TEXTURE DETERMINATION FROM ULTRASOUND FOR HCP AND CUBIC MATERIALS

by:

Bo Lan
Exeter College

Supervisors:

Prof. Fionn P.E. Dunne
Prof. Clive Siviour

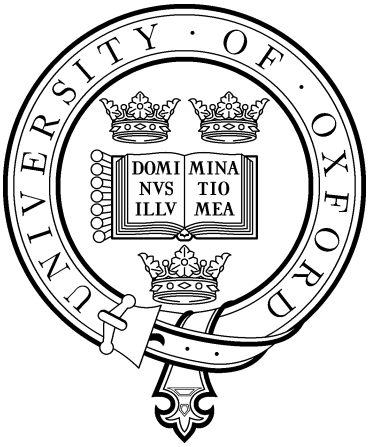

Department of Engineering Science
University of Oxford

A thesis submitted for the degree of
Doctor of Philosophy
Trinity 2014

Abstract

Crystallographic texture in polycrystalline HCP and cubic materials, often developed during thermomechanical deformations, has profound effects on properties at the macroscopic or component level. Given the respective natures of current detection techniques, a non-destructive, three-dimensional bulk texture detection method for these materials has not yet been developed. This thesis aims to achieve this goal through systematic studies on the relationship between ultrasonic wave velocity and texture.

The feasibility of such development is firstly reviewed via the combination of computational and experimental studies on exemplary HCP materials. Numerical results obtained via a representative volume element (RVE) methodology reveal that the wave speed varies progressively and significantly with changing texture, and experimental ultrasound studies combined with EBSD characterisation demonstrate distinguished velocity profiles for samples with different textures. Thus the possibility of the development is demonstrated from these combined results.

A novel convolution theorem is then presented, which couples the single crystal wave speed (the kernel function) with polycrystal orientation distribution function to give the resultant polycrystal wave speed function. Firstly developed on HCP and then successfully extended to general anisotropic materials, the theorem expresses the three functions as harmonic expansions thus enabling the calculation of any one of them when the other two are known. Hence, the forward problem of determination of polycrystal wave speed is solved for all crystal systems with verifications on varying textures showing near-perfect representation of the sensitivity of wave speed to texture as well as quantitative predictions of polycrystal wave speed. More importantly, the theorem also presents a solution to the long-standing inverse problem for HCP and cubic materials, with proof of principle established where groups of HCP and cubic textures are recovered solely from polycrystal wave velocities through the theorem and the results show good agreements with the original textures. Therefore the theorem opens up the possibility of developing a powerful technique for bulk texture measurement and wave propagation studies in HCP, cubic materials and beyond.

Acknowledgement

I would like to express my greatest gratitude to my supervisor, **Professor Fionn Dunne**, for the care and guidance he has been constantly offering throughout my DPhil study. Every bit of findings in this thesis is also saturated with his devotion. His passion and enthusiasm about research (and maybe his teasing skills as well) have deeply affected me and encouraged me to pursue a research career. Thanks also go to **Professor Mike Lowe**, **Dr Ben Britton** and **Dr Peter Huthwaite** for always enlightening me with insightful ideas, and **Professor Clive Siviour** for his help not only in academics but also in general affairs.

I would also thank my dearest girlfriend, **Yiming Dong**, for always accompanying me be it ups or downs of my study. Falling in love with her in the city of dreaming spires was the most beautiful thing ever struck on me. I am also heavily indebted to my family, especially my parents, **Fagui Lan** and **Yuzhen Luo**, and Yiming's parents, **Jing Wang** and **Jianhua Dong** for always being supportive of every step I moved forward.

I am blessed to have wonderful office atmospheres during my times both in Oxford and in Imperial, and I would like to thank my mates **Tomiwa Erinosho**, **Rodolfo Fleury**, **Jun Jiang**, **Jianan Hu**, **Kwanlae Kim**, **Ananya Renuka** and many more for creating such good environment. I would also thank **Anton Van Pamel**, **Gabor Gubicza** and **Dr Kalin Dragnevski** for help on experiments.

I am also grateful for having had a group of friends playing football together in almost every weekend and having gatherings occasionally. Even though I cannot include everyone's name here, I wish the likes of **Liang Xu**, **Ning Zhang**, **Shuai Yuan** and **Yin Dong** the best of luck in their future.

Finally, I would thank the Clarendon Scholarship Council, the Mandarin Scholarship Scheme of Exeter College and my direct sponsor, **Mr Alan Lamin** for the financial support in the past three years. Without them it would have not been possible for me to even start my DPhil. I am extremely grateful for having been offered the life-changing opportunity by them.

Contents

1 Introduction and Literature Review

HCP and cubic crystal structures make up a large portion of the commonly used materials, and crystallographic texture plays an important role in determining various properties of them. This thesis studies the interactions between such texture and ultrasound in HCP and cubic polycrystals (n.b. the other type of texture, the morphological texture, is not considered in this thesis), and this chapter serves as a brief description of the relevant research background. It starts by covering the fundamentals of crystallography, including the structures and symmetries of both crystal types, for better interpretations of texture and understandings of ultrasonic wave behaviours subsequently; it then gives overviews on the importance of texture and the reasons why it needs to be studied, and introduces the commonly used texture representation methods; this is followed by a comparison of advantages and disadvantages drawn among the most widely used techniques for texture detections, which demonstrates the origin of interests for a new detection technique using ultrasound to be developed; a review of the current literature is then given with focusses on the previous efforts of the development, which reveals the pieces of the puzzle that the work described in this thesis adds to the literature; the chapter finally concludes with a listing of the structure of the thesis.

SECTION. 1.1

Essentials of Crystallography

- **The crystalline state, unit cells & crystal systems**

Many commonly used artificial or natural substances are in crystalline state. Household products like salt, sugar and washing powders, precious stones such as rubies, sapphires, emeralds and diamonds or not-so-precious stones like quartz, are all examples of such crystalline materials [1]; most metals and ceramics for industrial usages, for instance steel, iron, copper, aluminium, titanium, are also crystalline. These materials may exist in the form of individual crystals, which are referred to as single crystals, or as aggregates of a number of crystals which are referred to as polycrystals; no matter in which form they are, the orientations of the crystals always play an important part in deciding the crystalline bulk properties, as will be covered in more detail later.

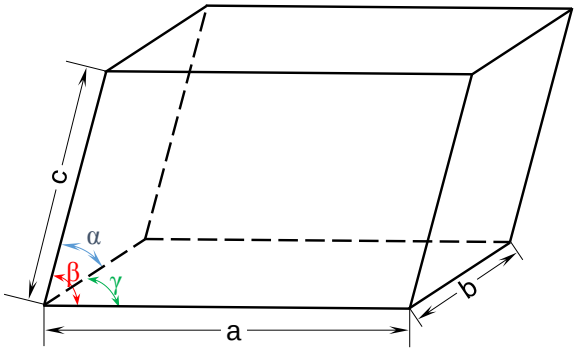

Figure 1.1: A general parallelepiped unit cell, fully defined by the lengths of its sides $a,\ b,\ c$ and angles $\alpha,\ \beta,\ \gamma$.

A crystal may be defined as a homogeneous body where the constituent atoms or molecules are arranged in a regular and periodic order [2, 3], and the smallest and irreducible subunit whose repetition in the three dimensions forms the crystal lattice is called a unit cell. It is from these unit cells where the symmetries of a crystal as

a whole derive [1, 2]; and according to the respective geometric features of their unit cells, crystals can be categorized into seven distinctive crystal systems.

The unit cells associated to the crystal systems are all parallelepipeds with their shapes completely defined by the combination of the relative lengths of the three sides a, b, c and the amplitudes of the angles α, β and γ, as shown in Figure 1.1, with the defining relationships listed in Table 1.1. The interests in this thesis lie upon the cubic system and a special case of the hexagonal system: Hexagonal Close-Packed, HCP.

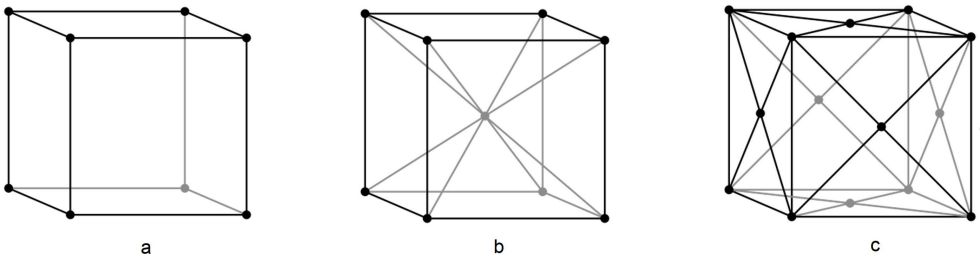

Figure 1.2: The three subsystems of the cubic crystal system: a. primitive (cubic-P); b. Body-Centred Cubic (BCC); c. Face-Centred Cubic (FCC). Image taken from [4], courtesy of Baszoetekouw.

The cubic crystal system can be divided further into three subsystems according to the atom or molecule (the motif of the repetitive unit cell) arrangements within a unit cell: primitive cubic (cubic-P), Body-Centred Cubic (BCC or cubic-I) and Face-Centred Cubic (FCC or cubic-F), as illustrated in Figure 1.2 a, b and c, respectively. Typical cubic-P materials include pyrite (FeS_2) and single element α phase Polonium [5] etc., while the examples of BCC materials include Fe, Cr, V etc. and those of FCC include Al, Cu, Ni etc; as for HCP materials, typical examples are Ti, Zr, Mg and many of their alloys.

Table 1.1: The relationships of sides and angles of the seven crystal systems [1, 3]

System Name	Relationships of Sides	Relationships of angles
Triclinic	NA	NA
Monoclinic	$a \neq b \neq c$	$\beta \neq \alpha = \gamma = \pi/2$
Orthorhombic	$a \neq b \neq c$	$\alpha = \beta = \gamma = \pi/2$
Tetragonal	$a = b \neq c$	$\alpha = \beta = \gamma = \pi/2$
Trigonal	$a = b = c$	$\alpha = \beta = \gamma \neq \pi/2$
Hexagonal	$a = b \neq c$	$\alpha = \beta = \pi/2,\ \gamma = 2\pi/3$
Cubic	$a = b = c$	$\alpha = \beta = \gamma = \pi/2$

- **Symmetries of HCP and cubic crystals**

The striking beauty of fine crystal samples originates from their symmetries, and from the examinations of many thousands of crystals it was demonstrated that all the crystal symmetry elements could be achieved through three simple types of operations: rotations, mirror planes and inversions [2]. In this section, the symmetries of the simplest and most regular HCP and cubic crystals (eg single element metals in terms of their crystal lattices and motifs) are examined as examples, and those of the similar and less symmetric crystal structures can be deducted by reducing some of the symmetry elements from these two examples.

Here I start with the rotation symmetries. If the exact appearance of a crystal remains after the crystal is rotated about an imaginary axis by the angle of $2\pi/n$ ($n \geq 1$), then the crystal is defined to possess an n-fold symmetry about the axis, and this is noted as a simple number n [6]. It can be mathematically proved [7] that the possible values of n which may occur in a crystal apart from the trivial 1 case are 2, 3, 4 and

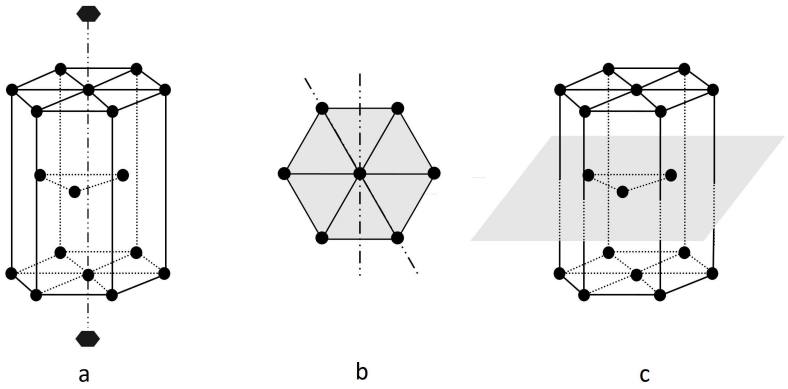

Figure 1.3: The symmetries of an HCP crystal: a. the sixfold symmetry (hexad) about its c-axis, b. the top view of the crystal with two mirror planes shown as the dashed lines; c. the mirror plane across the middle of the crystal.

6, and this is commonly known as the Crystallographic Restriction Theorem (however, this restriction does not apply for quasicrystals, see, for example, [8]). An HCP crystal possesses a sixfold symmetry (hexad) about its central axis which is called the c-axis of the crystal, as shown in Figure 1.3a, and the upper and lower planes perpendicular to the c-axis on which locate the hexagons formed by atoms are called the basal planes. In a cubic crystal, there are three types of rotation symmetries: six of twofold (diad), four of threefold (triad) and three of fourfold (tetrad), and they are illustrated in Figure 1.4a, b and c, respectively.

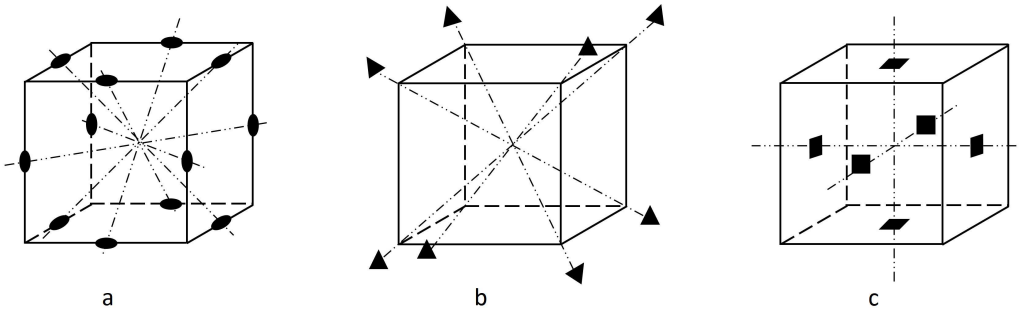

Figure 1.4: The rotation symmetries of a cubic crystal: a. the 6 of twofold symmetries (diads) about the $\langle 110 \rangle$ axes; b. the 4 of threefold symmetries (triads) about the $\langle 111 \rangle$ axes; c. the 3 of fourfold symmetries (tetrads) about the $\langle 001 \rangle$ axes.

When a crystal is divided into two parts by a plane in such a way that the part on one side of the plane is matched by the part on the other side in a reflection or

mirror-image manner, the crystal is defined to have a mirror plane symmetry about the dividing plane, and its notation symbol is the letter m [6]. There are three mirror planes in an HCP crystal, of which two go through the c-axis and are perpendicular to the atom planes, as shown in Figure 1.3b, and the other one is perpendicular to the c-axis and across the middle of the crystal, as shown by Figure 1.3c; a cubic crystal, on the other hand, has in total nine mirror planes, six of which are perpendicular to the six diad axes, as shown by Figure 1.5a∼c, and the other three are perpendicular to the three tetrad axes, as shown by Figure 1.5d.

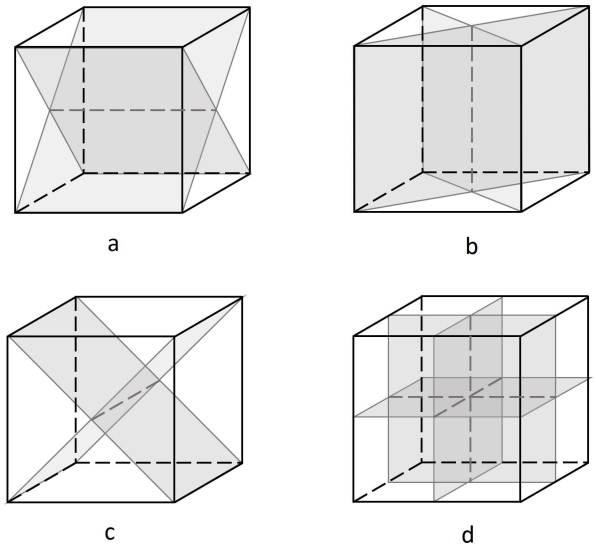

Figure 1.5: The mirror planes of a cubic crystal: a∼c show the 6 planes perpendicular to the 6 of diad axes, and d shows the 3 ones perpendicular to the 3 tetrad axes.

An inversion axis of order n is present in a crystal if all of its properties remain unchanged after going through the combination of a rotation about the axis for $2\pi/n$ and an inversion with respect to a point located on the axis [3], and this symmetry is noted as $\bar{n}$ [6]. There is no inversion axis in an HCP crystal, while all rotation symmetry axes in a cubic crystal are also inversion axes as they all go through the centre of the crystal, which is also the crystal's inversion centre.

So to conclude, an HCP crystal has one hexad about its c-axis perpendicular to one of its mirror planes and parallel with the other two; the perpendicular relationship

is often written in the point group convention as $6/m$, and along with the other two mirror planes they form the point group symbol for HCP as $6/mmm$. Similarly, the symmetries for the cubic crystal class can be written as $4/m\bar{3}2/m$ (even though the tetrads and diads axes are also inversion axes, these symmetries can be proved to be repetitive when both rotation symmetry and mirror planes are considered), which is usually mentioned as its equivalent and simpler form $m\bar{3}m$. These symmetries hold for the simplest HCP and cubic structures such as single element crystals, as well as many alloys made of Ti, Fe, Ni etc, in which the fundamental mechanisms for the alloys to form (substitutional or interstitial) do not normally cause significant lattice distortions or motif differences that change the symmetries, so these substances are still regarded to belong to point groups $6/mmm$ and $m\bar{3}m$ in this thesis.

SECTION. 1.2

The Importance of Texture and Its Representation Methods

- **The importance of texture**

One property of a material links an action applied on the material and the resultant reaction [9]. It is *isotropic* when it does not depend on the direction in which the action is exerted with respect to a fixed reference frame, and it is *anisotropic* when it does [9]. In practice, elastic, thermal, plastic, electric, magnetic properties of single crystals are always anisotropic, and it has been quoted that in many cases the magnitudes of differences in material properties can be as high as $20 \sim 50\%$ [10, 11]. Hence the crystallographic orientation (or simply *orientation*) of an anisotropic crystal, which is introduced as an operational definition to describe the crystal alignment after a series of rotations from an initial state [12, 13] that can be determined by diffraction experiments alone [9], has great importance in deciding the crystal's properties.

For a polycrystalline aggregate, even though the tensors representing these properties for all crystals are the same with respect to their respective crystal coordinate systems, they are certainly different if the crystal systems (i.e. orientations) do not overlap with the same global system, which would cause the aggregate to exhibit local variations of the properties; and in this case, it is the collective orientation distributions of all crystals that dictate the overall properties of the aggregate.

Due to the fact that the solidification and deformation histories of crystalline materials are always likely to cause the orientations not to distribute randomly but to display preferable patterns, the preferred orientation distribution, also referred to as crystallographic *texture*, is common place and an intrinsic feature of polycrystalline

materials such as metals, ceramics, polymers and rocks [14]. (It is emphasized that this thesis only addresses the issues of crystallographic texture, and the other type of texture, morphological texture, is beyond its scope; therefore the term *texture* refers to *crystallographic texture* in this thesis by default unless otherwise specified.) While the directional characteristics introduced by texture in polycrystalline materials were first recognized not in metals but in rocks, in the 20th century research on texture was overwhelmingly dominated by metallurgists and has recently grained popularity in ceramics and polymers as well.

Research on HCP textures has attracted significant interest only in recent decades because of the growing usages and importances of materials (mainly metals) of this crystal structure. For example, titanium alloys are employed extensively as structural materials in aerospace and aircraft industries; the zirconium alloy Zircaloy has been selected as the key material for cladding nuclear reactor fuels [15]; and magnesium alloys are widely used as structural materials in transport auto-mobiles and light-weighted enclosures for computer, communication and consumer (3C) electronics [16]. Elastically, HCP crystals are often simplified as transversely isotropic [17,18], meaning that they are isotropic on the basal plane about their c-axes (the hexad centre in Figure 1.3a); and as elastic stiffnesses along their c-axes are significantly higher compared to those on the basal plane [19], the the c-axes pole distributions for HCP materials are vital in elasticity evaluations. Plastically, there is no doubt that the crystallographic texture greatly influences the deformation behaviours for HCP materials, since the diversity in deformation mechanisms in an HCP crystal, eg basal slip, prismatic slip, pyramidal slip and a few twinning modes, are all coupled with texture in their effects on the macroscopic plastic behaviours of the polycrystals [20]. For example, texture dictates the initial state of the general anisotropy of yield strength (which is often expressed as a yield surface) of a polycrystal before plastic deformation happens, and the evolution of texture during plastic deformation would causes

an additional contribution to strain hardening [9] which would affect the change of the yield surface as well. The exemplary studies showing the importance of texture and its influence on plastic deformation include those for titanium [21–23], for zirconium [21, 24, 25] and for magnesium [26, 27].

In addition to texture, for titanium products, there is another important factor that has significant impact on their mechanical properties; that is, the occurrence of macro-zones, which are regions of near-uniform crystallographic orientation, the scale of which is normally about 100 times the size of a typical grain [28], observed in forged disks as well as in billets [29, 30]. Research shows that the presence of macro-zones, where the local basal poles are aligned close to the loading direction, are responsible for crack nucleation and growth, and can drastically reduce component fatigue life [28, 31].

Similarly with the HCP materials, the properties of cubic materials such as Fe, Cu, Al, etc. are also heavily affected by their textures. Elastically, the variations of stiffnesses over evaluation directions in single BCC-structured Fe are even more pronounced compared to HCP-structured Ti alloys [18, 32]. Plastically, there are 12 slip systems $\{110\}\langle\bar{1}11\rangle$ for BCC materials, and also 12 in number but different slip systems $\{111\}\langle1\bar{1}0\rangle$ for FCC materials [33]; because these slip systems are all defined with respect to local crystallographic orientations, it is obvious that texture dictates the slip modes of the polycrystals. As mentioned earlier, other properties apart from elasticity and plasticity such as thermal expansion and magnetic properties of cubic materials are also found to be heavily influenced by texture [9]. Therefore texture is one of the major causes of anisotropy for various properties in cubic polycrystals [34] and therefore attracts the interest of many researchers [10, 34–37].

• **Texture representation methods**

The most commonly used texture representation methods include pole figure, inverse pole figure and the Orientation Distribution Function (ODF), and one specifically for HCP texture representations: the Kearns' factors.

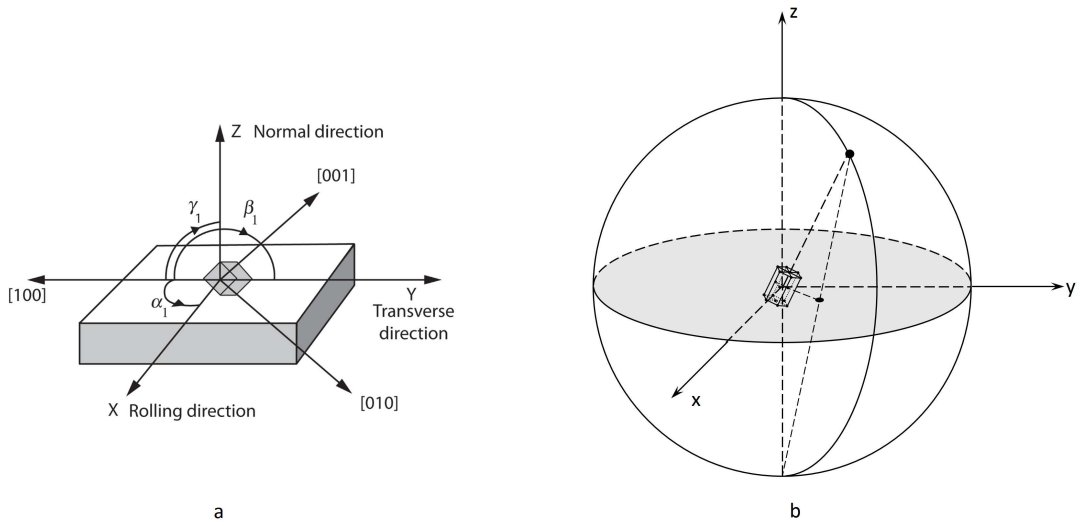

Figure 1.6: a. the definition of the sample and crystal systems, using a rolled sample with cubic crystals as an example [11]; b. the stereographic projection of the (0001) pole of an HCP crystal to the sample system.

In order to introduce the pole figure and inverse pole figure, the concepts of the sample and crystal systems as well as the stereographic projection need to be described first. The definition of the two coordinate systems is shown in Figure 1.6: the sample system is often defined according to the geometric features of the sample, eg for a rolled sheet, it is normally chosen as the right hand coordinate system containing the Normal Direction (ND), Rolling Direction (RD) and Transverse Direction (TD); and for an arbitrary crystal within the sample, there is also a crystal system naturally coherent with it. Now if the crystal is placed at the origin in the sample system, each lattice vector defined with respect to the crystal system always has an intersection point with the northern part of the unit sphere drawn from the sample system, as shown by Figure 1.6b, which corresponds to the crystallographic orientation; the line

linking this intersection point to the south pole also has an intersection point with the equatorial plane, which is the stereographic projection of the specific lattice vector (or pole) and clearly corresponds to the crystal orientation as well.

This is only the projection of a certain pole in a single crystal. If the same technique is carried out on the same pole across all crystals within an aggregate, the discretely-dotted pattern obtained on the equatorial plane which illustrates the distributions of the certain pole in the aggregate and hence reflects the crystallographic orientation distributions is called the pole figure [9,11,12]. A pole figure can be drawn as scattered points as well as a contour plot which shows the occurrence intensities of the pole at different projection positions, the latter of which enables mathematical descriptions of the orientation distributions and will be introduced with more details in Chapter 3.

The inverse pole figure technique is also based on the idea of stereographic projection, but unlike pole figure which uses the sample system as the reference system with respect to which all the crystal poles are projected, the inverse pole figure uses the crystal systems as the reference systems instead and projects the sample system onto different crystal systems, which is exactly the inverse process of obtaining a pole figure, hence the name *inverse* pole figure [11].

A pole figure or an inverse pole figure illustrates the distribution of one pole only, and it does not provide enough information to recover the original crystallographic orientation distributions of the polycrystals; to achieve the full description of the distributions, one needs at least two pole figures combined, or to employ the complete mathematical expression, the ODF.

The ODF is defined in terms of the three Euler angles introduced by Leonhard Euler to describe the orientation of a rigid body [38] so that any arbitrary orientation of a crystal can be achieved from a fixed sample system by means of three rotations about the axes following a certain sequence. For example, the sequence involving a

first rotation about the z-axis by an angle α and a second rotation by the angle β about the y$'$ axis obtained after the first rotation and a last rotation about z$''$ by γ (in short the z-y$'$-z$''$ sequence) is used by Roe [39] and Matthies [13] and will be employed throughout the thesis; the other commonly used Euler angle sequence is the z-x$'$-z$''$ one used by Bunge [12].

It is worth pointing out that the above rotations, no matter in Roe's or Bunge's conventions, are all done by rotating the coordinate system, which are often referred to in physics (especially in quantum mechanics) as *passive* rotations; in contrast, when evaluating a vector with respect to two different coordinate systems, an equivalent way to the passive rotation is to rotate a vector about fixed coordinate axes, which are referred to as *active* rotations. The resultant rotation matrices of both rotation types have the following relationship [40]:

$$\begin{aligned} R^{(p)}(\alpha,\beta,\gamma) &= R^{(p)}_{z''}(\gamma)R^{(p)}_{y'}(\beta)R^{(p)}_{z}(\alpha) = [R^{(a)}(\alpha,\beta,\gamma)]^{-1} \\ &= R^{(a)}_{z}(-\alpha)R^{(a)}_{y}(-\beta)R^{(a)}_{z}(-\gamma), \end{aligned} \tag{1.1}$$

and this relationship will be fully utilized in our subsequent mathematical deductions.

With single crystal orientation described, the ODF of a polycrystal is thus defined as the statistical occurrence distribution function of the three Euler angles, whose varying ranges for α, β and γ are $(0, 2\pi)$, $(0, \pi)$ and $(0, 2\pi)$ respectively, by which means the complete texture information of the polycrystal is encapsulated in the ODF. The graphical representation of the ODF is called the ODF diagram, while the mathematical expression is often expanded in terms of its harmonic functions [12, 39, 41], from which the pole figure contour plots can also be derived.

For HCP materials (especially for zirconium alloys), Kearns [42] found it more convenient in industries to use an even smaller fraction of the ODF information compared to the (0001) pole figures, hence he defined the indices f containing the statistical

proportions of c-axes aligned along the respective surface directions of the sample as shown by equation 1.2 [42, 43], which are then called the Kearns' factors:

$$\begin{aligned} f_{\mathrm{RD}} &= \frac{1}{N}\int_0^{2\pi}\int_0^{\pi/2} I(\theta,\phi)\sin^3(\theta)\cos^2\phi \; d\phi d\theta \\ f_{\mathrm{TD}} &= \frac{1}{N}\int_0^{2\pi}\int_0^{\pi/2} I(\theta,\phi)\sin^3(\theta)\sin^2\phi \; d\phi d\theta \\ f_{\mathrm{ND}} &= \frac{1}{N}\int_0^{2\pi}\int_0^{\pi/2} I(\theta,\phi)\sin(\theta)\cos^2\theta \; d\phi d\theta \end{aligned} \tag{1.2}$$

where $I(\theta,\phi)$ is the (0001) pole distribution intensity function at the position with polar angle θ and azimuthal angle ϕ, and the constant N is the total intensity integrated over part of the surface of the unit sphere

$$N = \int_0^{2\pi}\int_0^{\pi/2} I(\theta,\phi)\sin\theta \; d\phi d\theta. \tag{1.3}$$

SECTION. 1.3

Common Texture Measurement Techniques

Given the importance of texture, many techniques have been developed to extract the information. In this section, a few widely employed texture measurement techniques are briefly reviewed, among which some are capable of performing measurements across relatively large regions (several millimetres to several centimetres) hence are classifies as macrotexture techniques, such as X-ray diffraction and neutron diffraction, while others like Electron Back Scatter Diffraction (EBSD) are designed for measurements within small regions (typically a few hundred microns) and to show more details about grain morphologies and individual grain orientations etc. hence are classified as microtexture techniques [11].

- **X-ray diffraction**

X-ray diffraction was among the first techniques used to evaluate preferred orientations in metals, and its fundamental theoretical basis is sketched in Figure 1.7 with a single crystal and a monochromatic beam as an example: the X-ray beams are reflected by crystal lattice planes like lights reflected by mirrors, and only when a given X-ray wavelength λ and lattice plane spacing d satisfy the well-known Bragg's Law [44], $n\lambda = 2d\sin\theta$ (where n is an integer), can the reflected beam from the lattice plane be received at the calculated receiver's position. Therefore if reflections can be received by the receiver for a crystal which happens to be oriented with a specific lattice plane parallel with the sample surface in the configuration shown by Figure 1.7a, then for another crystal with a rotated orientation where the particular lattice plane is not parallel with the sample surface any more, no reflections can be obtained, as shown by Figure 1.7b; the only way to receive the reflected beam with this configuration is to carefully tilt the sample to a position with the lattice plane

parallel with the sample surface, then the signals from reflections would appear on the receiver again, as shown by Figure 1.7c, and the current sample tilting position is clearly directly related with the relative orientation of the concerned crystal with respect to the sample.

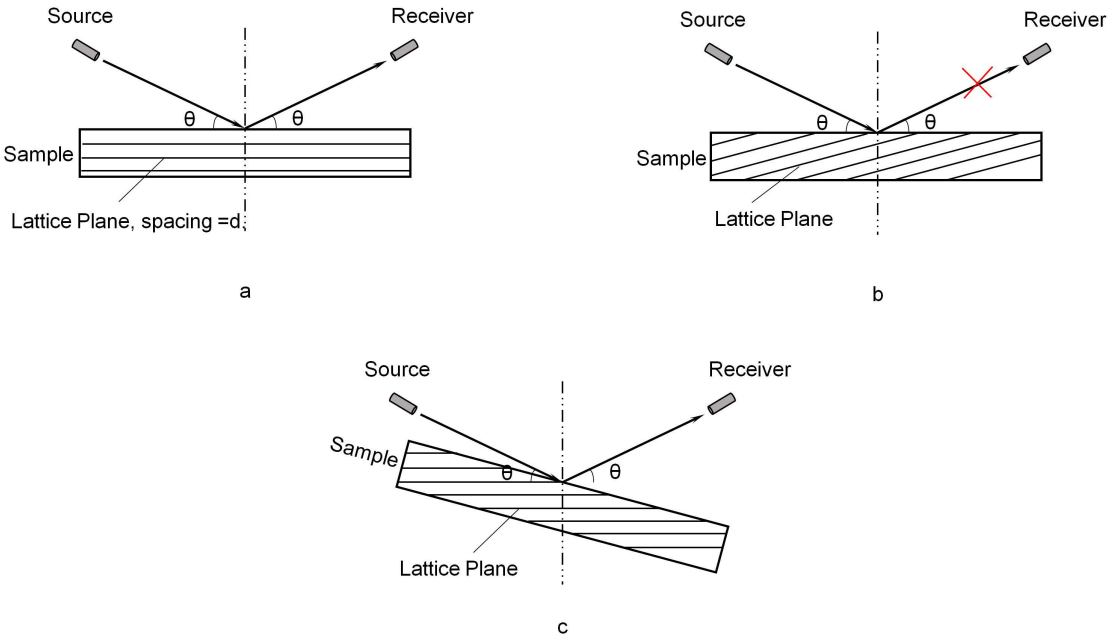

Figure 1.7: Sketch of how the Bragg's Law applies to X-ray diffraction on lattice planes, where a: the lattice plane (hkl) is parallel to the sample surface, and the X-ray beam source and receiver are both configured with an angle θ to (hkl) satisfying the Bragg's Law, the receiver is able to detect an energy peak of the beam reflected by plane; b. the (hkl) plane is at an angle with the sample, and the receiver cannot detect any signal at this position; c. the sample is tilted to an angle to make the lattice plane (hkl) in the same position as (hkl) in a, where the receiver receives a peak again. Based on the tilting the relative orientation of the lattice plane with respect to the sample surface can be deducted [11].

Therefore for polycrystalline samples, the intensities recorded at a fixed receiver position θ is for the detections of a certain lattice plane hkl only, and they need to be combined with the tilting angles of the sample for the interpretation of the orientation distributions of the hkl plane normal. This is how a pole figure may be obtained from X-ray diffraction experiments [11, 14]. Two different geometrical setups of texture goniometers are applicable in X-ray tests: transmission and reflection, as shown

by Figure 1.8, and in most conventional tests the latter goniometer is employed as the intensity and penetration depth of the X-ray beams are limited, with the former goniometer restricted to usages on low absorption materials like magnesium and aluminium or extremely thin films [11]. The above descriptions are about the detections using monochromatic X-ray beams, but a similar theoretical basis, Bragg's Law, still applies for other test modes such as those with white light sources of multiple X-ray wavelengths and a range of varying reflection receiving positions.

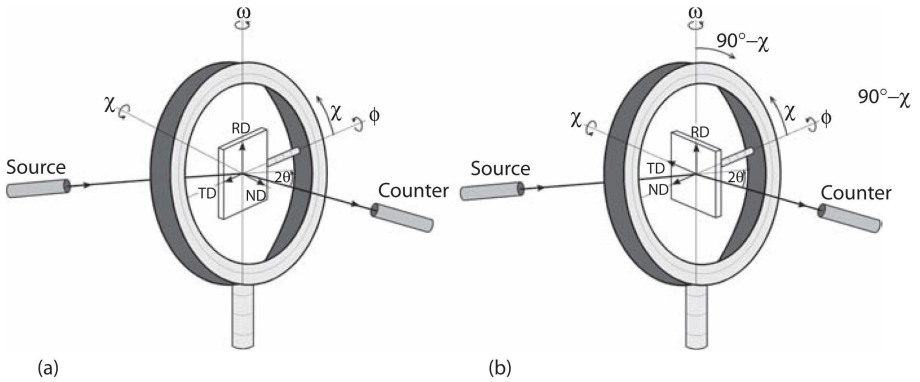

Figure 1.8: Diffraction in four-cirle goniometers with two geometrical setups: (a). transmission and (b). reflection. [11].

Each pole figure from the X-ray diffraction test contains the orientation distribution of a certain lattice plane normal (or a reciprocal lattice vector) according to Bragg's Law, and the solution to the inverse problem of obtaining the complete ODF from a series of tests was worked out independently by Roe [39] and Bunge [12], which marked a milestone for texture detection and ensured the prominence of X-ray diffraction for decades [1, 44].

- **X-ray synchrotron**

Compared to the X-ray beam generated by conventional sources which are of relatively low intensity, the beam used by X-ray synchrotron is produced in storage rings or other sophisticated particle accelerators and hence is fine-focused and of high-intensity

with monochromatic or continuous wavelengths. The unique advantages of its high intensity, small beam size and free choice of wavelength open a wide range of new possibilities [45, 46], and the particular features include good resolution in the Bragg angle, extremely high angular resolution in crystal orientation (pole figure angles) and high penetration depth of several millimetres to centimetres [46]. Because of the high penetration depth, synchrotron tests are often performed in transmission mode, as shown by Figure 1.8b.

Synchrotron diffraction images captured by CCD detectors almost instantaneously display the presence of texture expressed in systematic intensity variations, and the data can also be recorded to allow elaborate post-processing to determine texture patterns quantitatively [14]. The technique is particularly valuable for compounds with weak scattering(eg polymers and biological materials) and for investigating local texture variations, and other applications, eg *in situ* observations of texture changes during deformation at high pressure and high temperatures, also benefit from the unique advantages of the synchrotron technique.

- **Neutron Diffraction**

Neutron diffraction has a history for texture analysis almost as long as X-ray diffraction. The technique requires a source of neutrons, so it is normally carried out either at reactors with a constant flux of thermal neutrons or with pulsed neutrons at spallation sources [14, 47]. The wavelength distribution of thermal neutrons is a broad spectrum similar to X-rays. Different from X-ray beams which are scattered by electrons surrounding the nucleus of an atom hence can penetrate a very limited depth, neutron beams do not bear charge hence have no interactions with the electrons but are scattered only by the nucleus in the centre of an atom with a size typically 100,000 times smaller than the distance between neighbouring centres [48], therefore the scattering and reflections of neutron beams within matters are much lower than

X-ray, empowering the neutron diffraction technique with advantages of high penetration and low absorption and making it suitable for bulk texture investigations of large sample volumes. Because of the low absorption rate of neutrons, environmental stages (heating, cooling, straining) can be applied as variables in the technique for *in situ* observation of texture changes; and because of the high penetration depth, these tests are normally performed in transmission mode as shown by Figure 1.8b.

- **Electron Back Scatter Diffraction**

All the techniques mentioned above are for macrotexture measurements only able to provide statistical orientation distributions without giving any spatial resolution regarding the structures of the crystals, and this is overcome by the Electron Back Scatter Diffraction (EBSD) technique, which is able to link the microtexture directly to crystallographic macrotexture representations [49].

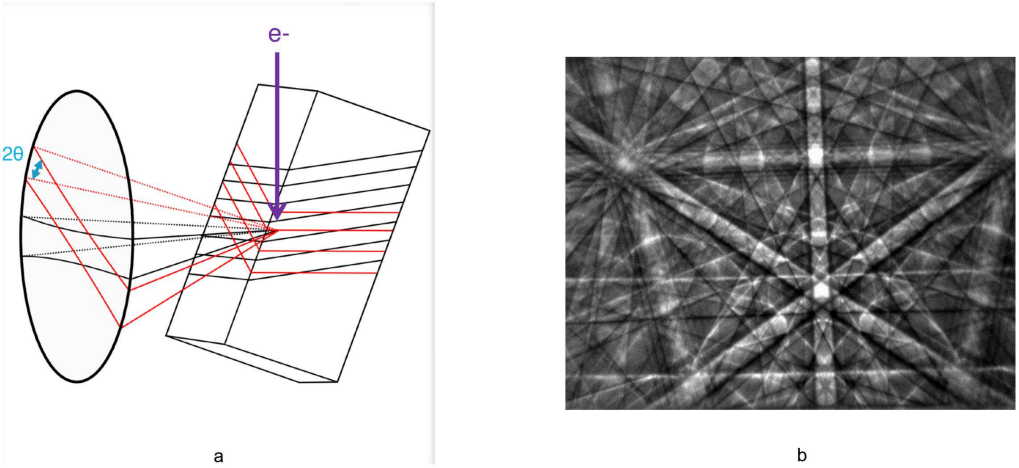

Figure 1.9: a. The reflection of the electron beam by a certain lattice plane within the tilted sample; b. a typical Kikuchi pattern formed in an EBSD test, the lines crossing each other are formed by the reflection of the electron beam from different lattice planes [50].

The basic principles are illustrated in Figure 1.9 [50]. When a highly-focused electron beam strike upon the surface of a tilted sample, some of the electrons are elastically

backscattered by the crystal lattice planes in the similar way with the X-ray reflection, from which the reflection lattice planes can be inversely inferred based on the Bragg's Law. The reflections of the electron beams from the same set of lattice planes, if projected on a CCD detector as shown by the circle in Figure 1.9, forms a set of parallel lines on the detector; the reflections from different lattice planes at the same test position are in different angles, hence the projections on the detector appear to be a pattern with lines crossing each other. This pattern so formed is called the Kikuchi pattern, which contains the information of various lattice orientation at the test point, and by interpreting the Kikuchi pattern at a test point, the orientation of the crystal at this point can be inferred; by interpreting test points from a raster scan on the surface, EBSD is able to acquire accurate orientations at all these testing positions on the surface to generate a grain orientation map [49, 51]. This unique advantage has gained the EBSD technique great momentum since the 90s and made it the most widely used texture detection method [51].

- **Spatially Resolved Acoustic Spectroscopy**

Even though full microtexture information can be obtained through EBSD, the scanning processes are quite slow, which restricts EBSD tests to normally very localized regions; besides, the samples need to undergo extremely delicate preparation processes before the tests can be made. Spatially Resolved Acoustic Spectroscopy (SRAS) is an excellent alternative technique which overcomes many of these disadvantages of EBSD at the cost of some loss of resolution. This technique is based on the fact that the anisotropy of the crystals causes the velocities of the surface acoustic waves (SAWs) to vary with the evaluation direction, and via mapping the SAW velocities in various different directions, the orientation of the crystals at the sample surface can be inversely determined. By doing so the SRAS is able to detect the crystallographic orientations across a large region in almost real time [52, 53].

- **Respective shortcomings of these techniques**

X-ray and EBSD techniques both require relatively good surface finish, so they are destructive during sample preparation; moreover, they and the SRAS technique are all surface or near-surface techniques, meaning that the textures detected are limited within the surface or sub-surface layers of the sample. Even though the neutron diffraction and X-ray synchrotron techniques can penetrate a thickness up to centimetres [54, 55], the former requires a neutron source and the energy the latter needs is extremely high, hence these tests can only be conducted in certain sites with limited access and are also very expensive.

SECTION. 1.4

Attempts to Recover Bulk Texture Information from Ultrasonics

Due to the respective shortcomings of the techniques reviewed in the previous section, it is therefore desirable for a non-destructive technique capable of bulk texture measurement to be developed; and given their attractive natural properties [56], bulk ultrasonic waves are the best candidate for this task. The efforts devoted to solve this *inverse* problem (i.e. to extract texture from ultrasonic speed measurements, as opposed to the *forward* problem where texture is known and ultrasound wave speed is predicted) can be categorized into making use of two ultrasonic wave properties: attenuation and wave velocity variation.

- **Recovering texture using attenuation methods**

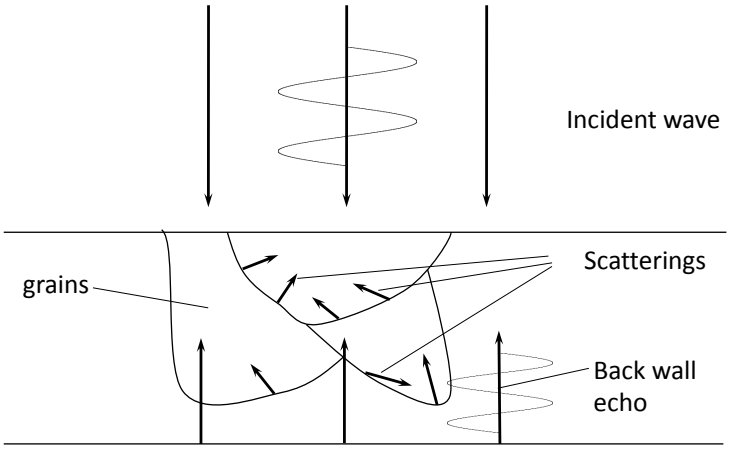

Figure 1.10: Attenuation is defined as the loss of energy between the incident wave and the echo (directly reflected by their amplitudes), and its two major contributing factors are absorption (i.e. energy dissipation, not shown in the figure) and scattering.

Attenuation of ultrasonic waves is defined as the loss of energy between the incident wave and the echo or the transmitted wave, and its two major contributing factors are absorption (i.e. energy dissipation) and scattering, as shown in Figure 1.10. Normally

only the latter factor is utilized in theoretical and experimental analyses because of the difficulty of measuring absorption and the fact that scattering is expected to dominate in typical cases of attenuation measurements. Early attempts to relate wave scattering with grain anisotropy were made by Stanke and Kino [57], who developed a theoretical model to predict the attenuation due to scattering within a single-phased polycrystal with anisotropic grains. Latter experimental evidence proved that for a mill annealed Ti-6Al-4V bar, the orientation dependence of attenuation stemmed from the scattering effects associated with texture and macroscopic elongated grains [58], which was similar with results reported for austenitic stainless steels that developed columnar grain structure due to solidification [59]. But because of the randomness of scattering and the resulting attenuation, measurement of attenuation is not capable of capturing information for texture extraction, and thus is mainly used for other purposes, for example grain size detection, and some exemplary efforts in this regard include [60–63].

Evidences have been reported that when there are presences of macrozones (sometimes termed differently by the NDE community as micro-textured regions, MTRs, or duplex microtextures) in titanium alloys which drastically affect the fatigue lives of the components [28,31], the scattering behaviours of the materials also become significantly different, which provides the opportunity for the macrozones to be directly examined by ultrasonic waves and has triggered much related research. For example, Han and Thompson [64] proposed a theory to predict backscattering coefficients in the regions consisting of macrograins and applied it to titanium alloys; Bhattacharjee et al [65] found that when correlating the ultrasonic attenuation with the microtexture within a near-α sample, the results indicated nearly linear dependence of the attenuation on the microtextured region size in the $d/k = 0.1$ to 1.0 range, where d and k are the effective microtexture region size in the direction of wave propagation and the ultrasonic wavelength, respectively; Yang et al [66,67] introduced a model to

study scattering-induced attenuation and used it to study the marcozones and found good agreement between the prediction of the model and experimental results.

- **Retrieving texture from wave velocities**

Compared to attenuation, bulk wave velocity is coupled more closely with polycrystal orientation and offers a more rigorous mathematical relationship to be developed between the two. The commonly followed route in doing so is, first, establish the mathematical expression for the polycrystal elastic properties using the single crystal properties and texture information; second, bridge the texture information with ultrasonic wave velocity through the direct relationship between elastic properties and wave velocities (eg the Christoffel equation); and finally, employ the range of known wave velocities with the established relationship and invert the resulting equations to give the texture information. However, this inverse process is not a trivial problem for polycrystals and a robust solution has remained elusive.

In determining the polycrystal elastic properties, grain average methods are often employed, where three assumptions apply. The first by Voigt assumes that strain is constant across the polycrystal hence averaging the stiffness matrix by volume fraction gives the overall stiffness matrix of the polycrystal; Reuss, however, assumed stress to be constant and averaged the compliance to give the resulting polycrystal compliance matrix; Hill concluded that the methods by Voigt and Reuss in fact set up the upper and lower bounds respectively for the possible elastic properties, which are likely to lie at the average values of the Voigt and Reuss results [68]. Relating texture with polycrystal elastic properties can be done by following Roe's idea of spherical expansion [39]. Morris [69] employed Voigt's assumption and expanded both the ODF and the 8th order rotation tensor into spherical harmonics and used the orthogonality of the expansion to eliminate the expansion bases and thereby obtained the polycrystal elastic moduli expressed with single crystal moduli and the

ODF coefficients for samples with orthorhombic symmetries. Sayers [70] pushed this idea forward by developing explicit expressions between ODF coefficients and wave velocities in different directions and then applying it to austenitic stainless steel to inversely obtain the coefficients. Backus [71] chose to decompose the elastic tensor instead of the rotation tensor into harmonics, of which the relations were later used by Smith et al [72] to study the azimuthal dependence of Love and Rayleigh waves. A helpful summary of the mathematical basis of these theories related to hexagonal materials is given by Li et al [73].

These approaches laid down the theoretical foundations for the majority of the subsequent studies, especially for texture detection on plate-shaped samples where the texture relations with other wave modes like Rayleigh and Lamb waves can also be utilized [74–76]. For example, Sayers [77] derived the expressions for angular variation of ultrasonic waves in hexagonal materials for non-destructive tests; Hairo [75]combined the texture relations with both Rayleigh surface waves and skimming Lamb wave modes to get the non-zero ODF coefficients and obtained coarse pole figures; Kielczynski et al [76] made use of bulk longitudinal wave, Rayleigh surface wave and Lamb wave modes to obtain five texture coefficients for hexagonal samples with orthorhombic symmetry; Thompson et al. [74] and Dixon et al. [78] used only the Lamb wave dependence of texture coefficients to obtain three 4th-order ODF coefficients for cubic materials. Anderson et al. [43] performed similar studies to extract Kearns factors from hexagonal-grained Zircaloys.

The major disadvantages of these studies are, first, most of them are based on the assumption of orthorhombic sample symmetry in order to minimize the numbers of unknown ODF coefficients, and force others to be zero, which inevitably leads to loss of information in most cases. Second, the use of Rayleigh or Lamb waves which only exist in surface layers or thin plates narrows the applicability of the general method for bulk texture determination; and finally, the ODF coefficients are complex numbers

by definition so that when real spherical harmonic expansion is used, information loss occurs because in all these studies, only one real number is recovered for each of the coefficients.

SECTION. 1.5

Structure of The Thesis

This thesis aims to tackle the long-standing inverse problem of texture detection from ultrasound and provide a solution to it (at least for two of the crystal systems), which would enable the evaluation and determination of bulk texture information in polycrystalline HCP and cubic aggregates directly from ultrasonic wave speed measurements. In order to progressively identify the challenges and explain clearly how they are overcome, the thesis is organized in the following structure:

In Chapter 2, the feasibility of the whole study is reviewed by examining the magnitudes of differences of ultrasonic wave velocity varying with crystallographic textures in HCP materials. In doing so, relevant theories are introduced first, based on which a dynamic polycrystal finite element model is then established, with properties of exemplary HCP materials Zr and Ti-6Al-4V incorporated and a range of textures implemented, for the simulation of plane wave propagating in polycrystalline aggregates, and the computational results are finally combined, compared and verified by experimental EBSD and ultrasonic studies on a couple of samples.

Chapter 3 provides a solution to the inverse problem for HCP materials. An analytical model is firstly established by introducing vector forms to the conventional grain average idea, with further analysis on the model using the spherical harmonic method leading to a novel spherical convolution relationship, which enables both forward and inverse studies for the materials to be carried out in a very simple fashion, thus the detection of texture directly from ultrasonic wave velocities is also made possible. A proof of principle is then established via qualitative and quantitative comparisons with results from the computational model set up in Chapter 2.

In Chapter 4, the analytical model and convolution relationship introduced in Chapter 3 are extended to a generalised form by taking all three Euler angles into account

when calculating orientation distributions. Similar spherical harmonic analyses are performed and a generalised convolution theorem is obtained, which now enables forward studies (ultrasonic wave speed predictions from texture information) for all crystal types, as well as the inverse determination of texture from ultrasound for cubic materials when their crystal symmetries are considered. Proof of principle is also established by using metal Fe as the exemplary cubic material.

Finally, Chapter 5 concludes the major contents of the thesis and lists the future plans to be carried out that are beyond the scopes already covered in this thesis, including experimental validations of the theoretical models and a possible device development.

2

Feasibility Studies: How Strongly Ultrasonic Wave Velocities Are Coupled with Textures?

This chapter contains three major sections. In the first section, the anisotropic ultrasound behaviour in HCP materials is briefly reviewed, followed by the development of a dynamic elastically anisotropic finite element model containing representative volume elements (RVEs) for both single- and two-phase HCP polycrystals. The ultrasonic wave loading is described together with the model boundary conditions and wave velocity extraction techniques. The model is then evaluated and verified via primary studies on single crystals and bi-crystals with varying boundary conditions.

This is followed by the second section on computational forward studies using the polycrystal model. Single-phase Zr polycrystals with a range of textures are implemented into the RVE model and their responses to ultrasonic excitation representative of laboratory testing techniques are examined in order to demonstrate the strong variations in ultrasonic wave speed resulting from texture change, and the incorporation of a macro-zone.

In the next section, laboratory-based ultrasonic scans and EBSD investigations are performed on two differing (unidirectionally and cross-rolled) two-phase Ti samples, in which the ultrasonic responses and EBSD characterisations in three orthogonal directions are investigated. The EBSD characterisations, detailing both the HCP alpha

and BCC beta phase crystallographic orientations and their distributions are then employed to construct representative model polycrystals with which computational ultrasound studies are then carried out in the three orthogonal directions. Detailed comparisons between the results of the experimental ultrasonic testing and the model predictions are presented. The chapter is then concluded by considering the potential for the use of ultrasonic measurement techniques for the detection and quantification of HCP textures and macro-zones, and address the difficulties associated with the introduction of more realistic two-phase microstructures.

SECTION. 2.1

Background: theoretical and computational models

In this section, firstly a brief review on the angular variation of the ultrasonic wave velocity in a single HCP is given because of its centrality to subsequent interpretation of results. It is based upon the well-known Christoffel equation for which a summary of the deductions is presented; then I move on to establish a Finite Element (FE) model of a Representative Volume Element (RVE) for the dynamic elastic analyses of wave propagation in polycrystals which will be employed through out this thesis; the section is then concluded via verifications of the computational model through some primary applications on single crystals, bi-crystals and grain boundaries.

2.1.1 The theoretical model: Christoffel equation

The Christoffel equation was first introduced by the German physicist E.B. Christoffel [79], and it has since been applied for theoretical analyses on ultrasonic wave velocities in single crystals or polycrystals of all types of crystal structures. Here the deduction process of the equation is briefly listed, and for more detailed descriptions the reader is referred to [80] and [81].

Consider an elastic longitudinal wave propagating in an infinite homogeneous and purely anisotropic medium. The three-dimensional wave equation can be written as:

$$\frac{\partial \sigma_{ij}}{\partial x_j} = \rho \frac{\partial^2 u_i}{\partial t^2}, \tag{2.1}$$

where i and j both range from 1 to 3, x_j describes the position along the jth coordinate axis, t is time, σ_{ij} refers to the components of the stress tensor $\boldsymbol{\sigma}$, and $\boldsymbol{u}$ is the local displacement function of both position and time.

The stress tensor $\boldsymbol{\sigma}$ is then linked to the strain tensor $\boldsymbol{\epsilon}$ in an anisotropic medium by

the Hooke's Law written as

$$\sigma_{ij} = C_{ijkl}\epsilon_{kl}, \tag{2.2}$$

where $\mathbf{C}$ is the elastic stiffness tensor of general anisotropy, and the strain tensor components ϵ_{kl} are defined as

$$\epsilon_{kl} = \frac{1}{2}\left(\frac{\partial u_l}{\partial x_k} + \frac{\partial u_k}{\partial x_l}\right). \tag{2.3}$$

Combining equations 2.1, 2.2 and 2.3 yields the three-dimensional wave equation

$$\rho\frac{\partial^2 u_i}{\partial t^2} = \frac{1}{2}C_{ijkl}\left(\frac{\partial u_l}{\partial x_k} + \frac{\partial u_k}{\partial x_l}\right). \tag{2.4}$$

Due to the symmetry of the strain tensor, k and l in equation 2.4 are interchangeable, which simplifies the equation into:

$$\rho\frac{\partial^2 u_i}{\partial t^2} = C_{ijkl}\frac{\partial u_l}{\partial x_j \partial x_k}. \tag{2.5}$$

Meanwhile, if we are interested in the wave velocity in an arbitrary direction $\boldsymbol{n}$, a harmonic solution to the wave equation in $\boldsymbol{n}$ may be expressed as

$$u_i = A_i \exp[i(\xi n_j x_j - \omega t)] \tag{2.6}$$

where $\boldsymbol{A}$ is the particle displacement vector, ξ is the wave number, and n_j is the jth component of the unit vector $\mathbf{n}$ in the desired propagation direction. Substituting equation 2.6 back to 2.5 and introduce a new variable $\Lambda_{ijkl} = C_{ijkl}/\rho$ lead to:

$$\omega^2 A_i = \frac{C_{ijkl}}{\rho}\xi^2 n_j n_k A_l = \Lambda_{ijkl}\xi^2 n_j n_k A_l, \tag{2.7}$$

and introducing the phase velocity $v = \omega/\xi$ further give the relationship

$$\left(\Lambda_{ijkl} n_j n_k - v^2 \delta_{il}\right)(A_l) = 0. \tag{2.8}$$

Equation 2.8 is a classical eigenvalue problem, whereby projecting the velocity onto the ith direction gives the ith eigenvalue. To ensure the equation has non-trivial solutions, its determinant must be zero, i.e.

$$\left|\Lambda_{ijkl} n_j n_k - v^2 \delta_{il}\right| = 0, \tag{2.9}$$

and three velocities can be obtained as the eigenvalues by solving this equation. The largest solution has an eigenvector (particle displacement vector) along or close to the desired direction $\boldsymbol{n}$, and hence is a longitudinal or quasi-longitudinal wave velocity, and the other two are both shear waves. Given the nature of eigenvectors, the particle displacement directions of the three velocities are mutually orthogonal to each other. Here HCP crystals are used as a demonstration of the usage of the equation. Their crystal structure, eg in zirconium, is often simplified to be transversely isotropic such that isotropy in elastic response is assumed within a basal plane about the crystal c-axis (normal to the basal), but the c-axis direction modulus is different to the a-type directions. Hence the elastic stiffness matrix (where all components are given in GPa) for a single phase alpha zirconium crystal at room temperature may be written as

$$\mathbf{C} = \begin{pmatrix} 136.0 & 78.0 & 68.0 & & & & \\ 78.0 & 136.0 & 68.0 & & & & \\ 68.0 & 68.0 & 163.0 & & & & \\ & & & 29.0 & & & \\ & & & & 40.0 & & \\ & & & & & 40.0 & \end{pmatrix} \tag{2.10}$$

in which the c-axis is here aligned along the z-axis of the coordinate system. Since the HCP crystal is isotropic about the c-axis, the wave velocities on the y-z plane are representative of any other plane that contains the z-axis. Considering, therefore, the y-z plane as the representative plane, and taking a loading direction which lies on the plane and makes an angle θ from the z-axis (but in the y-z plane), the unit vector $\mathbf{n}$ of this direction is then:

$$\mathbf{n} = \begin{pmatrix} n_1 & n_2 & n_3 \end{pmatrix}^{\mathrm{T}} = \begin{pmatrix} 0 & \sin\theta & \cos\theta \end{pmatrix}^{\mathrm{T}} \tag{2.11}$$

Substituting equations 2.10 and 2.11 into equation 2.9 enables the longitudinal wave velocity with respect to angle θ to be determined and this is shown in Figure 2.1 for the HCP crystal considered.

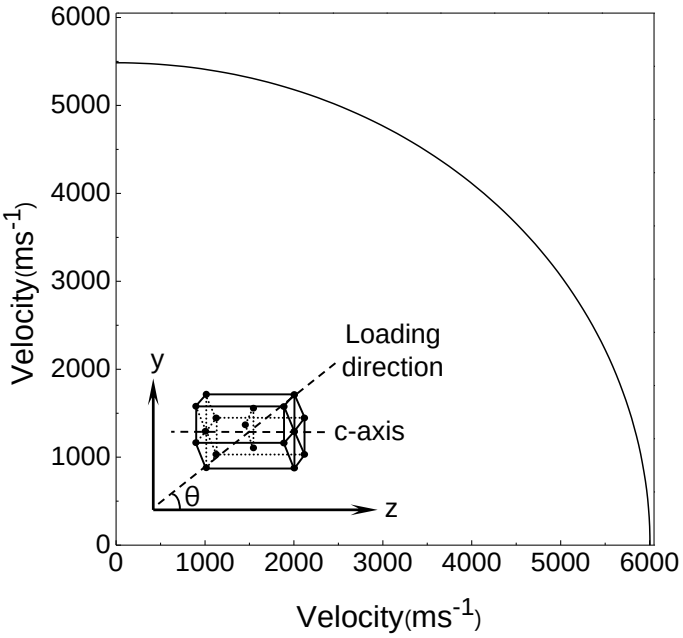

Figure 2.1: Longitudinal wave velocity changing with crystallographic orientation θ.

The figure shows that the lowest velocity of 5485 m/s occurs when $\theta = \pi/2$, corresponding to the configuration for which the wave propagates perpendicular to the c-axis of the crystal; then the velocity increases with increasing angle, until the high-

est magnitude of 6005 m/s occurs when $\theta = 0$, which corresponds to the configuration for which the wave propagates parallel to the c-axis. The latter configuration is henceforth referred to as the *reference configuration*, and all other crystal orientations are given with respect to it. The two cases of wave propagation at $\theta = 0$ and $\theta = \pi/2$ are used as benchmarks for the subsequent computational analyses.

2.1.2 Dynamic Elastic Polycrystal FE Model

The computational polycrystal methodology has been widely used to tackle plasticity problems [82,83], but here it is employed to simulate ultrasonic wave propagation in a polycrystalline single-phase HCP aggregate. In this approach, explicit representation of the material grains and their crystallographic orientations are made, and full account is taken of the elastic anisotropy discussed above, within a fully dynamic finite element formulation enabling the anisotropic wave equation, shown by equation 2.5, to be solved point-wise spatially and temporally within the finite element method. Here the polycrystal RVE, boundary conditions, ultrasonic loading conditions and ultrasound wave velocity results extraction are presented.

- **Polycrystal representative volume element**

A representative volume element (RVE) finite element model has been developed for the simulations consisting of 2160 crystals or grains in Abaqus/Explicit, shown in Figure 2.2a. The macro-level uniaxial material response is sought first so that a representative square-section model of dimensions $900 \times 900 \times 9000$ μm^3 with $6 \times 6 \times 60 = 2160$ crystals is used, in which each crystal is in cubic shape with dimension 150 μm. The grain size chosen is representative of near α-phase titanium or single-phase Zr alloys. The crystallographic orientation of each crystal is independently specified in order to establish a range of crystallographic textures and single crystal orientations within the RVE.

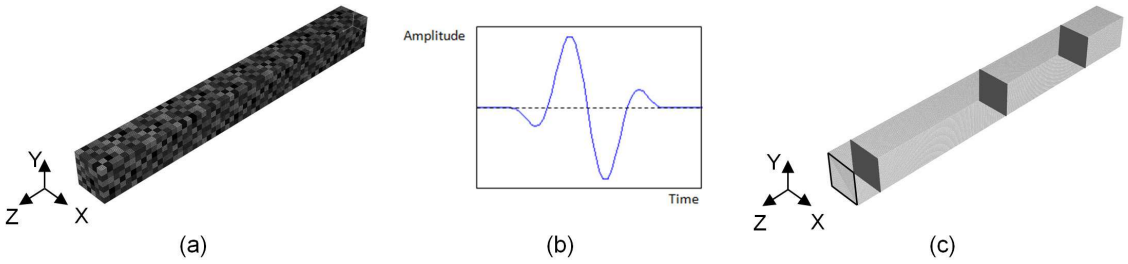

Figure 2.2: a. Representative volume element containing 2160 crystals with a total ∼7.3 million finite elements; b. a schematic of the Hanning Window and ultrasonic wave pulses imposed; c. the locations of the measurement planes in the RVE used for data extraction. Meanwhile, the lateral faces of the bar are all fixed in their normal directions and the far end of the bar is set as a free surface.

The time step size in the finite element model is decided with the following considerations. Firstly, the wave velocities in zirconium are in the order of 5000 m/s, leading to extremely short wave transmission times, thereby requiring time increments, which sample the wave signal in the time domain into discrete values, to be small enough to capture the wave motions accurately. This corresponds to the requirement posed by the sampling theorem in the frequency domain, such that the sampling frequency should be at least twice the eigenfrequency according for a stable solution from the finite element model; and it sets the upper bound for the time step size Δt in the time domain. On the other hand, the lower bound of Δt in a dynamic, explicit finite element model is governed by the time it takes the fastest strain wave - typically the longitudinal wave - to travel between two nearest nodes within the model. Therefore in total, the time step Δt should always satisfy the following relationships mathematically:

$$\frac{H}{c_1} \leq \Delta t \leq \frac{2}{\omega_{max}} \tag{2.12}$$

where H is the smallest element size, c_1 the longitudinal wave speed, and ω_{max} the maximum eigenfrequency of the finite element model. It needs to be noted that because high sampling frequency is required to capture the wave signal well in the model, Δt has to be very small (in fact, it is chosen to be much smaller than the upper

limit); as a result, the element size H also needs to be extremely small to enable such Δt to be chosen. This is the reason why the mesh in the model has to be extremely fine for the data interpretations.

The element type in our model is the linear cubic element C3D8R (comparison with higher-accuracy elements is addressed in the latter parts), which makes the distance between two nearest nodes equal to the dimension of the element. The time step size is therefore largely governed by the element dimension such that extremely small time steps require extremely fine meshes. In the simulations here, the nearest node to node dimension is set as 0.03 μm and the finite element model contains $30 \times 30 \times 300$ elements, with each crystal containing $5 \times 5 \times 5$ elements.

- **Boundary conditions**

In ultrasonic wave testing, a longitudinal or shear wave applied at a sample surface by the transducer transmits through the sample (but with some reflection, scattering and attenuation), reaches a far surface, and is reflected back and received by the transducer. The transducer is typically very much smaller than the sample itself, making the detection a localized process; in fact, it is normally assumed that the majority of the wave energy generated by the transducer propagates only uni-axially in the sample, and, as a first approximation, is contained within a tunnel-like region whose diameter is of approximately the same size as the transducer, as shown in Figure 2.3.

This tunnel-like region, which is constrained by the surrounding material, is the counterpart of our RVE model. Therefore the boundary conditions applied to the outer faces of the representative finite element model, which are all parallel to the wave direction, are specified such that all points on the outer surface are constrained to have zero x- and y-direction displacements. This double plane-strain condition means that the waves within the model behave as if both the excitation source (the

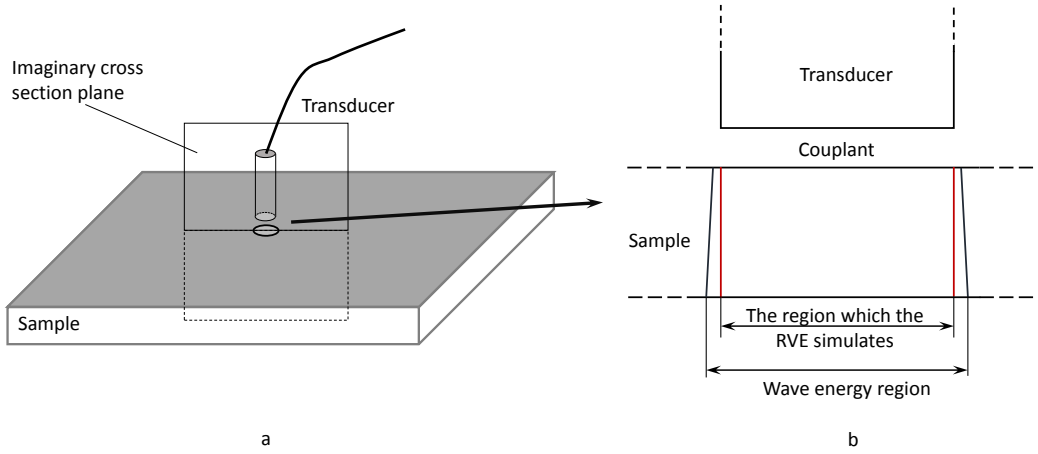

Figure 2.3: The tunnel-like region in which the majority of the wave energy is confined, and which the RVE model simulates.

transducer) and the material are infinite in the spatial dimensions normal to the propagation direction (x and y). Although this is clearly an approximation, such an assumption is known to work extremely well in the modelling of real ultrasound waves propagating through solids. In addition, the far end surface in the simulation model is the counterpart of the reflection surface in the experimental sample and is set as a free surface. Experimental results suggest that representative ultrasonic wave reflection does not show significant change in magnitude nor wave shape distortion [63, 84], which supports the imposition of the uni-axial boundary conditions described.

- **Ultrasonic wave loading**

In the model, ultrasonic waves are excited on the near end of the sample shown in Figure 2.2a as pressure variations whose amplitudes change as two cycles of high-frequency sinusoidal waves in a Hanning window, as shown in Figure 2.2b. The frequencies of the exciting waves are set to be representative of the mainstream test frequency span used in the industry, ranging from 2 MHz to 6 MHz, and the magnitudes of the waves in all frequencies are arbitrarily (since linear elasticity is assumed) set to be 1 MPa. The plane on which the pressure is applied is shown schematically by the face with the black border in Figure 2.2c.

The wave in the bar comprises longitudinal travelling stress waves resulting from the pressure loading. The loading is chosen as two cycles of sinusoidal waves in a Hanning window because: (a) it is a typical excitation signal used in the industry; (b) compared with a square window and some other windows, the bandwidth of the Hanning window is much narrower, and (c) the narrow bandwidth of the Hanning window also limits the distortion of the shape of the travelling wave resulting from dispersion and makes the capture of wave peaks and subsequent calculation of the wave speeds more accurate. The dispersion of the ultrasonic wave signals during propagation may also be affected by the relationship between wavelength and the characteristic grain size. The wavelengths in our model range from seven to twenty times that of the grain size in the 2-6MHz frequency span, such that dispersion effects remain small (see later).

- **Results extraction**

Once an ultrasonic excitation wave has been introduced in to the model, it is necessary to track its transmission through the polycrystal sample and to determine the average wave speed. In order to do so, three measurement planes are established, as shown in Figure 2.2c by the dark faces, which are defined as node sets whose velocities and stresses are traceable at every time step during the analysis, with the distances between neighbouring planes fixed. The planes are located at least one length of the applied wave away from either end of the bar, in order to avoid interferences between incident waves and reflections.

Figure 2.4 shows a typical stress response at the nodes on one of the measurement planes in Figure 2.2c in a random-textured polycrystal model at the time when the wave peak arrives at this plane. Comparison is drawn between two element types in the figure but it can be seen in both plots that by the time the travelling wave reaches this measurement plane, the wave is itself no longer perfectly planar as a result of the combination of grains with differing crystallographic orientations through which it

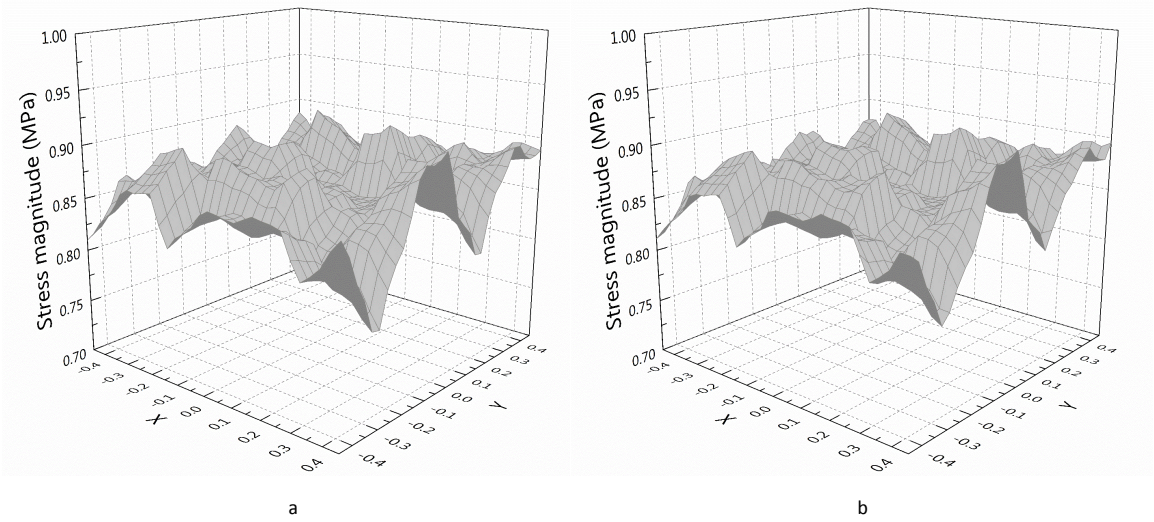

Figure 2.4: Axial stress magnitudes at the nodes on the second measurement plane (shown in Figure 2.2c) when the compressive stress wave peak arrives. The texture in this model is chosen to be random. In this figure (a) shows the results by using C3D8R element type, and (b) by C3D8.

has already passed. Once at the measurement plane, the absence of wave planarity is then enhanced by the various crystallographic orientations within the plane; as shown earlier, the asymmetry of a typical HCP crystal is capable of generating wave velocity differences of up to about 500 m/s by virtue of its crystallographic orientation alone. The axial stresses at the measurement plane are then averaged to give the ensemble response with time.

The ensemble average stresses over all the nodes on the measurement planes at each time step provide discrete axial stresses and how they vary with time as shown by the symbols in Figure 2.5 at two measurement planes. However, in order to best capture the corresponding wave peak point time, the calculated waves are fitted using a sinusoidal function to give the best representation of the time at which the wave peak intersects with the measurement planes. In this way, wave speeds through the polycrystal ensemble are determined by considering wave time of flight between the measurement planes as shown in Figure 2.5.

Knowledge of the times of interaction of the waves with the three measurement planes

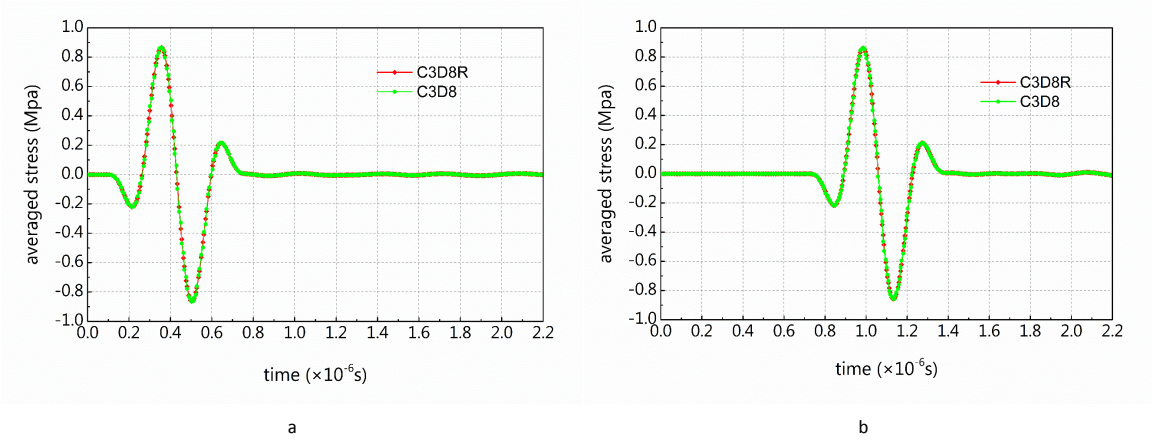

Figure 2.5: The responses to the compressive stress wave of (a) the first and (b) the second measurement planes across the wave history. Each discrete point in the figure is obtained by averaging the stress magnitudes of all the nodes on that plane at that time step, and the solid line indicates a sinusoidal fit to these data. Results obtained with two element types are shown: red for C3D8R, and green for C3D8.

then allows velocities to be determined. This is repeated over ranges of input frequency in order to generate phase velocity versus frequency and hence dispersion diagrams where necessary.

Figure 2.4 shows that despite the different element types, the stress responses and distributions on the tracked plane show no distinct differences, and the averaged stress changing with time for the two element types almost overlap with each other in Figure 2.5, which results in less than 1 m/s difference in the calculated wave velocity. These have in effect demonstrated (and will continue to be proved in the following parts) that the combination of the chosen element size and element type C3D8R is adequate for capturing the wave speed accurately. Even though the stress distribution in Figure 2.4 is not entirely smooth, averaging across the whole plane to obtain a single value for the time step has largely diminished the localisation effects. Therefore in the following parts of this thesis, I continue to adopt the mesh size of 0.03 μm and element type of C3D8R for both accuracy and efficiency. However, if focusses are laid upon the planar stress distribution rather than the wave speed, finer mesh and higher-order element types are recommended.

It is noticeable in Figure 2.5 that the amplitude of the averaged stress on the tracked plane is no longer equal to 1MPa as is the input signal. This is mainly because of the reflection of the wave energy occurring on the grain interfaces caused by the different elastic moduli of the neighbouring grains, which will be discussed in further details later in Section 2.1.3. The fluctuation of the averaged stress in Figure 2.5 after (as opposed to being perfectly flat before) the wave has arrived is the proof of such reflections that cause a fraction of the wave energy to be reflected back and forth in the propagated region, rather than travelling along with the major envelop of the wave energy.

Another important point about this simulation technique is that by calculating the average transmission wave speed across the RVE model, the wave speeds are directly resulting from the various overall collective crystallographic texture, whereas the information of morphologies and grain arrangements etc. are discarded.

- **Configuration of grain orientations in the model**

There are up to 2160 crystals in this polycrystal model, and the orientation of each grain is applied individually for the whole model to display overall collective textures; as ultrasonic waves, which are elastic waves, are the sole interest of the studies in the thesis, the orientations are applied in association of elastic stiffness matrix only and no plastic anisotropy is considered.

Crystallographic orientations are defined as the configurations rotated away from the global sample system used for defining wave loading and boundary conditions, and they are specified either by a set of three Euler angles, (α, β, γ), or four quaternions, (q_0, q_1, q_2, q_3). The corresponding 2nd order rotation tensor (which may be written as a 3×3 rotation matrix) $\mathbf{r}$ required to rotate 2nd order tensors from the global sample system to the local crystal system can be directly calculated from the Euler angles or quaternions. The tensor $\mathbf{r}$ can also be employed to rotate the 4th order elastic tensor

C to the required orientation **C'** using the following equation [85]:

$$C'_{ijkl} = r_{im} r_{jn} r_{kp} r_{lq} C_{mnpq} \tag{2.13}$$

Equation 2.13 may be written in a more compact, matrix-multiplication form if we note the 2nd order (such as stress and strain) tensors as vectors and their subscripts as

$$1 = 11,\ 2 = 22,\ 3 = 33,\ 4 = 23,\ 5 = 13,\ 6 = 12. \tag{2.14}$$

It is worth pointing out that the above convention is the most widely used simplification, but not the only one; for example, Abaqus/Explicit uses a different definition such that $4 = 12$ and $6 = 23$, and one must be wary of the difference to obtain the correct computational results.

With the help of the notation 2.14, the stiffness tensors may also be written in a 6×6 matrix form, and equation 2.13 can be proved to be equal to the following form:

$$\mathbf{C}' = \mathbf{R}\mathbf{C}\mathbf{R}^{\mathrm{T}} \tag{2.15}$$

where the matrix **R** is calculated from the components of the rotation matrix **r** via:

$$\begin{pmatrix} r_{11}^2 & r_{12}^2 & r_{13}^2 & 2r_{12}r_{13} & 2r_{13}r_{11} & 2r_{11}r_{12} \\ r_{21}^2 & r_{22}^2 & r_{23}^2 & 2r_{22}r_{23} & 2r_{23}r_{21} & 2r_{21}r_{22} \\ r_{31}^2 & r_{32}^2 & r_{33}^2 & 2r_{32}r_{33} & 2r_{33}r_{31} & 2r_{31}r_{32} \\ r_{21}r_{31} & r_{22}r_{32} & r_{23}r_{33} & r_{22}r_{33} + r_{23}r_{32} & r_{21}r_{33} + r_{23}r_{31} & r_{22}r_{31} + r_{21}r_{32} \\ r_{31}r_{11} & r_{32}r_{12} & r_{33}r_{13} & r_{12}r_{33} + r_{13}r_{33} & r_{13}r_{31} + r_{11}r_{33} & r_{11}r_{32} + r_{12}r_{31} \\ r_{11}r_{21} & r_{12}r_{22} & r_{13}r_{23} & r_{12}r_{23} + r_{13}r_{22} & r_{13}r_{21} + r_{11}r_{23} & r_{11}r_{22} + r_{12}r_{21} \end{pmatrix} \tag{2.16}$$

and of course one needs to swap the 4th and 6th row and column of **R** for the usage in Abaqus/Explicit because of its different simplification convention.

With knowledge of the orientations and rotation matrices for each one of the 2160 model grains, the anisotropic elastic stiffness with respect to the global sample system can now be determined for each crystal using equations 2.15 and 2.16, with the information of the crystal stiffness given in equation 2.10 and the rotation matrices; and the rotated stiffnesses are then implemented into the finite element RVE model for the solution process.

2.1.3 Primary studies on single crystals and grain boundaries

- **Single crystal studies**

The ability of the FE model established in the previous section to capture wave velocities accurately is examined here. In order to provide verification of the computational approach against the theoretical solution given by the Christoffel equation, two extreme single crystal cases, namely the reference configuration for which the wave propagation direction is parallel with the crystal c-axis, and configuration SC90 for which the wave propagation direction is normal to the c-axis, are incorporated by applying the uniform orientation on all crystals within the model. Both analyses have been carried out with a Hanning window of a sinusoidal wave over frequency range $2.0 < f < 6.0$ MHz, and the determined resulting wave phase velocities varying with frequencies are shown in Figure 2.6.

It can be calculated that the simulated velocities for the reference configuration (labelled SC for single crystal in Figure 2.6) and the SC90 are 6005 m/s and 5485 m/s respectively, in good accordance with those obtained from the solution to the Christoffel equation. The results show little sign of dispersion over the frequency range considered, but there are small variations in velocity, particularly for SC90 at the high-frequency end, likely due to the sample discretization (see the earlier discussion on the relationship between time-step and finite element size).

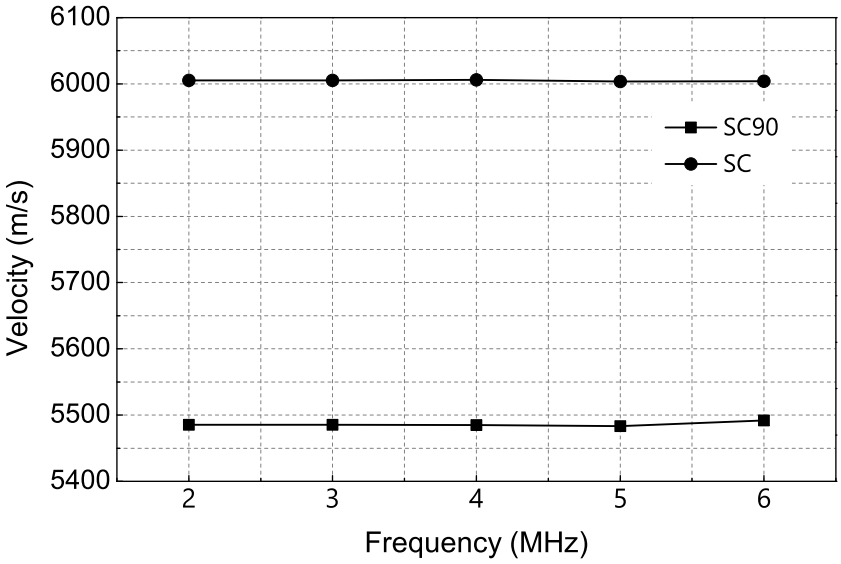

Figure 2.6: The simulation results for the two extreme cases of a single crystal Zr, SC and SC90.

In addition, these values of the two extreme cases also set the bounds on all possible ultrasound velocities in the context of the single-phase HCP polycrystals considered, and, as can be seen, the velocity range is greater than 500 m/s which is very large compared to what is now experimentally differentiable.

- **Grain boundary studies**

Now that the model has been verified for single crystal velocity simulations, another thing which needs to be investigated before stepping into studies on polycrystals is the influence of the way grain boundaries are treated in the model on the overall wave speed, which is examined here through the analysis on the interaction between two crystals.

The orientation changes among neighbouring gains in the simulation model are modelled as abrupt jumps, i.e. the grain boundaries are simplified to be zero-thickness interfaces; however, in reality, grain boundaries are essentially layers of certain thick-

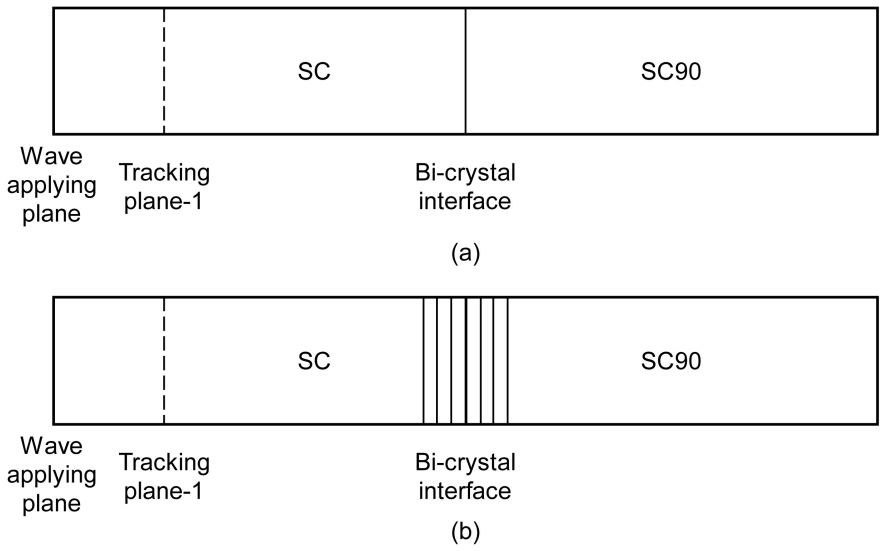

Figure 2.7: Schematics of the models with bi-crystal implemented. In (a) the grain boundary is modelled as a interface with an abrupt jump of orientation, while in (b) as layers with gradual orientation changes to simulate the grain boundaries appearing at boundaries in reality. The thickness of the grain boundary layers are not to scale.

nesses where the orientation of one crystal changes relatively gradually towards the neighbouring one; curvatures and dislocations that are commonplace at grain boundaries are not considered here, given the difficulties of modelling them and the fact that their influences on wave velocities are expected to be considerably smaller compared to crystallographic orientations. The effect of such simplified grain boundary layers is investigated by comparing the results of the two models shown in Figure 2.7, where the bi-crystals are both implemented by configuring the whole left and right halves of the simulation model with different orientations, but the grain boundaries are modelled in two ways: in Figure 2.7a the interface between the two crystals is left as an abrupt change, while in Figure 2.7b it is treated as a series of layers with orientations gradually changing from one crystal to the other to simulate the reality. The orientations for the bi-crystal are chosen to be SC and SC90 respectively, which form the largest possible velocity difference between two crystals hence can serve as an extreme case for the upper limit of the grain boundary effect.

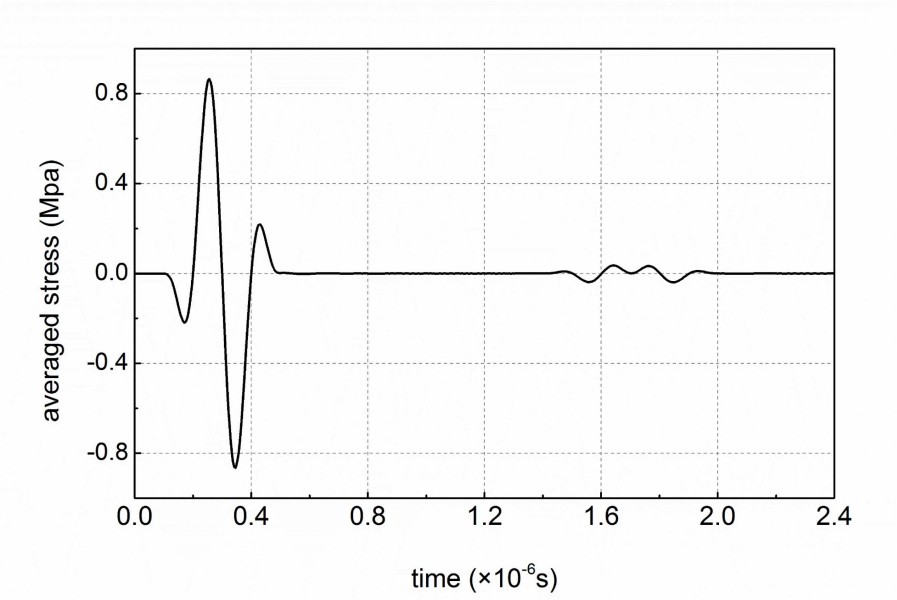

(a)

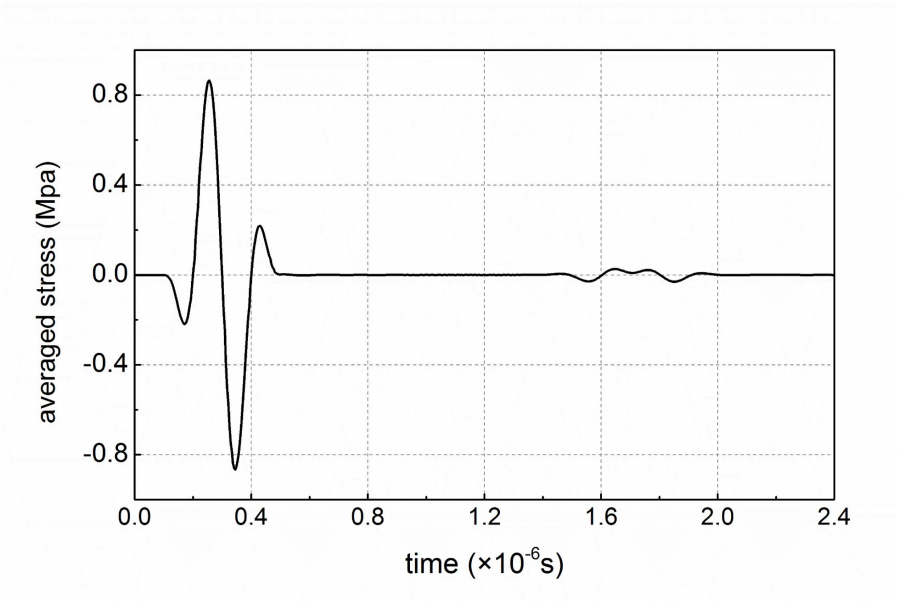

(b)

Figure 2.8: Time-amplitude plots obtained from the tracking plane-1 of the bi-crystal model in Figure 2.7a and 2.7b, respectively.

Simulation results of the average velocities across the whole model for the sharp and the gradually changing grain boundary implementations are respectively 5739.7 and 5737.5 m/s, and the difference between the velocities, at merely 2.2 m/s, is smaller

than the error level of both the computational model and the state-of-the-art ultrasonic experimental techniques (errors at ∼10 m/s), hence cannot be captured via either method. The wave propagations are tracked on the plane-1 in Figure 2.7 for both cases, and the corresponding relationships are plotted in Figure 2.8a and b respectively. There is hardly any difference in the wave responses of the two cases, except that the reflection wave for the gradual interface has slightly smaller amplitudes. Therefore it can be claimed that the ignorance of grain boundary thicknesses in the FE model has negligible effects on the longitudinal wave speeds.

There are two more implications to make: first, because the SC and SC90 orientation combination has the largest wave velocity difference, the introduction of grain boundary thicknesses to this combination should also set up the upper bound for the interruption on velocity for all cases; in other words, the ignorance of thicknesses for any other orientation combinations should cause velocity differences less than 2.2 m/s, which are also negligible. Moreover, it should also be noted that in reality, the wave incident direction is rarely perpendicular to the grain boundaries as constructed in the FE model, but is almost always in a certain angle with the latter. This complicates the wave propagation scheme by introducing refraction and mode conversion (a fraction of the wave energy converts between the longitudinal and shear modes), but as far as only the longitudinal wave speed is concerned, it is still similar with the grain boundary thickness study, where a fraction of the wave propagates across the boundary in the form of longitudinal wave and no lags are caused to it despite of the mode change and reflections happening at the interface. Therefore making the grain boundaries always perpendicular to the wave propagation direction in the model should not introduce significant error to the calculated velocities either.

So far in this section, the anisotropy of an HCP crystal has been revealed by the Christoffel equation in terms of its ultrasonic wave velocities; an RVE FE model has also been established to accommodate a large number of grains for the dynamic elastic

analysis on ultrasonic wave propagation in polycrystals; and the model has been fully verified through single crystal simulations and it has also been proved that the way in which grain boundaries are dealt with in the model does not introduce measurable errors. Therefore the model is ready to be used for polycrystal studies to be carried out in the next section.

SECTION. 2.2

The Forward Studies I: Computational Analyses of Polycrystalline Ultrasonics

In this section, the FE model established and calibrated previously is utilized to study wave velocities through polycrystals with different textures, in order to examine the potential for a ultrasonic measurement technique for the detection and ideally quantification of bulk three-dimensional HCP textures and (hopefully) Ti alloy macro-zones to be developed. Firstly, the way polycrystalline textures are represented in the model is shown, and the single crystal responses studied in Section 2.3 are considered to benchmark the methodology and set the bounds on expected ultrasonic velocities. This is then followed by consideration of a polycrystal with random texture, and a modified polycrystal model which contains a macro-zone. I then go on to address a range of standard Zr alloy textures in order to establish whether ultrasound has the potential to differentiate these textures, hence providing the possibility for ultrasonic texture determination.

2.2.1 Texture Representation in the Polycrystal Model

The FE model is capable of incorporating a maximum of 2160 independent grains in each of which a uniform crystallographic orientation may be specified, hence it becomes possible to model single crystal behaviour through to highly textured polycrystals and in this section, the methodology for assignment of crystallographic orientation is presented. The orientations which need to be assigned here come from either software (e.g. output from a texture analysis or the generation of random textures) or from EBSD measurements, and in both cases the allocation of crystallographic orientations is carried out subject to the limitation of a maximum of 2160 grains in the model. In the former case, grain orientations are binned according to spatial

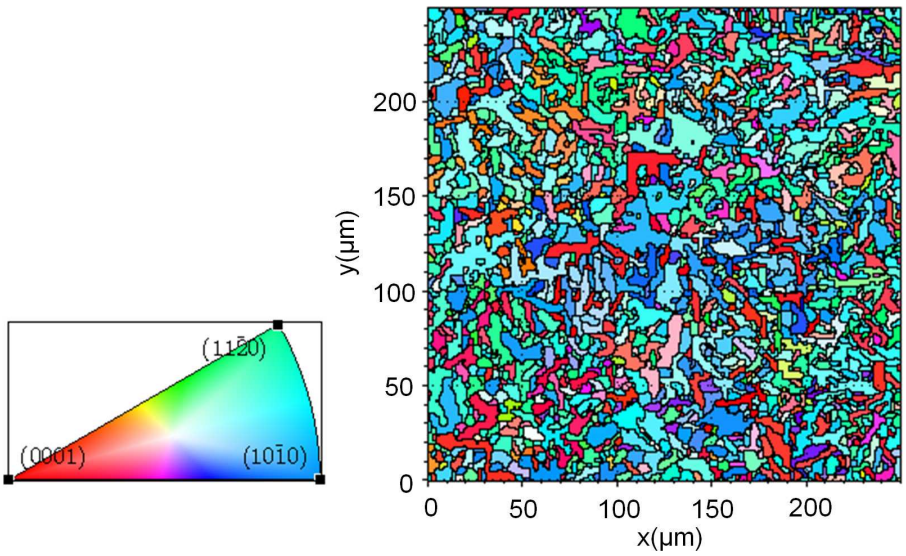

Figure 2.9: The crystal orientation map of the Zr-Random texture obtained from surface EBSD scans, with the colour coding shown in the left.

frequency, and the allocation of grain orientation in the model made in order to reproduce the area fraction distribution of orientations provided. In the case of EBSD data, it is first necessary to bin orientations into grains (e.g. using a misorientation thresholding to divide grains), so that an average orientation is obtained for each grain after which allocations to model grains are made as described already. The extreme but simplest texture is that for a single crystal in which all grains in the model are allocated the same orientation, as having been studied in Section 2.1.3.

A typical EBSD map for a Zircaloy4 alloy is shown in Figure 2.9 and the corresponding (0001) ODF representation of the texture is shown in Figure 2.10a [86]. This texture is referred to as the Zr-Random texture. The methodology described above for the polycrystal model representation of this texture has been applied and the corresponding ODF figure thereby giving the finite element polycrystal model representation of that texture is given in Figure 2.10b, showing a reasonable representation of the EBSD-obtained texture in Figure 2.10a.

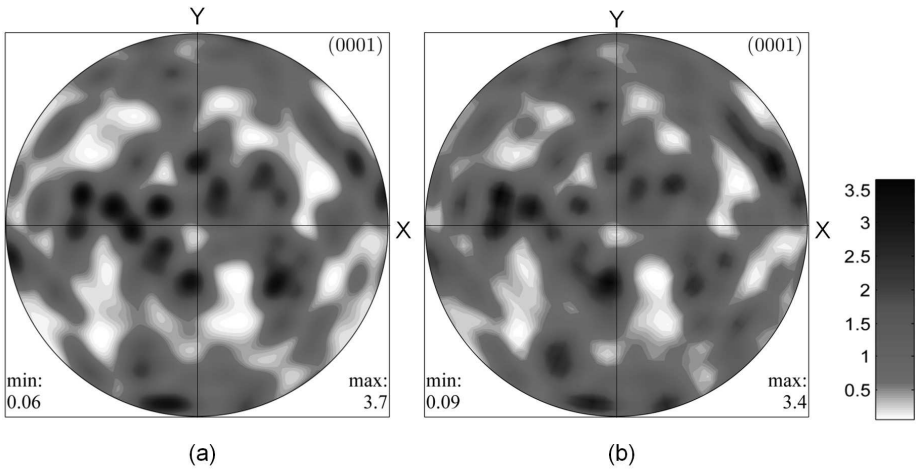

Figure 2.10: ODF figures for the Zr–Random texture (a) obtained from surface EBSD and (b) after averaging for the finite element representation.

2.2.2 Random and Non-random Textures and Macro-zones

The two extreme single crystal cases studied in Section 2.1.3 are employed here as the bounds on all possible ultrasound velocities. And similarly with the parameters used before, all the analyses in this section are also carried out with a Hanning window of a sinusoidal wave over frequency range $2.0 < f < 6.0$ MHz, with the exception of the following analysis in which frequencies up to 14 MHz (resulting in wavelengths 2.3 - 16.6 times of the grain size) were included in order to investigate dispersion effects.

In the computational results for the two single crystal cases in Figure 2.6, little sign of dispersion over the frequency range was shown, and the velocity variations particularly for SC90 at high-frequencies should be ascribed to sample discretization. Here in order to investigate dispersion effects further, the polycrystal model shown in Figure 2.2 with a random crystallographic texture subject to ultrasonic excitation with frequency up to 14 MHz is considered. The results are shown in Figure 2.11. It can be seen that although there do exist decreases in phase velocity with frequency, indicating dispersion, it only becomes noticeable at higher frequencies for which the wavelengths are getting close to the grain size. However, dispersion effects are seen

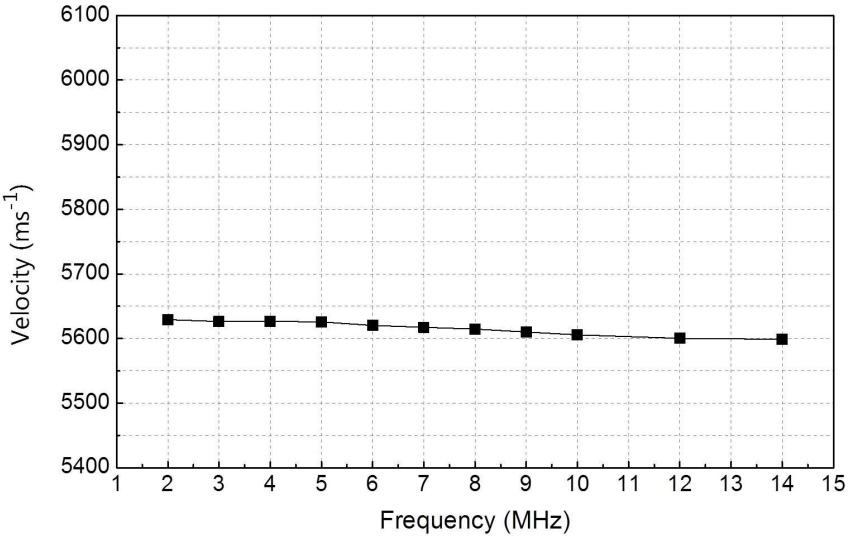

Figure 2.11: A typical dispersion curve for a computer generated random texture in the frequency span of 2 to 14 MHz.

to be small in the frequency range 2∼6 MHz. The subsequent results also reinforce that in this frequency range there is practically no dispersion.

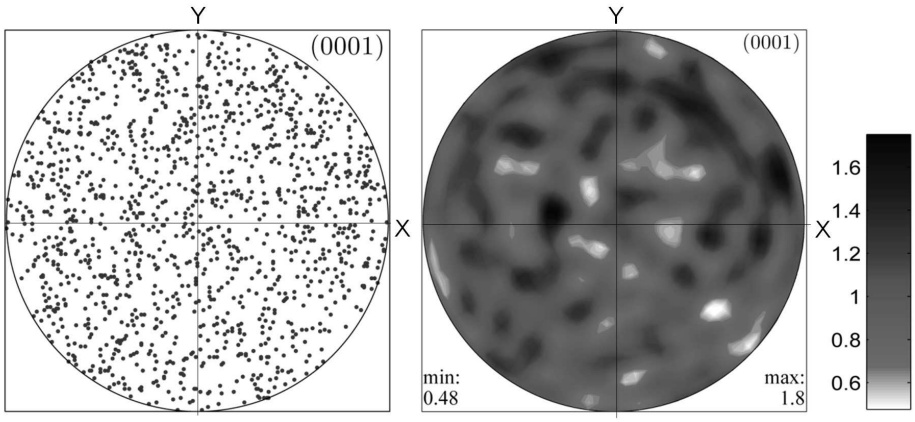

Figure 2.12: The Pole and ODF figures for the computer-generated random texture.

A polycrystal is considered next for which a range of ten (computer-generated) random textures are imposed in the RVE. The (0001) pole figure and ODF for one of these textures are shown in Figure 2.12, which have been homogenized as discussed above in order to generate the RVE with 2160 independent crystallographic orientations in order to represent this texture. The ultrasonic wave velocities for the differing

random texture realizations are not the same, while similar, but distribute within a small region. This region, plotted as grey shadows in Figure 2.13 along with the benchmarking single crystal results, shows upper and lower bounds of the ultrasonic wave velocity for the range of random textures considered.

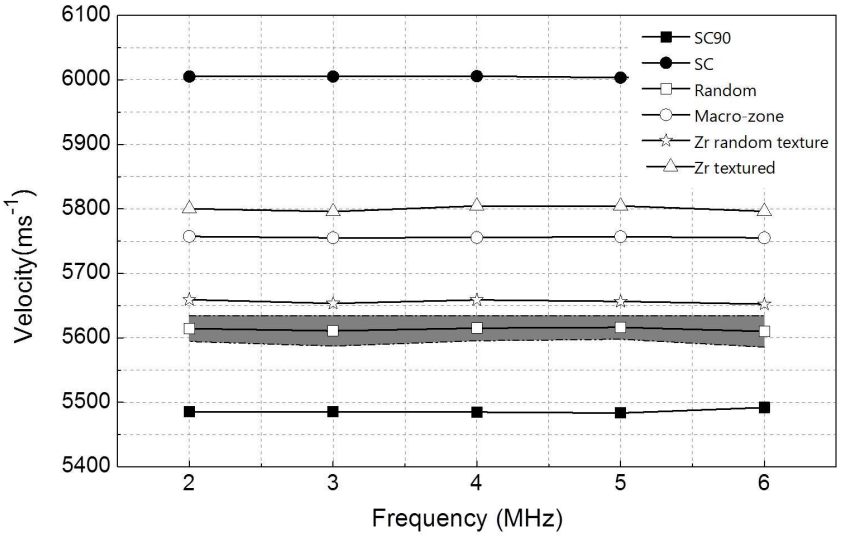

Figure 2.13: Calculated ultrasonic wave speeds for differing textures, of which: SC: single crystal; SC-90: single crystal with $\theta = 90$ deg; Random: computer generated random orientation distributions; Macro-zone: computer generated random orientation distribution with the central part of the model RVE configured with uniform crystallographic orientation; Zr random texture and Zr textured: two experimentally obtained textures, the former randomly distributed while the latter has (0001) as the preferred orientation.

A further nominally random texture, but in this instance with orientation data obtained from EBSD and corresponding to that already discussed and shown in Figure 2.9, has also been analysed and is included in Figure 2.13 and labelled Zr Random texture. This is close to the numerically generated random texture ultrasound response, but nonetheless different. However, the differences simply result from the fact that a nominally random measured texture is not necessarily random in the numerical sense, and that in fact, small deviations from numerical randomness can generate measurable differences in ultrasonic wave speed.

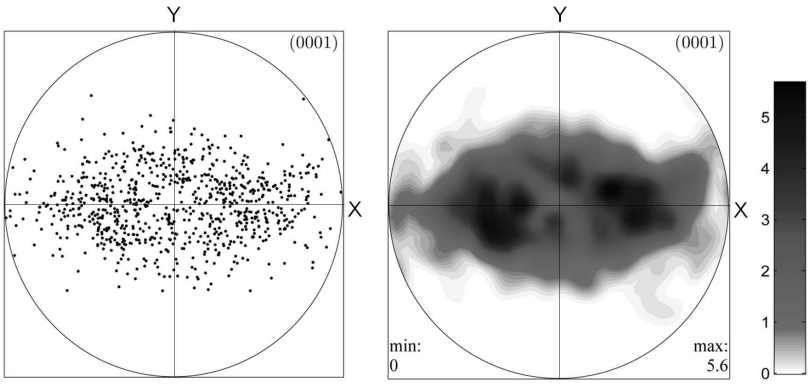

Figure 2.14: The Pole and ODF figures of the 'Zr textured' polycrystal from surface EBSD scans.

In order to demonstrate the very profound ultrasonic differences between nominally random and textured polycrystals, one further very particular Zr texture is considered next which is shown in Figure 2.14. This texture was obtained from EBSD and shows moderate orientation of crystal c-axes towards the wave propagation direction such that an overall wave velocity closer to the single crystal SC orientation is expected. This is what is calculated and shown in Figure 2.13 with a clear separation from both the single crystal (SC) behaviour and the random polycrystal behaviours (Random and Zr Random Texture). The ultrasonic velocity differences are substantial (> 150 m/s) and easily measurable.

Finally, in this section, the focus returns to macro-zones, particularly relevant in Ti aero-engine alloys, which manifest as regions of approximately uniform crystallographic orientation of a size normally more than ten times the nominal grain size. After component processing, macro-zones in their own right are not strictly considered defects, but much work in cold dwell fatigue has demonstrated that they are precursors for the formation of large facets which may go on to fatigue crack propagation. Their detection, therefore, within formed components is of considerable importance. Moreau et al [87] have recently demonstrated the success of ultrasonics in macro-zone detection, at least for a known macro-zone occurring on a free surface such that the

approach could be validated by EBSD. In their analysis, they assumed the ray tracing approximation and it is addressed here whether this is a reasonable assumption. The generic macro-zone detection within the bulk of a polycrystalline texture using ultrasonics is also considered. An SEM and EBSD image of a macro-zone in a Ti alloy is shown in Figure 2.15a, along with its representation in the RVE model in Figure 2.15b.

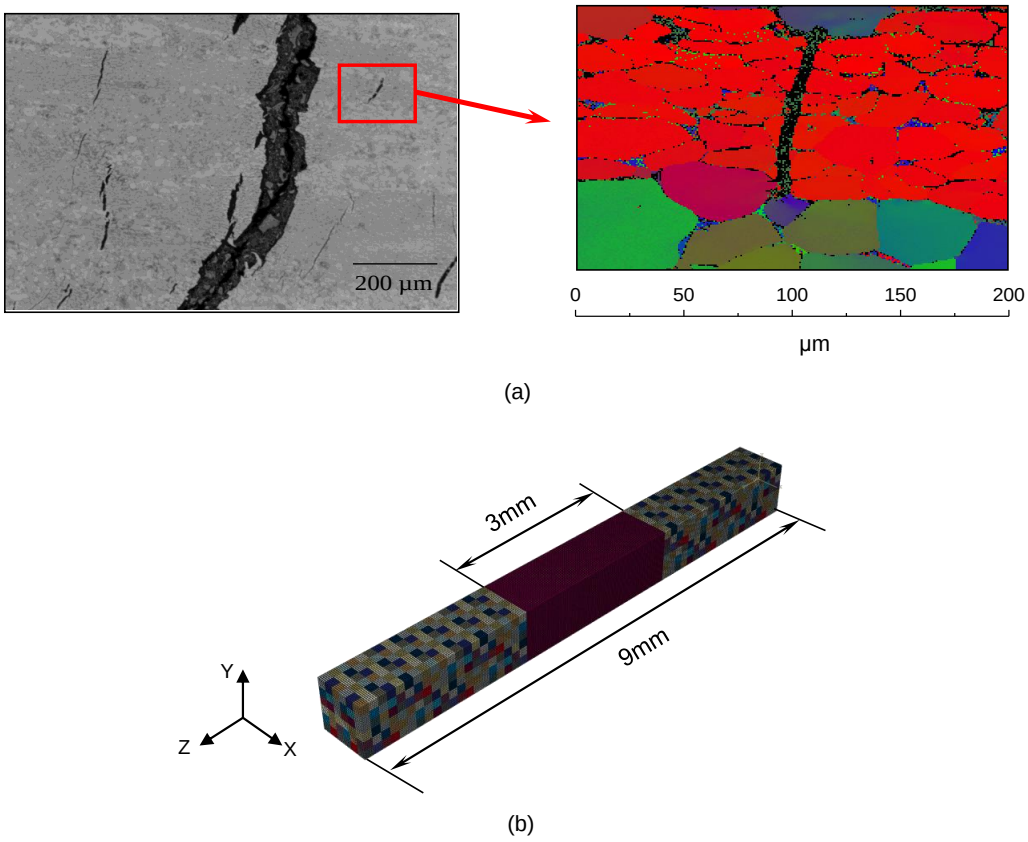

Figure 2.15: (a) An exemplary microscopic observation of a macro-zone obtained from EBSD [88], where the large central region of crystals with the same red colour (representing the same crystallographic orientation) indicates the macro-zone, and (b) the configuration of the macro-zone in the RVE; the two ends of the RVE are assigned random texture, while the crystals in the central part, representative of the macro-zone, are assigned the same orientation.

In the latter, a representative region of uniform crystallographic orientation within the central region of the RVE is incorporated. Initially, the orientation is such that

the macro-zone crystallographic orientation has its c-axis parallel to the wave propagation direction of travel, but the effect of macro-zone orientation is considered in more detail later. The ultrasonic response is shown in Figure 2.13 in which again, differentiation from the response observed for single crystals, random polycrystals and textured polycrystals is evident.

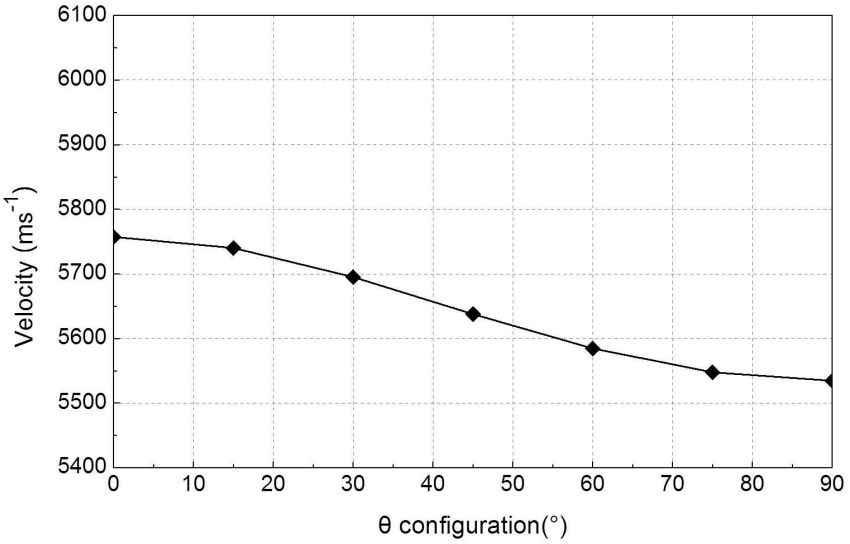

Figure 2.16: Wave velocity changing with the crystallographic orientation of the macro-zone embedded within random polycrystals.

However, changes in the crystallographic orientation in the macro-zone cause the overall wave velocity to change. In order to investigate its effect, seven different orientations are specified in the macro-zone, in which the c-axis of the crystal is taken to be parallel to the wave propagation direction ($\theta = 0$ deg) through to that in which the c-axis is perpendicular to the wave propagation direction ($\theta = 90$ deg). The change of configuration introduces a significant shift of wave velocity with a difference of near 200 m/s, as shown by Figure 2.16, and this property enables the presence of macro-zones to be differentiated clearly from random textures if multiple measurements are performed in various directions.

2.2.3 Arbitrary Zr textures

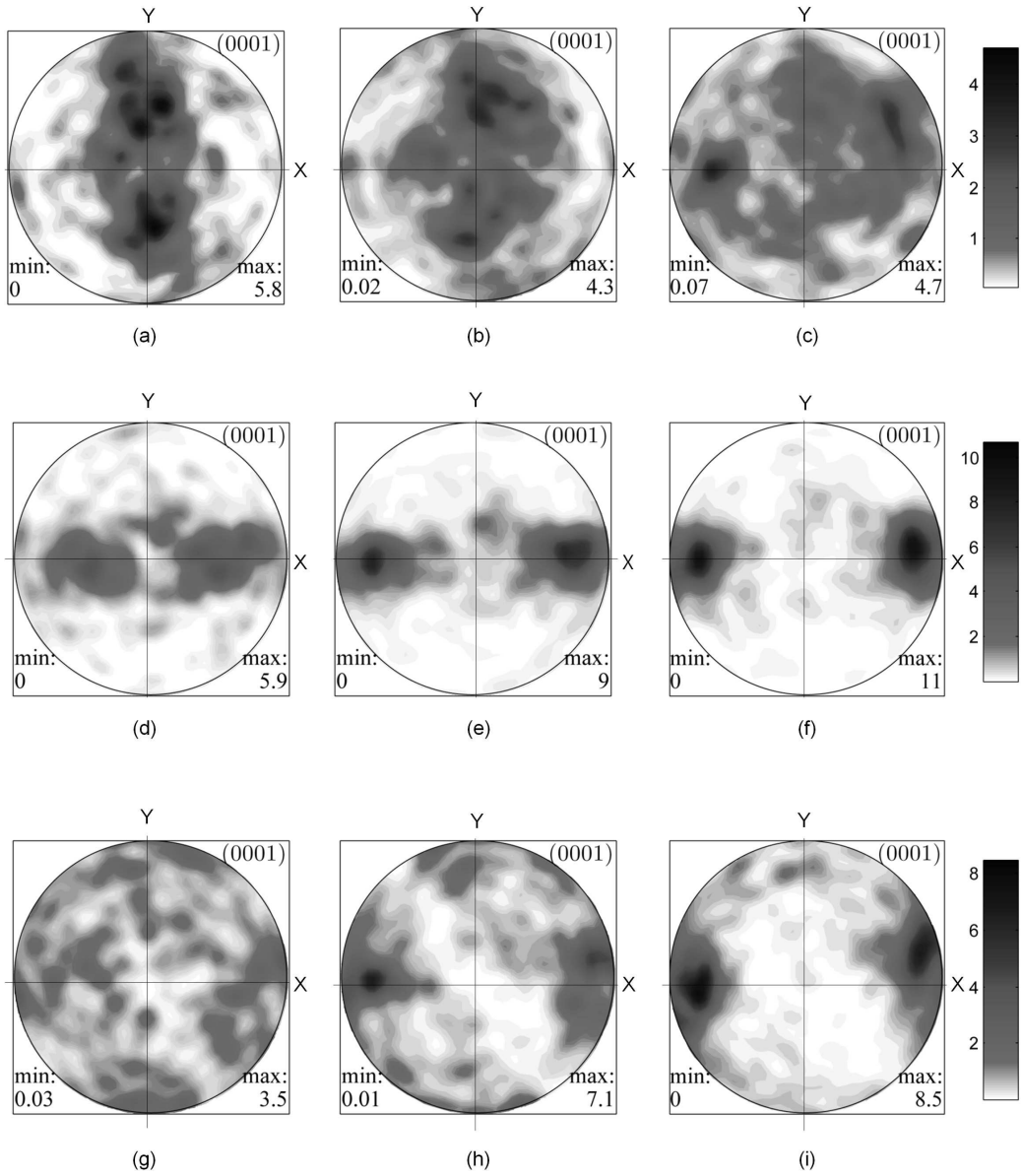

Figure 2.17: Nine different representative Zr alloy textures.

The analyses so far have been concerned with what might be considered rather extreme examples in texture analysis: textures that are rather special being single crystal, random, highly textured or containing a macro-zone. In this section, however, I address a range of intermediate and unremarkable Zr textures in order to determine again whether differentiation between them and ultimately, identification

might become a possibility using ultrasound. Nine further textures (obtained from the combination of experimental measurements and computer simulations of texture development in Zr alloys [89]) are considered, characterized by their pole figures, shown in Figure 2.17 and labelled textures (a) through (i) (textures a, d and g are obtained experimentally, and the subsequent pole figures in the same row with them are obtained from computer simulations).

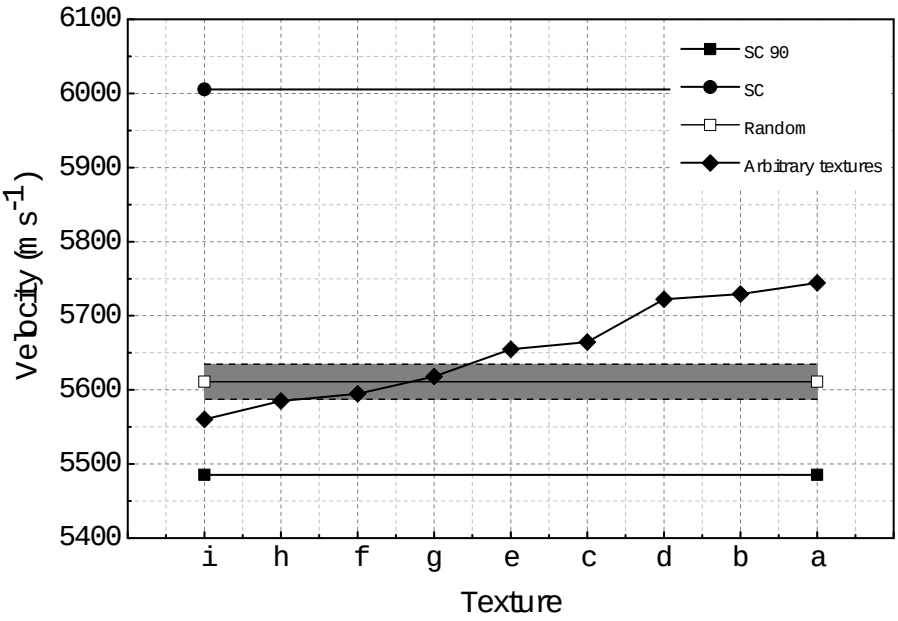

Figure 2.18: Ascending order of ultrasonic response of nine arbitrary Zr textures, with the grey zone showing the velocity region for random textures (n.b.: all velocities in this figure are for waves of 3 MHz frequency, so the symbols on SC, SC-90 and Random lines do not mean simulations performed at the dot positions but are for differentiating purpose only).

Examination of the pole figures may well lead to some speculation on the appropriate ordering in terms of respective ascending ultrasound wave speed; naturally, the higher the proportion of grains with c-axes parallel to the wave propagation (z-) direction leads to the higher wave speed. All of these textures have been analysed using the RVE ultrasound technique and the results obtained in texture order are shown in Figure 2.18. For context, the figure also includes the single crystal bounding and ran-

dom polycrystal wave velocities. Some of the arbitrary texture ultrasound velocities therefore intercept that for the random texture (unsurprisingly given the broad range of textures examined), but are all largely removed from the extreme single crystal velocities. Also, the velocity range for the textures considered is quite large, at about 200 m/s; these are magnitudes of differences easily detectable with ultrasound.

To conclude this section: studies have been carried out through the dynamic elastic FE model on the ultrasonic wave velocities of a whole range of different textures, including computer-generated random textures, macro-zones, experimentally obtained random and textured textures, and a series of non-distinguished textures. The computational results are all positive, suggesting that subtle changes in polycrystalline texture cause the wave speeds to differ; and for a majority of examples shown, the amplitudes of these differences are well above what the latest experimental techniques can tell.

SECTION. 2.3

The Forward Studies II: Experimental Investigations and Validations

The ultrasonic wave velocities have been proved via systematic simulations to be significantly different in HCP (with Zr used as an example) polycrystals with different textures. In this section, the relationship between wave speed and texture is investigated with experimental techniques such as EBSD and conventional ultrasonic scans. Two polycrystalline Ti-6Al-4V samples, which have undergone different manufacturing processes hence supposedly have rather distinguished textures, are the subjects of the experimental study. Their three-dimensional textures are firstly fully characterised by EBSD measurements on surfaces perpendicular to the rolling, transverse and normal directions respectively; and inputting the obtained texture information to the established FE model gives the predictions of the wave velocities in all the three directions; then the conventional ultrasonic scans are carried out in all directions as well, and the average experimental velocities are obtained. Ultimately, comparisons are conducted between the predictions and experimental results of the wave velocities, which not only provide additional verifications for the accuracy of the FE model, but also show the explicit experimental proof of how significant the coupling between wave velocity and polycrystal texture is.

2.3.1 Application of the Method to Two-Phase Titanium Alloys

All of the computational studies carried out in the previous section are for single-phase zirconium alloys, but in this section, two-phase titanium alloys are considered in which the presence of the BCC beta phase is explicitly incorporated. In the following, the computational studies are performed for Ti-6Al-4V alloy, a typical commercial alpha+beta titanium alloy, with beta phase volume fraction of about 10% at room

temperature. The elastic moduli of both the alpha and beta phases of Ti-6Al-4V are listed in Table 2.1 [90], together with comparison to those for the alpha zirconium.

Table 2.1: Single crystal elastic moduli of Zirconium and both phases of Ti-6Al-4V [90]. C_{ij} is in GPa. For Zirconium and α phase Ti-6Al-4V, $C_{66} = (C_{11} - C_{12})/2$.

	C_{11}	C_{12}	C_{13}	C_{33}	C_{44}
Zirconium	136.0	78.0	68.0	163.0	40.0
Ti-6Al-4V(alpha phase)	170.0	92.0	70.0	192.0	52.0
Ti-6Al-4V(beta phase)	138.0	108.0	-	-	51.0

The implementation of the beta phase into the computational model is carried out by specifying the corresponding beta phase elastic moduli in a given number of model crystals, in order to represent the measured volume fraction of beta phase contained within the alpha-beta polycrystal. The alpha and beta phase crystallographic orientations are specified within the model in order to reproduce the results of EBSD measurements on uni-directionally and cross-rolled Ti-6Al-4V plate, and the results of the ultrasound computational analyses are presented with the experimental studies together in the next section.

2.3.2 Experimental samples and characterizations with EBSD

Two samples, both of which are two-phase Ti-6Al-4V alloy, are fully characterized using EBSD and subjected to ultrasonic scans to enable their textures and ultrasonic responses to be analyzed respectively. One sample is uni-directionally rolled (UD), and its dimensions (length, width, thickness) in the x, y, z directions are respectively $49.80 \times 14.53 \times 7.50$ mm^3; the second sample is cross rolled (XR), with dimensions of $40.01 \times 38.88 \times 8.29$ mm^3. According to literature [16], the uni-directional rolling process causes the majority of the c-axes of the HCP crystals to align along the

transverse direction, while the cross rolling results in preferred distribution along both rolling directions. Therefore, the orientation distributions of the two samples should presumably be similar with the respective sketches in Figure 2.19.

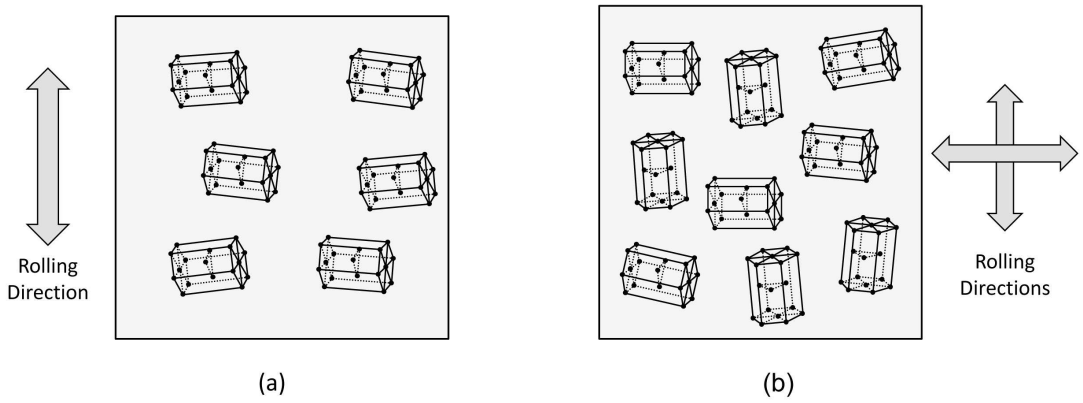

Figure 2.19: Sketches for the presumable orientation distributions for (a), UD sample and (b), XR sample according to literature [16].

EBSD studies are then carried out in three orthogonal planes on both samples to characterize the three-dimensional crystallographic orientations. These tests are performed on the Carl Zeiss EVO LS15 ESEM equipped by an EDAX EBSD detector. Before EBSD detection, the samples were grinded with silicon papers of grits in the order of 320, 600, 2000, respectively, which was followed by a polishing step using Gemini Diamond Slurry 9-micron monocrystalline with hydrogen peroxide for about 20 minutes, with the final step of polishing using colloidal silica with hydrogen peroxide for at least an hour. Two to three different regions are tested on each of the surfaces but only one representative result for each surface is shown in Tables 2.2 and 2.3, with the corresponding colour legend.

The EBSD examinations highlight the differences of textures in the two samples immediately; for the UD sample in Table 2.2, scanning direction 3 contains most of the crystal c-axes lying parallel to it, with its pole figure showing a very strong pole located in the centre, suggesting that this direction may be perpendicular to the rolling

Table 2.2: EBSD characterisation results of the UD sample: the grain map, pole figure and beta phase percentage

Scanning directions	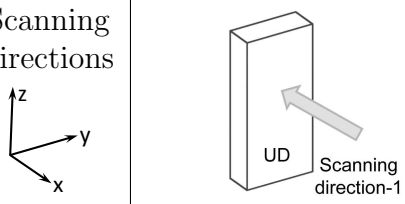	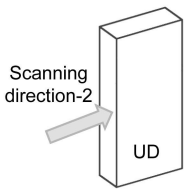	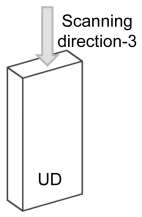
EBSD maps	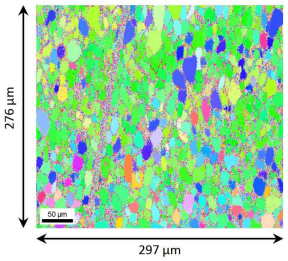	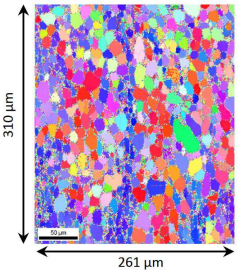	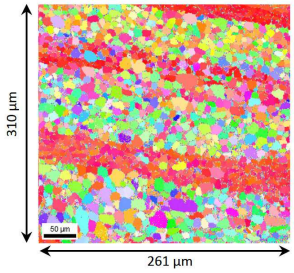
Alpha phase pole figures	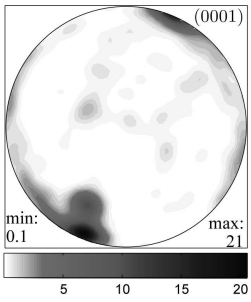	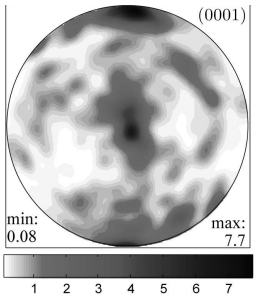	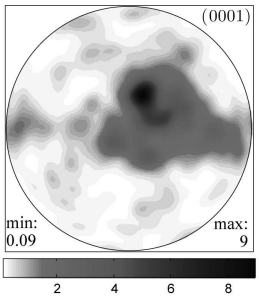
Beta phase percentage (%)	10.6	9.9	5.9

direction, i.e., the sample is rolled along the scanning direction-2; while the other two directions' pole figures tend to be less pronounced. For the XR sample, the scanning directions 2 and 3 have very similar grain maps and pole figures, reflecting the two rolling directions. In these pole figures, there is still a relatively strong pole distribution in the centre, but of course not as strong as for the UD sample. It is noteworthy that the EBSD analysis of the UD sample in Table 2.2 shows quite significant banding of orientation, particularly in the plane normal to the rolling direction.

Table 2.3: EBSD characterisation results of the XR sample: the grain map, pole figure and beta phase percentage

Scanning directions	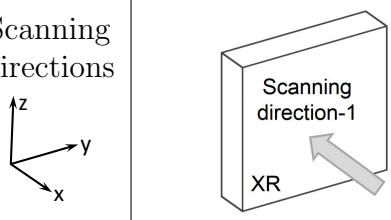	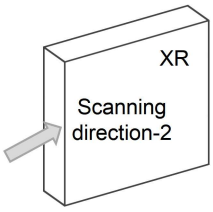	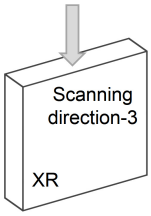
EBSD maps	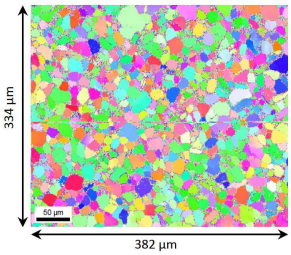	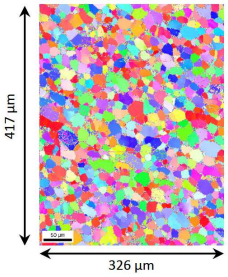	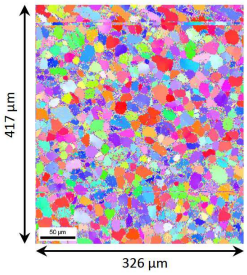
Alpha phase pole figures	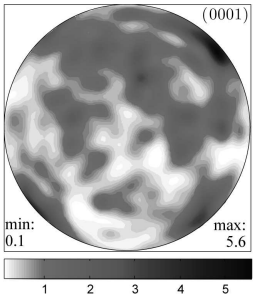	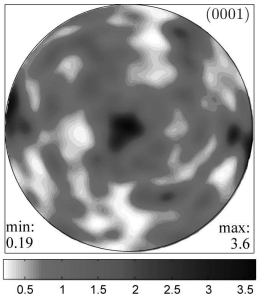	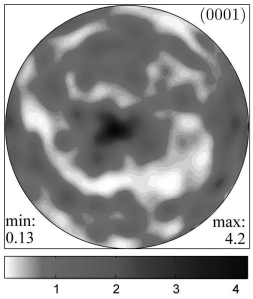
Beta phase percentage (%)	7.3	5.6	9.5

2.3.3 Conventional Ultrasonic Scans

The computational modelling above shows that the ultrasonic wave velocity in a polycrystalline bulk has a strong dependence on its texture, and since different rolling histories cause the textures to be quite different, it is anticipated that these differences are also reflected in the wave velocities. Hence conventional ultrasonic scanning is employed to determine the wave velocities in all orthogonal directions, in order to examine the ability for the ultrasonic method to differentiate differing textures.

- **Setup of the Platform**

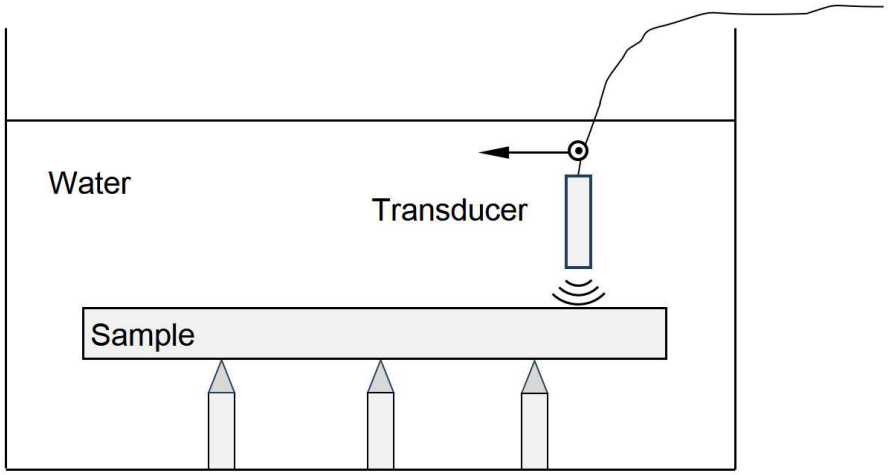

Figure 2.20: The schematic configuration of the ultrasonic scanning platform.

The schematic setup of the ultrasonic scanning platform is shown in Figure 2.20. The sample is immersed in a water tank and supported by a few sharp-ended levers to make the lower surface of the sample (known as the backwall) a free surface for the wave reflection. A 10 MHz transducer whose focal length is approximately 2.5 cm (1 inch) is used as both the wave source and the receiver to perform the scan, and is configured perpendicular to the sample surface and its focus located on the backwall.

- **Scanning Ultrasonic Velocity Results**

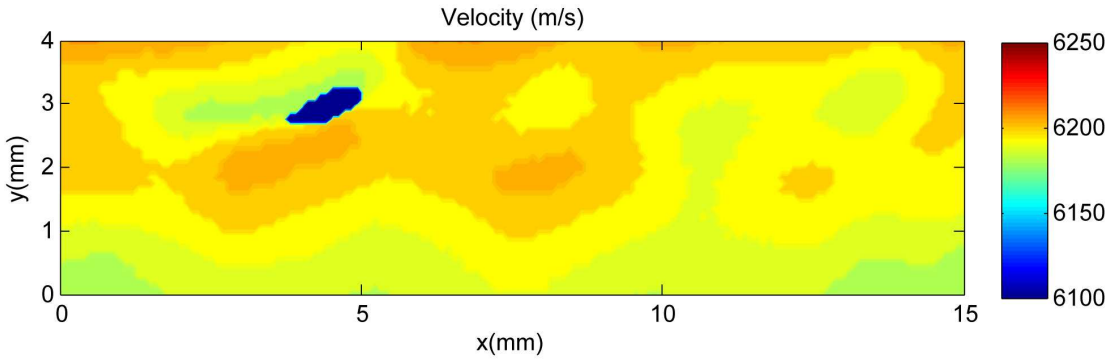

Figure 2.21: Ultrasonic wave velocity variation map in scanning direction 2 on the UD sample.

Ultrasonic scans are performed in all orthogonal directions on both samples, and Figure 2.21 shows one representative velocity map obtained in scanning direction 2 on the UD sample. The results suggest that there is generally good consistency of wave velocity values across the sample, with slight deviations resulting from local variations in crystallography apparent in Table 2.2. Indeed, as shown in Table 2.4, the variation of the wave velocities in any specific direction are relatively small.

Table 2.4: Ultrasonic scan results for both samples

Scanning directions	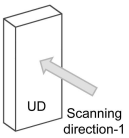	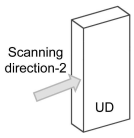	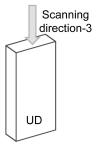	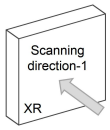	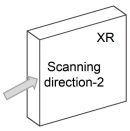	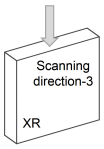
Min speed (m/s)	6160.9	6146.9	6332.3	6168.2	6225.2	6229.2
Max speed (m/s)	6181.2	6215.6	6378.3	6177.4	6297.7	6235.2
Avg speed (m/s)	6171.3	6190.2	6358.8	6175.2	6233.2	6232.8

In an earlier section of this chapter, the computational results of ultrasonic speed in single-phase random-textured Zr polycrystals were presented. Here, computations are presented for random textured, two-phase (12.5% beta) Ti polycrystals as outlined in Section 2.4.1, and the experimentally obtained results above are firstly compared with these, as shown in Figure 2.22. To make the comparison straightforward, all the computed results are shown in Figure 2.22 as constant velocity lines. The ultrasonic scan results are obtained with a 10 MHz transducer and are shown by points corresponding to the uni-directionally and cross-rolled samples for the wave directions shown in the figure. In connection firstly with the computational results, Figure 2.22 shows that the introduction of the beta phase into the random-textured alpha phase

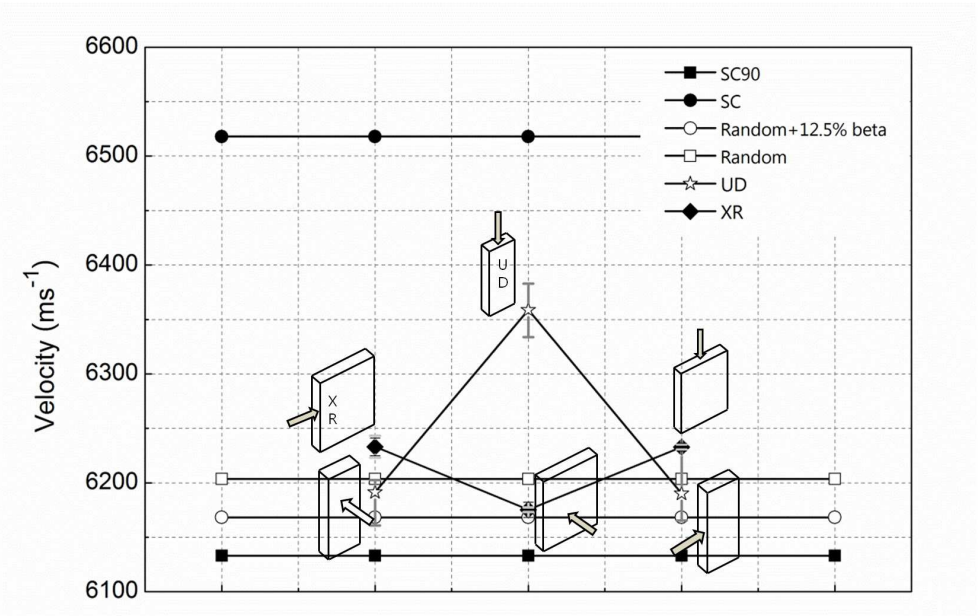

Figure 2.22: The layout of experimental results compared to simulation results (n.b.: all simulation velocities in this figure are for waves of 3 MHz frequency, so the symbols on SC, SC-90 and Random lines do not mean simulations performed at the dot positions but are for differentiating purpose only

distribution leads to an overall reduction in predicted ultrasonic velocity. The 12.5% volume fraction of the beta phase causes a velocity reduction of about 25 m/s. For the UD sample, the rolling direction leads to a much higher velocity than for the other two orthogonal directions, reflecting the strong UD texture, and puts the measured velocity well into the 'textured region' of the diagram, while the velocities in the other two directions for the UD sample both lie between the pure alpha random and alpha-beta (12.5% beta) lines. This highlights the expected velocity profile representative of a uni-directionally rolled sample. For the XR sample, the two rolling directions give velocities at about 55 m/s above the alpha-beta line, while the velocity in the normal direction 1 lies very close to the alpha-beta line. This also, therefore, provides an indicative profile representative of cross-rolled textures. The ultrasonic scan results therefore provide sufficient information to distinguish the two sample textures.

2.3.4 Explicit Model Representation EBSD-measured Textures and Comparisons of Predicted and Measured Ultrasound Velocities

In this part, the textures obtained by EBSD characterisation for the UD and XR samples are explicitly incorporated into the polycrystal model and the corresponding wave speeds calculated, and then compared directly with the ultrasonic scan test results, in order to provide verification, or otherwise, of the computational model.

The incorporation of the EBSD information into the model is carried out as follows. The alpha and beta phase regions are distinguished from the EBSD data, and the individual crystallographic orientations extracted and assigned to groups of elements in accordance with the methodology described in Section 2.2.3, making sure the appropriate volume fraction of beta phase is maintained. It should be noted that the areas over which EBSD scans were carried out with which the texture models were built are small relative to the regions over which the experimental transducer excitation is imposed. Hence, multiple EBSD scans on a given surface were carried out and incorporated in to the texture representation in the model.

Table 2.5: Comparison between ultrasonic velocities obtained directly from ultrasonic scans and those obtained by implementing textures from EBSD tests into the computational model

Scanning directions	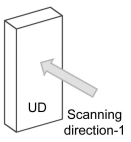	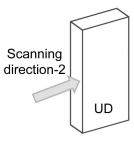	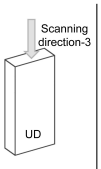	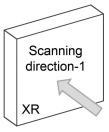	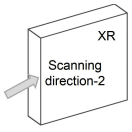	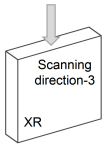
Avg speed from ultrasonic scans (m/s)	6160.9	6146.9	6332.3	6168.2	6225.2	6229.2
Avg speed from EBSD and simulations (m/s)	6171.3	6190.2	6358.8	6175.2	6233.2	6232.8
Error (%)	0.17	0.70	0.42	0.11	0.13	0.05

The spatial ultrasonic wave velocities calculated for a given surface are then averaged in order to get the average speed on that surface. The computed results along with the experimental ultrasonic velocity measurements are listed together for comparison in Table 2.5. It can be seen that the results obtained show good quantitative agreement and support the validity of the modelling approach for determination of texture effects in ultrasonic velocity.

SECTION. 2.4

Discussions

Existing techniques for texture detection and quantification in polycrystal materials, such as X-ray Diffraction and EBSD, are currently simply not appropriate for bulk testing and perhaps never will be. Ultrasonic techniques, having undergone major advancements in recent years with particular emphasis on array imaging hardware and processing systems and detailed study of the scattering and beam deviation of waves by inhomogeneities, hold out the very attractive potential for achieving the goal of non-destructive bulk texture detection, subject to a range of problems being overcome.

In the context of HCP alloys, at least for single phase, the ultrasonic speeds have been proved to be bounded by the elastic anisotropy of the crystal but the differences are sufficiently large such that ultrasonic measurement should be possible in textured materials. Just as defects, textures in polycrystals are also three-dimensional – as are macro-zones, and in this chapter focusses have been paid on the measurement of tri-directional wave speed. However, there is much scope for multi-directional and multi-transducer (array) techniques which could potentially overcome many of the problems and enable, for example, the orientation-dependence of texture to be determined, along with the spatial variation of texture. The same arguments apply for macro-zones, and the preliminary analyses presented in this chapter support this.

However, the determination of texture from velocity measurements is a classical inverse problem for which a straightforward solution is hard to obtain. In addition, the analyses of arbitrary textures in Zr raise the important issue of non-uniqueness and the difficulties associated with differentiating between differing textures but which may produce the same ultrasound signature. These issues will be addressed partly (for HCP materials) in the next chapter, where a solution to the inverse problem is

provided, with the uniqueness of the problem proved and the methodology to obtain texture from ultrasonic wave velocities presented.

SECTION. 2.5

Conclusions

In this chapter, a polycrystal representative volume element methodology has been developed for an aggregate of elastically anisotropic HCP-BCC two-phase model polycrystals in which crystallographic orientations may be specified in order to be representative of random or specifically defined textures. The ultrasonic response of the model has been validated for the transmission and reflection of a Hanning window against Christoffel equation for homogeneous elastic anisotropy.

The polycrystal RVE model has been employed to investigate the ultrasonic response of a range of computationally-generated random texture realizations in order to identify bounds on the ultrasonic wave speed for such textures in comparison to the upper and lower wave speed bounds set by the extremes of elastic anisotropy of HCP crystals. Randomly textured Zr polycrystals were found to generate wave speeds of about 5615 m/s within a range of approximately ± 25 m/s, relative to the anisotropic single-crystal bounds of 5480 and 6000 m/s. A range of textured Zr polycrystals were found to demonstrate easily measurable differences in ultrasonic velocity. In addition, the incorporation of a macro-zone typical of that occurring in titanium alloys in service has been analysed over a range of crystallographic orientation relative to wave direction.

Two Ti-6Al-4V samples with differing rolling histories have been characterized using EBSD and examined with the ultrasonic scanning method to determine wave speed in three orthogonal directions for each sample. The alpha-beta textures have been quantified and incorporated within the polycrystal model in order to predict the ultrasonic wave speeds in the three orthogonal directions for each sample. The computed and experimental ultrasound speeds were in good quantitative agreements (with errors less than 1%) and both the experimental measurements and model predictions

indicate the existence of clear velocity profiles enabling random, uni-directionally and cross-rolled Ti textures to be differentiated using ultrasound. These results suggest the potential for the development of diagnostic ultrasound techniques for bulk 3D hexagonal textures.

3

The Inverse Studies I: Spherical Convolution Theorem and The Solution to HCP Textures

In the previous chapter, forward studies have been presented for HCP titanium and zirconium alloys using both computational and experimental methods and found a strong relationship between texture and polycrystal wave velocity, which supported the possibility to capture texture differences by means of ultrasonic wave speed measurements. The possibility was strengthened by Moreau et al [87], who found good agreement between surface ultrasonic and EBSD texture measurements for a titanium sample with macrozones.

In this chapter, a rigorous mathematical description is presented to establish the relationship between HCP polycrystal bulk wave velocity and texture, whose form after performing spherical harmonic expansion can be used to carry out both forward and inverse studies instantly with satisfactory accuracy. This chapter is organized so that firstly, the theoretical background to single HCP crystal wave velocity is briefly presented, which is followed by the theoretical framework, the heart of the studies conducted in this chapter, including the refined analytical equation improved from the classic grain average method, its anatomy by means of spherical harmonics and eventually the spherical convolution theorem. The theorem is assessed firstly in forward studies in which experimental textures are employed in order to determine,

using the methodology presented, the corresponding ultrasonic wave speeds. The speeds so predicted are compared with the wave speeds independently determined using dynamic elastic polycrystal finite element techniques. Finally, the methodology is employed for inverse studies, where the currrent work is of most significance, in which three-dimensional textures, characterised with predicted ODFs, are uniquely determined from knowledge of ultrasonic wave speed distributions and single crystal elasticity properties. The predicted ODFs, shown through pole figures, are compared with the originals used in order to generate the representative ultrasonic wave speed distributions.

SECTION. 3.1

Background: Orientation Distributions, Pole figures and Single Crystal Wave Velocities for HCP Materials

3.1.1 HCP c-axis pole distributions

It has been discussed in detail in the previous chapter that HCP crystals are often simplified to be elastically transversely isotropic, in that they are assumed to be isotropic on the basal plane about the c-axis while having different (normally larger) modulus along the c-axis. Hence ultrasonic wave velocity in an HCP crystal depends only on the angle between the wave propagation direction and the c-axis, such that the retrievable information from ultrasonic measurements is potentially the orientation of the c-axis, or the orientation distribution of the c-axes if a polycrystal is considered.

The orientation of the c-axis of an HCP crystal in the polycrystalline sample coordinate system o-xyz can be specified by the combination of a polar angle θ and an azimuthal angle ϕ, as shown in Figure 3.1. Therefore, statistical pole distribution of the c-axes of all crystals in the sample can be described by a probability function $q(\theta, \phi)$ which satisfies:

$$\int_0^{2\pi} \int_0^{\pi} q(\theta, \phi) \sin\theta d\theta d\phi = 1 \tag{3.1}$$

This definition is similar to the plane-normal distribution obtained in diffracted X-ray measurements defined by Roe [39], and the visualization of this function $q(\theta, \phi)$ (with some changes to the normalization method) is a (0001) pole figure of the polycrystal. The main aim of this chapter is to present a methodology for the determination of the c-axes distribution function $q(\theta, \phi)$ of the HCP polycrystal, as well as its pole figures, from ultrasonic wave measurements.

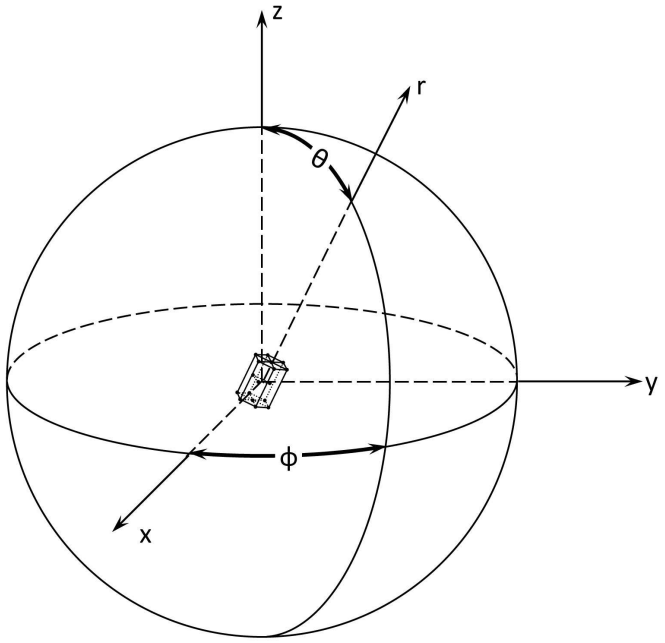

Figure 3.1: The orientation of an HCP crystal described by two angles

3.1.2 Single crystal wave velocities

In order to study ultrasonic wave velocity in an HCP crystal, the elastic properties are required. For instance, as listed in Chapter 1, an alpha-phase Ti-6Al-4V single crystal has the following stiffness matrix (unit:GPa) at the room temperature when its c-axis lies along the z axis in an orthogonal coordinate system [90]:

$$\mathbf{C} = \begin{pmatrix} 170.0 & 92.0 & 70.0 & & & \\ 92.0 & 170.0 & 70.0 & & & \\ 70.0 & 70.0 & 192.0 & & & \\ & & & 39.0 & & \\ & & & & 52.0 & \\ & & & & & 52.0 \end{pmatrix} \tag{3.2}$$

With knowledge of C_{ijkl}, the ultrasonic wave phase velocity in any given direction $\mathbf{n} = (\ n_1 \quad n_2 \quad n_3\ )^{\mathbf{T}}$ in three-dimensional space can be obtained by solving the Christoffel equation by substituting equations 3.2 and $\mathbf{n}$ into those given in Section 2.1. It should be noted again that our interest here is in the fastest wave, being the compression (longitudinal) wave.

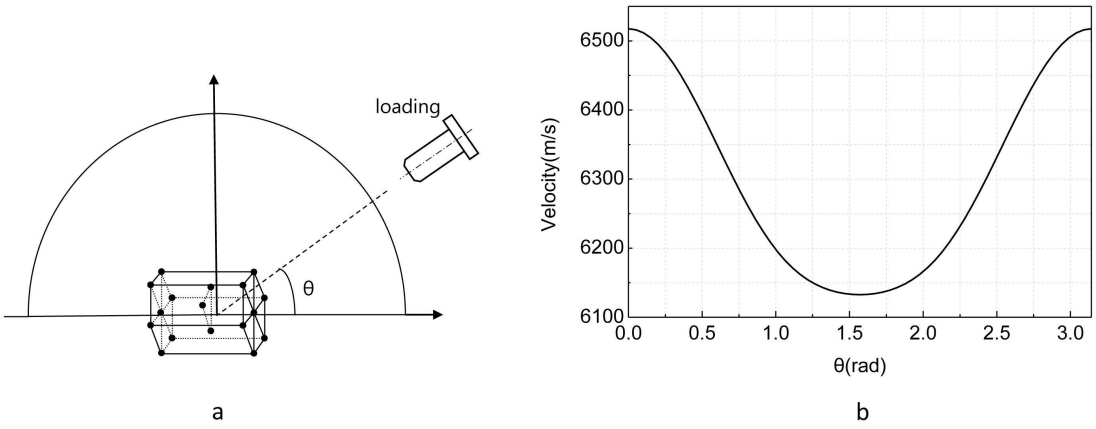

Figure 3.2: a. An HCP crystal in the reference configuration, and the incident angle θ between the wave direction and the reference direction; b. the compression wave velocity with θ

Because the crystal is taken to be isotropic about its c-axis, which is aligned along the z-axis, the velocity on the y-z plane is representative of velocities in all directions. The relationship between θ, which is the incident wave angle defined in Figure 3.2a, and the resulting wave velocity for this particular configuration has been illustrated in Figure 2.1 and is now shown in a different way in Figure 3.2b. It is still clear that the highest velocity occurs when the wave propagates along the c-axis where $\theta = 0$, and the lowest velocity when the incident wave and crystal c-axis are normal to each other when $\theta = \pi/2$. The response is a periodic function with period of π (not 2π because of the centrosymmetry of ultrasonic tests), and here only a single period, from 0 to π, is shown.

Next, a crystal which is rotated with an offset angle φ from the previous configuration

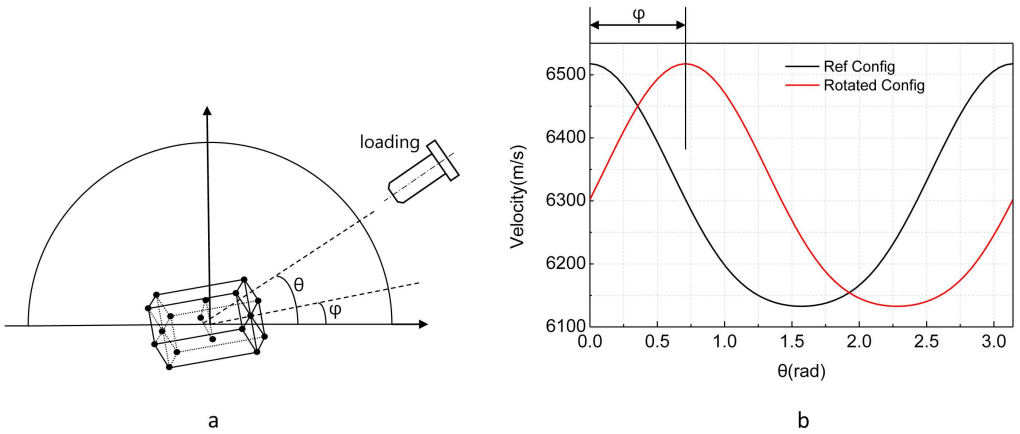

Figure 3.3: a. An HCP crystal configured with an offset φ and the wave incident angle θ; b. the resulting phase shift caused by φ to wave velocity with θ

is shown in Figure 3.3a. The offset introduces only a phase shift with magnitude φ so that if the wave velocity response in a single crystal in the reference configuration is $f(\theta)$, then the response of a crystal with orientation φ should be $f(\theta - \varphi)$, which is shown in Figure 3.3b, against that for the reference configuration.

SECTION. 3.2

Theoretical Framework for Studies on HCP

This section is devoted to the deduction of the theoretical framework for the studies on HCP. An analytical model is first established based on the classical grain average method, followed by its analyses by means of spherical harmonic expansions which lead to heart of this chapter, the spherical convolution theorem; and then discussions of the theorem are presented.

3.2.1 Refinement of grain average model

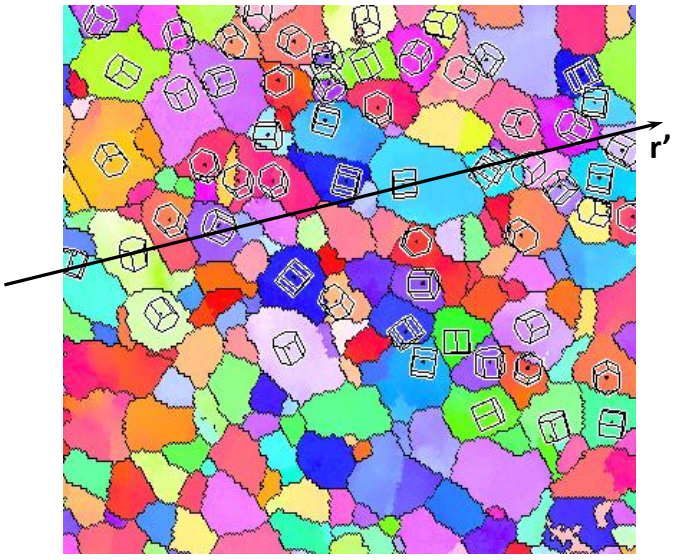

Figure 3.4: An ultrasonic wave beam propagating through an array of HCP crystals, as an approximation of the real case.

The idea of grain averaging is employed initially to develop the relationships between single crystal orientation, polycrystal texture and polycrystal wave velocity. When excited into an HCP polycrystal from a point source with large enough wavelength (greater than twice of grainsize), an ultrasonic wave can be assumed to see the polycrystalline aggregate as a continuum and the the grain sizes do not affect the overall wave speed, and its wavefront propagates out approximately in the shape a sphere;

if the wave propagation in a specific direction only is of interest, the problem can be simplified to one dimension in which a wave propagates in a straight line through an array of crystals, as shown in Figure 3.4. Assume that along this particular direction, the volume fraction of crystals with an orientation φ_i with respect to the direction is described by $g(\varphi_i)$, then the overall velocity in this direction can be calculated by averaging the contribution from grains with differing orientations by:

$$v = \sum f(\varphi_i)g(\varphi_i) \tag{3.3}$$

where $f(\varphi_i)$ represents the wave velocity through a single crystal with orientation φ_i in the specified direction.

Now as a first-step simplification for subsequent deductions, consider the two-dimensional case of an aggregate of a large number of HCP crystals with the c-axis of each crystal lying on the same plane, and the aggregate being statistically homogeneous in such a way that when evaluated from any angle within that plane, the waves go through the same texture. If θ is defined as the wave incident angle shown in Figure 3.3a, then the wave velocity in a crystal with orientation φ is $f(\theta - \varphi)$. With $g(\varphi)$ the volume fraction of crystals with orientation φ, the relationship between wave velocity with given direction θ for this two-dimensional case is given by:

$$v(\theta) = \sum f(\theta - \varphi_i)g(\varphi_i). \tag{3.4}$$

In polycrystals, crystallographic orientation need not, in fact, remain uniform within a given crystal, or grain. Variations in orientation result from the previous deformation history. Hence, rather than consider a grain-averaged approach, the possibility that orientation varies continuously is allowed such that the summation in equation 3.4

becomes:

$$v(\theta) = \int_0^{\pi} f(\theta - \varphi) g(\varphi) d\varphi \tag{3.5}$$

which is the standard definition of a convolution. It implies that the wave velocity through a two-dimensional aggregate of HCP crystals, where all crystal c-axes remain in-plane, is the convolution between single crystal velocity and the in-plane orientation distribution of crystal point-wise c-axes.

In order to generalise into three-dimensional space, two unit direction vectors are introduced such that $\boldsymbol{r_1}$ represents the wave propagation direction, and $\boldsymbol{r_2}$ the crystal c-axis orientation. Statistical homogeneity remains assumed such that when evaluating the polycrystal from any direction in the space, the ultrasonic waves are assumed to propagate through the same texture.

A similar integration process as above is adopted with some modification. At a given point in a crystal, the wave velocity depends only on the angle between its propagation direction and the c-axis of the crystal. The wave velocity in direction $\boldsymbol{r_1}$ through a crystal with orientation $\boldsymbol{r_2}$ is therefore expressed as $f\big(\arccos(\boldsymbol{r_1} \cdot \boldsymbol{r_2})\big)$. By definition, $\boldsymbol{r_1}$ and $\boldsymbol{r_2}$ in three dimensions, considering a point wave source, generate the surface of a unit sphere, so the integration required from equation 3.5 is written as:

$$v(\boldsymbol{r_1}) = \int_{\Omega} f(\arccos(\boldsymbol{r_1} \cdot \boldsymbol{r_2})) g(\boldsymbol{r_2}) d\Omega. \tag{3.6}$$

Note that $\int_\Omega$ indicates that the integration is carried out over the whole surface of the unit sphere that $\boldsymbol{r_2}$ covers.

Up to now, the function g has been defined as a volume fraction of crystallographic orientation. However, discretising the units to infinitesimal in the required summation transforms the summation into an integration, and the introduction of $\boldsymbol{r_2}$ in equation 3.6 leads the function g to the same concept as the orientation distribution function $q(\theta, \phi)$ defined in equation 3.1. If q is used instead of g to denote the orien-

tation distribution, and define a new function k which satisfies $k(\cos(\theta)) = f(\theta)$ to describe the single crystal velocity profile, equation 3.6 can be re-written as:

$$v(\boldsymbol{r_1}) = \int_{\Omega} k(\boldsymbol{r_1} \cdot \boldsymbol{r_2}) q(\boldsymbol{r_2}) d\Omega \tag{3.7}$$

This expression looks similar to that for classical grain averaging, but the introduction of the two direction vectors for wave direction and crystallographic orientation makes it fundamentally different. In fact, equation 3.7 is a spherical convolution, and by introducing spherical harmonics, it allows us to perform both forward and inverse studies in relating texture to ultrasonic wave speed.

3.2.2 Spherical Convolution Theorem

It transpires that many similarities exist between equation 3.7 and the formulation of a classical problem in computer graphics called radiance and irradiance. In the latter problem, researchers project surrounding light sources onto the reflective surface of a sphere to render a reflection image (or an environment map); or vice versa, try to recover the surrounding light sources from the environment map. An excellent analysis of this problem is presented by Ramamoorthi et al [91, 92], and in the following, I adapt from their approach in order to establish the spherical harmonic theorem for my own study.

- **Vectors to scalars in the analytical model**

For the purpose of convenience, equation 3.7 needs to be transformed from vector to its corresponding scalar form. A given crystallographic orientation direction of $\boldsymbol{r_2}$ on the right-hand side of equation 3.7 provides a rotated local coordinate system o-$x'y'z'$ with respect to which the ultrasonic wave incident direction $\boldsymbol{r_1}$ may be evaluated to give the single crystal velocity $k(\boldsymbol{r_1} \cdot \boldsymbol{r_2})$ in the $\boldsymbol{r_1}$ direction. The rotation of the

coordinate system may be described using three Euler angles α, β, γ about the Z-Y'-Z'' axes respectively according to Roe's convention [39], as shown in Figure 3.5. However, the third Euler angle does not have physical significance here because the single crystal elastic properties are assumed to be isotropic about the Z'' axis, and the anisotropy is completely determined by the first two angles. However, for the purposes of completeness, the third rotation angle γ is retained, and the physical non-significance of γ is addressed later. Now that the ultrasonic wave velocity $v(\boldsymbol{r_1})$ is dependent on the three Euler angles, it can be re-written as $v(\alpha, \beta, \gamma)$.

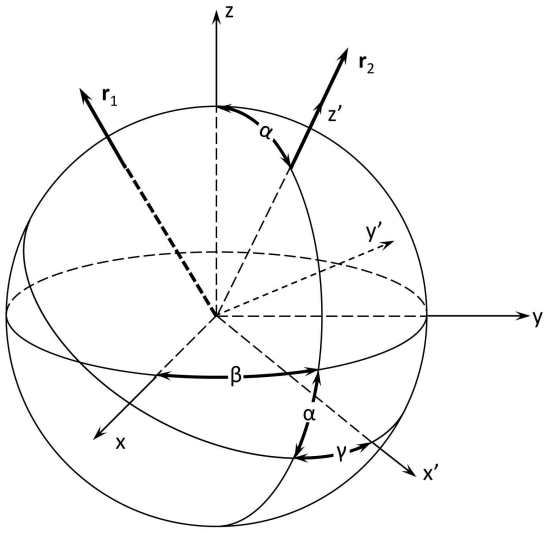

Figure 3.5: The global coordinate system o-xyz and a rotated local coordinate system o-$x'y'z'$ associated with the crystallographic orientation direction $\boldsymbol{r_2}$. The wave incident direction $\boldsymbol{r_1}$ is evaluated with respect to o-$x'y'z'$ to give $k(\boldsymbol{r_1} \cdot \boldsymbol{r_2})$.

The wave incident direction $\boldsymbol{r_1}$ can be described by the combination of a polar angle θ and an azimuthal angle ϕ in the global coordinate system, but the wave velocity depends only on the relative orientation of $\boldsymbol{r_1}$ with respect to $\boldsymbol{r_2}$. In other words, it is the set of polar and azimuthal angles θ' and ϕ' of $\boldsymbol{r_1}$ with respect to the rotated crystal coordinate system given by $\boldsymbol{r_2}$ that determine the wave velocity. Here (θ', ϕ') can be obtained by rotating the original pair (θ, ϕ) using the Euler angles for rotating the global coordinate system. Following the conventions in quantum mechanics, this

rotation can be written to the *active* form [40] as:

$$(\theta', \phi') = R^{(a)}(\alpha, \beta, \gamma) \cdot (\theta, \phi) = R_z^{(a)}(\beta) \cdot R_y^{(a)}(\alpha) \cdot R_z^{(a)}(\gamma) \cdot (\theta, \phi) \tag{3.8}$$

where R_z indicates a rotation about the z axis and similarly, R_y about y axis. The original vector form of equation 3.7 can now be transformed into the scalar form as follows:

$$\begin{aligned} v(\alpha, \beta, \gamma) &= \int_0^{2\pi} \int_0^{\pi} k(\theta', \phi') q(\theta, \phi) \sin(\theta) d\theta d\phi \\ &= \int_0^{2\pi} \int_0^{\pi} k\big(R^{(a)}(\alpha, \beta, \gamma) \cdot (\theta, \phi)\big) q(\theta, \phi) \sin(\theta) d\theta d\phi \end{aligned} \tag{3.9}$$

- **Spherical Harmonics and their rotations**

More subtle properties can be revealed from equation 3.9 by means of spherical harmonic expansion. Spherical harmonics, which are analogous on the sphere to a Fourier basis on a line or a circle, can be treated as a set of bases upon which any function defined on a sphere can be expanded into harmonic series (about which a short introductory description is given in Appendix A). The orthogonal spherical harmonic basis of degree l and order m ($-l \leq m \leq l$) is defined as

$$Y_{lm}(\theta, \phi) = P_{lm}(\cos\theta) e^{im\phi} \tag{3.10}$$

where $P_{lm}(\cos\theta)$ is the *normalized* associate Legendre polynomial which accounts for the effects of the polar angle θ; while $e^{im\phi}$ means that the dependence of azimuthal angle ϕ in spherical harmonics is described in terms of the Fourier bases. Note that the Condon-Shortley phase is not included in the spherical harmonics used in this thesis. The further deductions may be started by expanding $q(\theta, \phi)$ into spherical

harmonic (SH) series as similarly carried out by Roe [39]

$$q(\theta,\phi)=\sum_{l=0}^{+\infty}\sum_{m=-l}^{l}Q_{lm}Y_{lm}(\theta,\phi) \tag{3.11}$$

where Q_{lm} is the SH coefficient obtained by projecting the original function onto the spherical harmonic bases [93]

$$\begin{aligned} Q_{lm} &= \int_{\Omega} q(\theta,\phi)Y^{*}_{lm}(\theta,\phi)d\Omega \\ &= \int_{0}^{2\pi}\int_{0}^{\pi} q(\theta,\phi)Y^{*}_{lm}(\theta,\phi)\sin(\theta)d\theta d\phi \end{aligned} \tag{3.12}$$

Here Y^{*}_{lm} stands for the complex conjugate of Y_{lm}.

The expansion of the function k in equation 3.9, however, is more difficult because of the rotations involved. It is firstly expanded in terms of the local angles and SH bases associated with the rotated coordinate system:

$$k(\theta',\phi')=\sum_{n=0}^{+\infty}\sum_{h=-n}^{n}K_{nh}Y_{nh}(\theta',\phi') \tag{3.13}$$

It may be noted that since an HCP crystal is assumed to be elastically isotropic about its c-axis which, under current circumstances, is aligned along the z'-axis, k therefore has no dependence on ϕ'. This symmetry enforces its SH coefficients K_{nh} to be:

$$\begin{aligned} K_{nh} &= \int_{0}^{2\pi} k(\theta')P_{nh}(\cos\theta')\sin(\theta')d\theta' \int_{0}^{\pi} e^{-ih\phi'}d\phi' \\ &= \begin{cases} K_{n0}, & h=0 \\ 0, & h\neq 0 \end{cases} \end{aligned} \tag{3.14}$$

Substituting this relationship back to equation 3.13 gives:

$$k(\theta',\phi')=\sum_{n=0}^{+\infty}K_{n0}Y_{n0}(\theta',\phi') \tag{3.15}$$

By comparing equation 3.11 and 3.15, it can be seen that the former expansion is done with respect to global SH bases while the latter to the local crystal system. This difference in the bases is bridged by rotating the global SH bases into the positions of the local ones via the Wigner D-matrix $D^n(\alpha, \beta, \gamma)$ [94]:

$$Y_{n0}(\theta', \phi') = \sum_{m'=-n}^{n} D^{n*}_{m'0}(\alpha, \beta, \gamma) Y_{nm'}(\theta, \phi) \tag{3.16}$$

where $D^n_{m'0}(\alpha, \beta, \gamma)$ are elements of the Wigner-D matrix defined as

$$D^n_{m'0}(\alpha, \beta, \gamma) = e^{im'\beta} d^n_{m'0}(\alpha) e^{i0\gamma} = d^n_{m'0}(\alpha) e^{im'\beta}. \tag{3.17}$$

Ramamoorthi's notation [91] is followed here to denote D^n as a $(2n+1) \times (2n+1)$ matrix containing the information about how to describe the rotated SH bases as a linear combination of the original SH bases of the same degree, and $d^n_{m'0}(\alpha)$ in equation 3.17 are Wigner-d matrix elements directly related to the Jacobi polynomials. Note also that $d^l_{mn}(\alpha)$ follow similar concept with $Z_{lmn}(\cos\alpha)$ defined by Roe in [39], but is not normalized.

Equation 3.17 shows that the rotations of SH bases do not have any dependence on γ, which follows from the earlier statement about the physical (anisotropic) insignificance of γ. In addition, it can be shown [94] that

$$D^n_{m'0}(\alpha, \beta, \gamma) = \sqrt{\frac{4\pi}{2n+1}} Y_{nm'}(\alpha, \beta) \tag{3.18}$$

and this property will be utilized as a key point in the following.

- **The spherical convolution theorem**

Now all the necessary tools have been gathered to develop a closed form expression for the convolution relationship in equation 3.7. Substituting equations 3.11, 3.15

and 3.16 back into 3.9 leads to the following:

$$\begin{aligned} v(\alpha,\beta,\gamma) &= \int_0^{2\pi}\int_0^{\pi} k\big(R^{(\alpha)}(\alpha,\beta,\gamma)(\theta,\phi)\big)q(\theta,\phi)\sin(\theta)d\theta d\phi \\ &= \sum_{n=0}^{+\infty}\sum_{m'=-n}^{n} K_{n0}D^{n*}_{m'0}(\alpha,\beta,\gamma)\sum_{l=0}^{+\infty}\sum_{m=-l}^{l} Q_{lm}\cdot T_{n,m',l,m} \end{aligned} \tag{3.19}$$

where:

$$T_{n,m',l,m} = \int_0^{2\pi}\int_0^{\pi} Y_{nm'}(\theta,\phi)Y_{lm}(\theta,\phi)\sin(\theta)d\theta d\phi = \delta_{ln}\delta_{m\bar{m}'} \tag{3.20}$$

Because of the orthogonality of spherical harmonics, $T_{n,m',l,m}$ is equal to 1 if and only if $l = n$ and $m' = -m$, which reduces equation 3.19 into:

$$v(\alpha,\beta,\gamma) = \sum_{l=0}^{+\infty}\sum_{m=-l}^{l} K_{l0}Q_{lm}D^{l*}_{\bar{m}0}(\alpha,\beta,\gamma). \tag{3.21}$$

With a few changes of the symbols, equation 3.18 can be re-written as:

$$D^{l*}_{\bar{m}0}(\alpha,\beta,\gamma) = D^{l}_{m0}(\alpha,\beta,\gamma) = \sqrt{\frac{4\pi}{2l+1}}Y_{lm}(\alpha,\beta). \tag{3.22}$$

Substituting 3.22 back in to equation 3.19 and dropping the angle γ on the left side of the equation since wave velocity does not have any dependence on γ simplify the equation to:

$$v(\alpha,\beta) = \sum_{l=0}^{+\infty}\sum_{m=-l}^{l}\sqrt{\frac{4\pi}{2l+1}}K_{l0}Q_{lm}Y_{lm}(\alpha,\beta) \tag{3.23}$$

which means that if the velocity v is expanded into an SH series, its SH coefficients are given by:

$$V_{lm} = \sqrt{\frac{4\pi}{2l+1}}\cdot K_{l0}\cdot Q_{lm} \tag{3.24}$$

and equations 3.23 and 3.24 form the spherical convolution theorem for our analysis.

3.2.3 Discussion of the approach

The relationships between the functions v, k and q are revealed explicitly by the spherical harmonic theorem above, which, firstly, enables us to perform the forward problem where polycrystal wave velocities may be predicted with knowledge of texture; and also, more importantly, provides a solution for the long-standing inverse problem in which texture may be predicted from knowledge of polycrystal wave velocity. Because the single crystal velocities $k(\theta, \phi)$ and their SH coefficients K_{l0} are known, using the convolution theorem from the right side to the left (i.e., convolving the texture SH coefficients with those for the single crystal velocity) to give the polycrystal SH coefficients, and thereby determine polycrystal velocities in different directions, is to perform the forward study. However, if the theorem is used from the left side to the right, i.e., obtain the polycrystal velocities and expand them into SH coefficients, and then de-convolve the single crystal velocity coefficients from these coefficients to obtain the texture SH coefficients, then that is the inverse problem. The steps of both the forward and inverse studies are illustrated in Figure 3.6, and both studies are examined in the following sections.

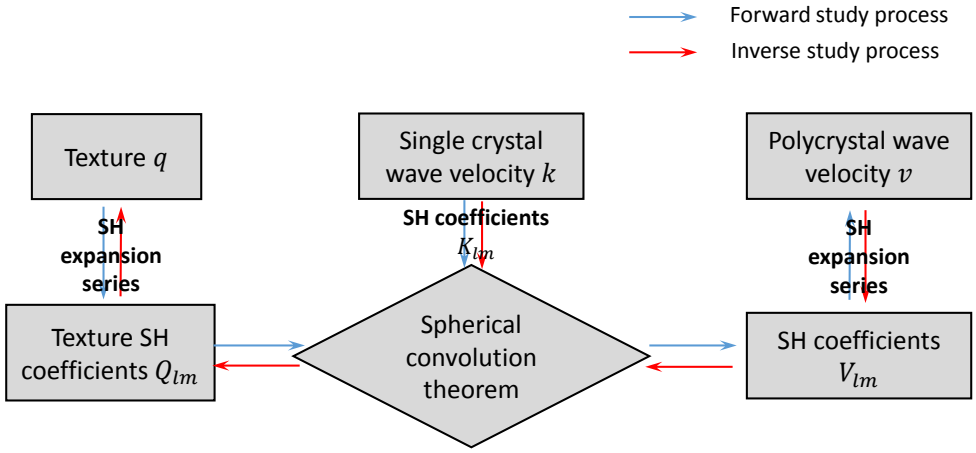

Figure 3.6: The flow chart of performing both forward and inverse studies using the spherical convolution theorem).

The SH coefficients of functions v, k and q are affected by certain symmetries. For

example, ultrasonic wave velocity tests always have centrosymmetry for both polycrystals and single crystals, which means, two waves propagating on the same line but in opposite directions have the same velocity; similarly, two crystals with exactly the opposite orientations are not distinguishable. This implies that the relationship

$$v(\theta, \phi) = v(\theta + \pi, \phi + \pi) \tag{3.25}$$

also holds for k and q. As proved by Roe [39], this symmetry enforces V_{lm}, K_{l0} and O_{lm} all equal to zero when l is odd.

It should also be noted that even though the single crystal velocities $k(\theta, \phi)$ have been used as the kernel of the convolution in equation 3.7, the model also has the flexibility to change the kernel for other single crystal physical properties that have similar directional variation relationship with k. For example, the wave slowness, which is defined as a vector along the direction of k with the amplitude of the reciprocal of k and is a crucial concept to Non-Destructive Evaluation (NDE) technology, can also be used as the kernel to calculate phase velocity variations in polycrystals. Similarly with slowness, if single crystal group velocity is used instead of phase velocity k, the outcome of the convolution becomes the variations of group velocity in the polycrystalline aggregate, which is experimentally more easily accessible for some detection techniques such as phased array. In addition, single crystal Young's modulus can also be used as the kernel to calculate the resultant Young's modulus variations in polycrystals.

SECTION. 3.3

Forward Studies: Predicting Ultrasonic Wave Velocities from Texture Using the Theorem

It has been shown in the previous section that with knowledge of c-axis pole distribution function $q(\theta, \phi)$, polycrystal wave velocity SH coefficients can be obtained using the spherical convolution theorem, such that with knowledge of polycrystal texture, wave velocity in any direction in the three-dimensional space can be predicted by constructing the polycrystal wave velocity function $v(\theta, \phi)$ using the ODF and single crystal wave velocity kernel, and their associated SH coefficients. In this section, an example of the forward problem is addressed in detail in which knowledge of polycrystal texture is utilized in order to predict resulting wave speed. I begin with some simple theoretical orientation distributions, and then move on to experimentally representative textures in HCP alloys. Following this, multiple examples of the inverse problem are addressed in detail in Section 3.5.

3.3.1 SH coefficients of single crystal velocities

The section is started by obtaining the SH coefficients of single crystal velocities. As mentioned in the previous section, the coefficients $K_{lm} = 0$ when $m \neq 0$ because the velocities do not depend on the azimuthal angle; moreover, $K_{l0} = 0$ when l is odd because of the centrosymmetry of the velocities. The corresponding spherical harmonics $Y_{l0}(\theta, \phi)$ for K_{l0} then simplify to $Y_{l0}(\theta, \phi) = P_{l0}(\cos\theta)$, which are *normalized* Legendre polynomials, so the even-degree SH coefficients of single crystal velocities can be obtained by fitting the curve shown in Figure 3.2b using Legendre polynomials with corresponding degrees. The resulting coefficients decrease with the degree l, and those of $0th$ to $8th$ degrees are listed in Table 3.1:

Table 3.1: SH coefficients of Ti-6Al-4V single crystal velocities

degree l	0	2	4	6	8
K_l^0	22088.30	374.61	58.96	-3.79	-0.29

3.3.2 Theoretical distributions

The spherical convolution theorem is next utilised for a number of theoretical pole distributions in order to obtain predicted velocity profiles. In the following parts, a single crystal in its reference orientation is firstly addressed, followed by a single crystal in a rotated orientation relative to the incident wave direction, and thirdly a polycrystal with random texture.

- **Single Crystal in reference configuration**

A single crystal clearly satisfies the homogeneity assumption of the analysis such that waves always go through the same texture. The (0001) pole distribution of a single crystal with its c-axis oriented in the (θ_0, ϕ_0) direction is a delta impulse at (θ_0, ϕ_0), hence the SH coefficients are calculated via:

$$Q_{lm} = \int_{\Omega} \delta(\theta_0, \phi_0) Y_{lm}^*(\theta, \phi) d\Omega = Y_{lm}^*(\theta_0, \phi_0) \tag{3.26}$$

If the single crystal is oriented with reference configuration, i.e., with its c-axis along the z-axis of the coordinate system, then both θ_0 and ϕ_0 are equal to 0. Hence from equation 3.26, the SH coefficients Q_{lm} may be obtained and convolved with the kernel coefficients shown in Table 3.1 using equation 3.24 to give the coefficients V_{lm}. Based on these SH coefficients, the original velocity, wave speed and orientation functions v, k and q may be computed in all directions with respect to the sample system. For the reference-configured single crystal case, all the *non-zero* SH coefficients of the

functions up to 8th degree, along with the spherical visualizations of the functions, are shown in Table 3.2.

Table 3.2: Results for single crystal with reference configuration

OD(q)	Kernel(k)	Velocity(v)
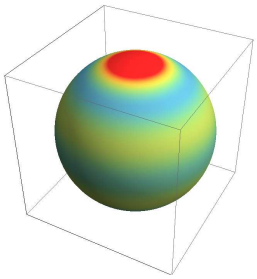	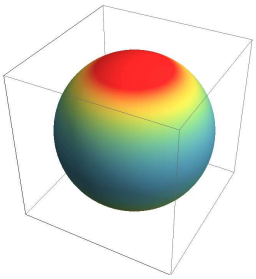	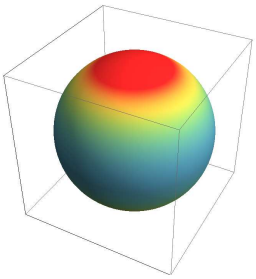
$Q_{00} = 1/2\sqrt{\pi}$	$K_{00} = 22088.3$	$V_{00} = 22088.3$
$Q_{20} = \sqrt{\frac{5}{4\pi}}$	$K_{20} = 374.61$	$V_{20} = 374.61$
$Q_{40} = \frac{3}{2\sqrt{\pi}}$	$K_{40} = 58.96$	$V_{40} = 58.96$
$Q_{60} = \sqrt{\frac{13}{4\pi}}$	$K_{60} = -3.79$	$V_{60} = -3.79$
$Q_{80} = \sqrt{\frac{17}{4\pi}}$	$K_{80} = -0.29$	$V_{80} = -0.29$

Figures in this and the following two tables for indicative purpose only.

Because the single crystal is oriented in exactly the same configuration with the kernel, the resulting velocity function v should be exactly the same as the kernel velocity function k, and correspond directly with the orientation function (here the single crystal orientation), and this is what is obtained in Table 3.2.

- **Single crystal with rotated orientation**

Next, consider a single crystal with an orientation rotated away from the reference configuration, say, with $\theta_0 = \pi/4$ and $\phi_0 = \pi/4$. The corresponding SH coefficients

are again obtained from equation 3.26, and the convolution is carried out as before. The resulting SH coefficients up to 4th degree and spherical visualizations are shown in Table 3.3.

Table 3.3: Results for single crystal with a rotated orientation

OD(q)	Kernel(k)	Velocity(v)
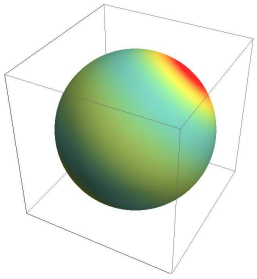	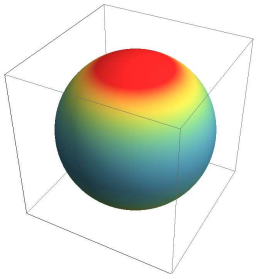	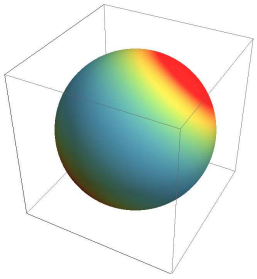
$Q_{00} = 1/2\sqrt{\pi}$	$K_{00} = 22088.3$	$V_{00} = 22088.3$
$Q_{20} = 0.1577$		$V_{20} = 93.65$
$Q_{21} = -0.2731 + 0.2731i$	$K_{20} = 374.61$	$V_{21} = -162.21 + 162.21i$
$Q_{22} = -0.1931i$		$V_{21} = -114.70i$
$Q_{40} = -0.3438$		$V_{40} = -23.95$
$Q_{41} = -0.0836 + 0.0836i$		$V_{41} = -5.83 + 5.83i$
$Q_{42} = -0.4182i$	$K_{40} = 58.96$	$V_{42} = -29.13i$
$Q_{43} = 0.2213 + 0.2213i$		$V_{43} = 15.42 + 15.42i$
$Q_{44} = -0.1106$		$V_{44} = -7.71$

Note that only Q_{lm} of order $m > 0$ are shown here, and that $Q_{l\bar{m}} = Q_{lm}^*$ ($\bar{m}$ means $-m$).

In this example, the resultant velocity function v is expected to maintain the velocity profile of the kernel k, but with the profile rotated in the same way as the orientation

distribution, q. It is shown in Table 3.3 that with the appropriate SH coefficients Q_{lm}, the velocity profile obtained after convolution is as expected.

In this example, it may be noted that the SH expansions (shown in Table 3.3 with up to 4th degree) for both the (0001) pole distributions and the velocity profile contain complex terms. The absence of the inclusion of the full complex form in the ODF distribution would preclude the accurate determination of the resulting velocity profile (as vice versa).

- **Random orientation**

Finally, in this example, the pole distribution function of a theoretically random texture is utilized with the single crystal velocity kernel to investigate the predicted resultant velocity profile. The orientation distribution function is a constant C over the entire surface of the unit sphere, and from equation 3.1 it is determined to be $C = 1/(4\pi)$, such that the SH coefficients are given by:

$$\begin{aligned} Q_{lm} &= \int_0^{2\pi} \int_0^{\pi} \frac{1}{4\pi} \cdot Y_{lm}^*(\theta, \phi) \sin(\theta) d\theta d\phi \\ &= \frac{1}{4\pi} \int_0^{\pi} P_{lm}(\cos\theta) \sin\theta d\theta \int_0^{2\pi} e^{-im\phi} d\phi \end{aligned} \tag{3.27}$$

which have non-zero values only if both l and m are 0. The convolution process is also performed as before giving the spherical visualization and SH coefficients shown in Table 3.4. It can be seen in Table 3.4 that as a result of the random texture, the polycrystal velocities are the same in all the directions, which means the random texture makes the polycrystal elastically isotropic. This property is represented mathematically with all the SH coefficients V_{lm} apart from V_{00} being equal to 0.

Table 3.4: Results for random orientation polycrystal

OD(q)	Kernel(k)	Velocity(v)
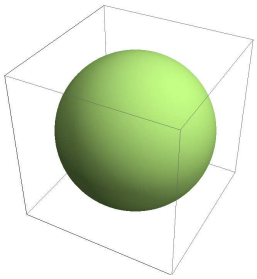	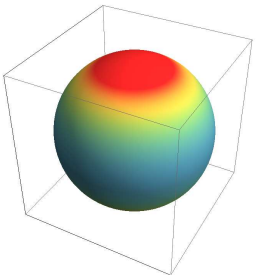	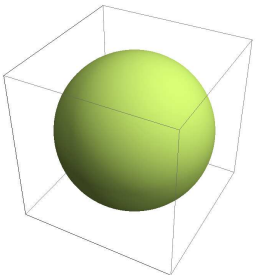
$Q_{00} = 1/2\sqrt{\pi}$	$K_{00} = 22088.3$	$V_{00} = 22088.3$
$Q_{2m} = 0$	$K_{20} = 374.61$	$V_{2m} = 0$
$Q_{4m} = 0$	$K_{40} = 58.96$	$V_{4m} = 0$
$Q_{6m} = 0$	$K_{60} = -3.79$	$V_{6m} = 0$
$Q_{8m} = 0$	$K_{80} = -0.29$	$V_{8m} = 0$

- **Constraints on higher order SH coefficients and truncation errors**

The calculation carried out so far for the simple theoretical distributions provide some insight into the nature of the methodology presented for evaluating HCP texture with ultrasonic waves. As listed in Table 3.1, the SH coefficients of the kernel are found to decrease with degree l, and the 6th and 8th degree coefficients K_6^0 and K_8^0 are -3.79 and -0.29, respectively. Given that the SH coefficients Q_{lm} are always less than or equal to those for the case of the single crystal with reference configuration, it can be shown that the corresponding SH velocity coefficients V_{6m} after convolution always have magnitude less than or equal to 3.79, and V_{8m} in particular is less than 0.29. A consequence of this is that when reconstructing the polycrystal velocities v from the SH coefficients, the impact of texture coefficients of 6th degree is no more than 3.79

m/s; for the 8th degree, no more than 0.29 m/s; and for higher degree, even less.

This leads to two important practical implications. First, when predicting polycrystal velocities using the spherical convolution model with knowledge of the texture SH coefficients, coefficients up to 6th degree are needed to achieve a theoretical velocity accuracy (as opposed to velocities measured experimentally) of approximately ± 1 m/s. Second and more importantly, when performing inverse studies (see later), since the best accuracy ultrasonic wave velocity tests can possibly achieve is normally worse than ± 3.79 m/s (typically ± 10 m/s), it becomes apparent that it is not possible to recover 6th or higher degree texture SH coefficients from ultrasonic wave velocity tests, because under these circumstances, numerical noise introduced is already much larger than the SH coefficient information to be extracted. This explains mathematically why it has been widely reported in the literature that only texture coefficients up to 4th degree are obtained [43, 70, 75, 76, 78]. Note that the SH coefficients arising in Tables 3.1 – 3.4 relate to HCP Ti-6Al-4V alpha phase, but that in general, the order of SH coefficients theoretically obtainable is determined by the spherical expansion of a given material's single crystal elastic properties.

Since the SH texture coefficients up to 4th degree are the practical goal, the issue of truncation error must be considered. Two extreme distributions, namely a single crystal and the theoretically random texture, should set the upper and lower bounds of the error respectively in any arbitrary case. A single crystal, whose distribution function is a delta impulse at a given orientation on the unit sphere and whose SH coefficients can be expanded to an infinite degree, leads to the largest truncation

error, whose standard deviation is calculated from [39] as:

$$\begin{aligned}\delta_q^2 &= \int_0^{2\pi}\int_0^{\pi}\Big(q(\theta,\phi) - \sum_{l=0}^{4}\sum_{m=-l}^{l} Q_{lm}Y_{lm}(\theta,\phi)\Big)\sin\theta d\theta d\phi \\ &= \int_0^{2\pi}\int_0^{\pi}\sum_{l=6}^{+\infty}\sum_{m=-l}^{l} Q_{lm}Y_{lm}(\theta,\phi)\sin\theta d\theta d\phi \\ &\approx \int_0^{2\pi}\int_0^{\pi}\sum_{l=6}^{N_0}\sum_{m=-l}^{l} Q_{lm}Y_{lm}(\theta,\phi)\sin\theta d\theta d\phi\end{aligned} \tag{3.28}$$

where N_0 is the order to numerically calculate the error. For EBSD tests N_0 is often chosen as 16, so compared to EBSD tests the standard deviation of the truncation $\delta_q^2 = 10.98$. Note though, that this is the extreme case of orientation distribution, and any real distribution will lead to far less error.

For the theoretically random texture, however, the orientation is uniform all over the sphere with only its 0th degree coefficient having a non-zero value, such that truncating the coefficients up to 4th degree does not cause any error at all. Hence, for any arbitrary texture, the standard deviation of the truncation error lies in the range of [0, 10.98], and the stronger the texture approaches a particular orientation, the larger the truncation error. Conversely, the closer the texture is to being random, the smaller the error. Awareness of the existence and origin of these errors may facilitate their diminution, but this has not been addressed in this thesis.

3.3.3 Studies with real example textures

- **Finite Element model and simulated wave velocities**

In this section, the RVE finite element model established in Chapter 2 is called upon in order to simulate the ultrasonic wave propagation in single-phased HCP polycrystals, taking full account of their crystallographic orientations, and hence texture, resulting from the elastic anisotropy. As shown by Figure 2.2 and demonstrated in Section

2.2, the model is able to accommodate 2160 crystals, with each being assigned an arbitrary orientation, such that a range of differing collective crystallographic textures could be studied, and in particular, the overall ultrasonic wave speeds for the differing textures could be determined. The ultrasonic wave signals were induced as pressure waves whose amplitudes are sinusoidal pulses in a Hanning window, and the centre frequency of the pulses is chosen to be 2MHz here, yielding the wavelength-to-crystal-size ratio at about 2.

It needs to be emphasized again that by employing transmission waves, whose speed is expected to be dominated by the overall crystallographic texture, the RVE model takes account of the collective effect of the overall texture only and discards the information of morphological texture, the arrangements of individual grains and grain boundaries. The relatively negligible effect of the discarded information has been proved via verification of the RVE model by the experimental studies combining conventional ultrasonic scans with EBSD tests presented in Chapter 2.

Comparative studies have been performed on nine differing experimentally representative HCP textures with Zr elastic properties and compared their resulting ultrasonic wave velocities. Here (0001) pole figures in Figure 2.17 are re-illustrated in Figure 3.7 with different colour-codings, and these textures are implemented into the RVE model again with the elastic properties of alpha phase Ti-6Al-4V. The resulting computed ultrasonic wave speeds determined for the respective textures are shown by the red dots in Figure 3.8 and are labelled as Simulation Results.

A clear dependence of the wave velocity on the polycrystal texture is again observed for the alpha phase Ti-6Al-4V, and the textures considered include those representative of a reasonably random polycrystal arrangement (eg Figure 3.7g) through to the likes of extremes for very highly textured arrangements (eg Figure 3.4i), with many intermediate and differing textures. In Figure 3.8, the wave speeds determined for the range of textures can also be seen to be bounded by the two extreme single

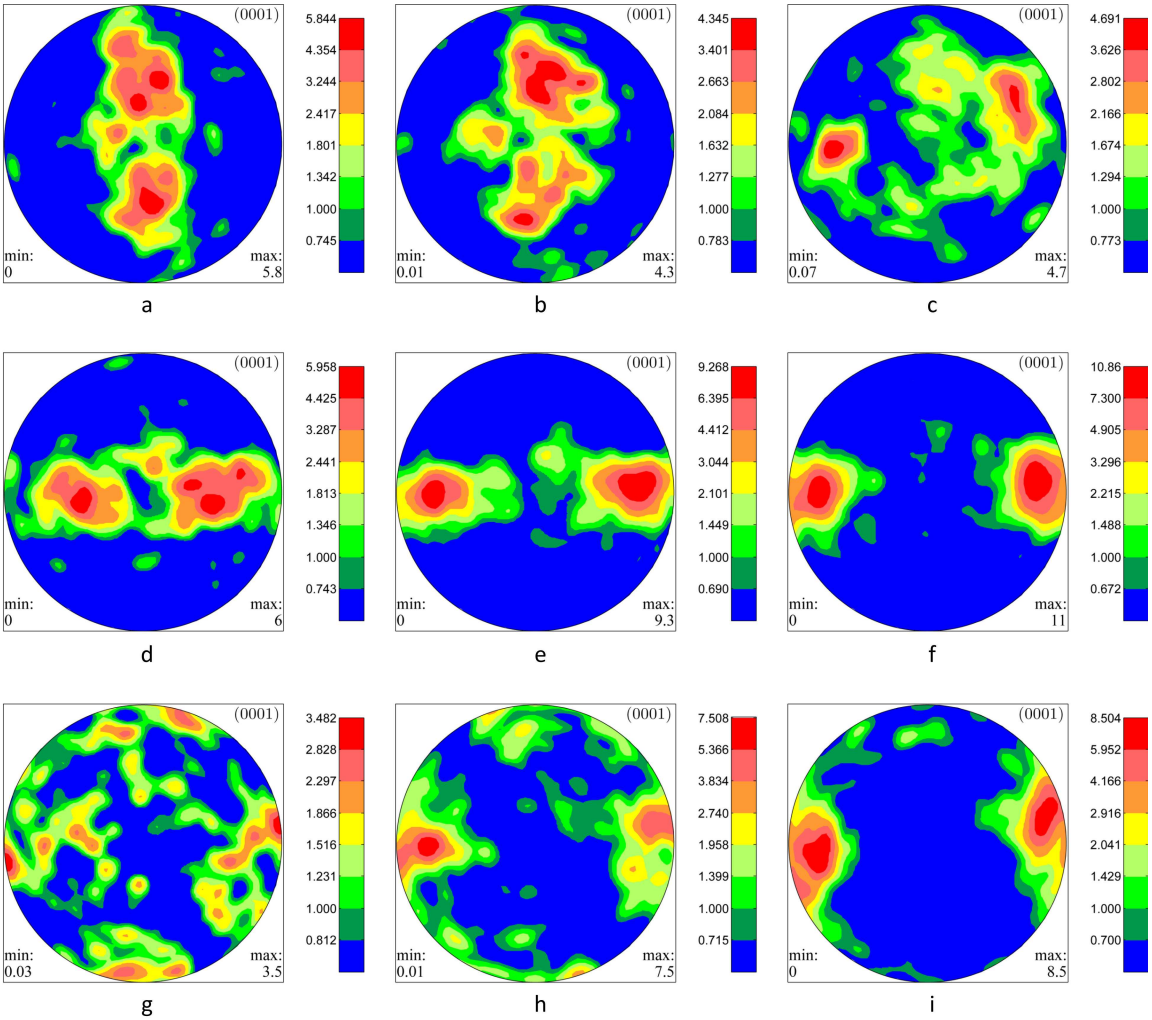

Figure 3.7: Nine differing experimentally representative pole figures (basically the same with Figure 2.17, but with colour-codings now changed).

crystal orientations (labelled SC and SC90 in the figure) resulting from configurations with the c-axis of the crystal parallel and perpendicular to incident wave direction, respectively. Included in the figure are also RVE-determined wave speed results for a range of realisations of computer-generated random polycrystals labelled Random zone in the figure, just as in Chapter 2 to indicate the range of wave speed expected for random textures. These independent calculations of wave speed for differing textures are used to compare with the predictions of the current convolution technique in the forward problem.

- **Convolution studies**

The section now proceeds to performing forward studies on the nine textures using the spherical convolution model. It is firstly necessary to calculate the SH texture coefficients Q_{lm} based on the known textures, for which the Matlab package MTEX [86] is a rather useful tool and is capable of readily outputting these coefficients from discrete orientation distribution inputs. Then, only a few pointwise multiplications are needed to be computed based on equation 3.24 to obtain the polycrystal SH wave velocity coefficients, so that the wave velocity function in three-dimensional space may be reconstructed and hence the wave velocity in any given direction in the space determined. Since in our independent RVE computational studies, only the wave speeds in one direction for each of the textures was examined - that is, along the z-axis in Figure 2.2c - I now try to obtain wave velocities from the convolution technique in the corresponding direction only by specifying both $\theta = 0$ and $\phi = 0$, in order to draw a straightforward comparison with the computational results from the FE model. The wave velocities so predicted by the convolution technique are also shown in Figure 3.8, labelled Velocity. Quantitative numerical comparisons are also listed in Table 3.6.

As discussed before, the convolution technique is enhanced by the flexibility to use other physical variables such as slowness as the kernel, and the way to do that is as follows: with phase velocity k calculated, it is easy to obtain the relationship of slowness changing with any given direction in the three-dimensional space, and its SH coefficients can be obtained by performing spherical harmonic expansion on the results, as listed in Table 3.5. Note that only the coefficients up to 6th degree are listed since they are the only ones needed to achieve a desirable accuracy, as explained in Section 3.2.3.

After the polycrystal slowness function s is obtained from using single crystal slowness

Table 3.5: SH coefficients slowness of the single crystal of Ti-6Al-4V

degree l	0	2	4	6
Slowness($\times 10^{-6}$)	160.5	-6.046	-1.177	0.1376

as the kernel and convolving with the c-axis distribution, the wave velocity $v(\theta, \phi)$ can then be calculated by:

$$v(\theta, \phi) = \frac{1}{s(\theta, \phi)}. \tag{3.29}$$

The wave velocities so determined are also shown in Figure 3.8 and Table 3.6 in order to investigate any resulting differences in the context of the textures considered. In addition, for the purpose of demonstrating the comparisons of the convolution technique with the Voigt and Reuss methods, the velocities obtained by respectively averaging stiffness and compliance tensors are also obtained with the help of MTEX [95] and shown in Figure 3.8 and Table 3.6.

Table 3.6: Comparisons of wave velocities obtained through various methods; row 2 shows simulated results, and rows 3 to 6 are obtained from the convolution method with different kernels (unit: m/s)

Texture	i	h	f	g	e	c	b	d	a
Voigt	6174.6	6191.9	6194.8	6213.0	6234.5	6241.2	6282.6	6287.0	6298.6
RVE FE	6147.1	6164.8	6176.0	6190.0	6221.3	6222.1	6272.4	6273.1	6283.0
Velocity	6172.6	6190.6	6193.6	6212.5	6235.2	6242.3	6282.7	6286.9	6298.4
Slowness	6172.8	6190.6	6193.4	6212.4	6234.9	6241.9	6282.6	6286.9	6298.4
Reuss	6145.4	6158.7	6174.0	6178.0	6208.3	6209.1	6253.3	6255.8	6269.0

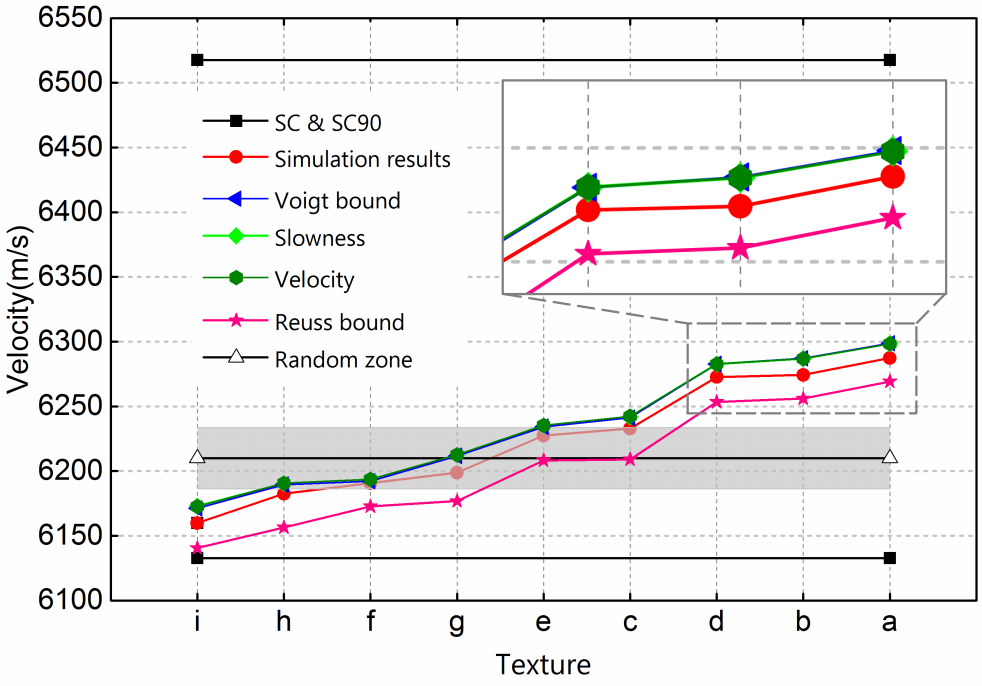

Figure 3.8: Comparisons between RVE FE and convolution technique wave velocities for the nine textures in Figure 3.7, with a zoomed-in view at the place marked by the dashed box (n.b.: the grey zone shows the velocity region for random textures, and all velocities in this figure are for waves of 3 MHz frequency, so the symbols on SC, SC-90 and Random lines do not mean simulations performed at the dot positions but are for differentiating purpose only).

- **Summary & Discussions**

Figure 3.8 shows that the wave velocities predicted by the Voigt and Reuss methods respectively have the largest and smallest magnitudes for a given texture, and the speeds calculated both via the RVE model and by using convolution kernels lie between them, which verifies Hill's conclusion that the Voigt and Reuss methods set up the upper and lower bounds for the polycrystal elastic stiffnesses. The predictions made by using wave velocity and slowness as kernel in the convolution technique are very close, and both kernels capture the changing relationship between polycrystal wave velocity and texture very well. The progressive wave velocity increases with texture sequence predicted by the RVE simulation is also very well captured by all

the convolution techniques.

It is notable in Figure 3.8 that the convolution technique, regardless of the kernel used, leads to predicted velocities which are consistently higher than those obtained from the RVE FE simulations and are almost overlapping with the those of Vogit's method. The difference in velocity is typically in the range of $5 \sim 15$ m/s. An explanation for this follows from the establishment of the convolution model: it is assumed that the wave propagates as a ray going through a sequence of crystals, without taking any account of the interaction among neighbouring grains. In the RVE FE model, the wave front propagates through the polycrystal, where the crystallographic orientations and resulting elastic anisotropy cause some crystals to result in higher velocity and some lower, along the wave front. This causes local stress fields to form, which, influence the average wave speed. Equivalently, because of the crystal anisotropy and the interactions among neighbouring crystals, the individual crystals do not necessarily behave as unstressed single crystals but in fact exhibit subtle differences of elastic properties as a result of the constraint imposed by the continuum requirements of equilibrium and compatibility which are not enforced in the convolution methodology. However, in summary, the convolution technique provides great sensitivity of wave speed to crystallographic texture both qualitatively and quantitatively.

SECTION. 3.4

Inverse studies: Crystallographic Texture from Wave Speeds

A number of forward studies on various theoretical and experimental orientation distributions have been successfully carried out in the previous section through the spherical convolution theorem model. In this section, the spherical convolution model is employed to tackle the long-standing inverse problem; that is, to retrieve polycrystal orientation distribution information from knowledge of spatial ultrasonic wave velocity.

3.4.1 Discretisation of the problem

For inverse studies of HCP polycrystals, the ultimate objective is the determination of the orientation distribution function of the HCP c-axes, to be reconstructed from its SH coefficients according to the SH expansion theory. The SH texture coefficients may be obtained by de-convolving the single crystal wave velocity from the polycrystal velocity function. Therefore, the first step in extracting the texture information from ultrasonic wave speed tests is to establish the polycrystal SH velocity coefficients V_{lm} from experimental results. It is hoped that in this chapter a proof of principle can be established so that rather than use experimentally measured velocity profiles with which to establish the SH velocity coefficients, I utilize the computational velocity results obtained from the RVE FE model used for forward studies above. The inverse studies, ie the de-convolution process, is then carried out according to the theorem, from these computational velocity measurements, in order to re-establish the orientation distributions from which they were determined. Hence, I aim to predict from the 'measured' velocity profiles the orientation distribution (0001) pole figures shown in Figure 3.7.

The SH velocity coefficients V_{lm} are obtained from wave velocity profiles $v(\theta, \phi)$ by projecting v onto the SH basis with degree l and order m which involves the continuous integration over the surface of the unit sphere as follows:

$$V_{lm} = \int_0^{2\pi} \int_0^{\pi} v(\theta, \phi) Y_{lm}^*(\theta, \phi) \sin(\theta) d\theta d\phi \tag{3.30}$$

In practice, however, it is not normally possible to obtain spatially continuous experimental data to perform this *continuous* integration, and often the best that can be obtained from experiment is a limited set of discrete wave velocity measurements over a given range of incident wave angles on the free surfaces of a typical polycrystal sample, or, in this chapter's case, a series of computational velocities in the range of incident angles. Hence it is often desirable to obtain the SH velocity coefficients from such limited number of discrete test results, which may be carried out by means of numerical integration techniques. The general approach for the numerical integration is firstly to discretise the continuous velocity function into a function at a number of nodes and then use the summation of the *weighted* function values at such nodes to approximate the continuous integration. As a result of this approximation, the numerical integration technique is only able to achieve accurate quantitative results for coefficients V_{lm} with degree $l \leq l_0$, hence the spherical harmonic expansion of the original velocity function v becomes band-limited to $l \leq l_0$ when being reconstructed [96, 97]:

$$v(\theta, \phi) = \sum_{l=0}^{l_0} \sum_{m=-l}^{l} V_{lm} Y_{lm}(\theta, \phi) \tag{3.31}$$

The degree l_0 achievable depends not only on the number of discrete nodes used, but also on the discretization scheme (i.e. the positions of the nodes) chosen and the nodal weighting functions used. The latter two are often referred to as the *quadrature* for the numerical integration, and the most widely used methods are equiangular and Gaussian-Legendre quadratures.

It was shown by Driscoll and Healy [96] that for a $2N \times 2N$ number of discrete data $f(\theta_i, \phi_j)$ at the equiangular grids $\theta_i = \pi i/(2N)$ and $\phi_j = \pi j/N$, where $i, j = 0, 1, 2, ..., 2N-1$, accuracy degree up to $2N-1$ for the objective SH coefficients can be achieved by performing the numerical integration using the following equation:

$$V_{lm} = \frac{\sqrt{2\pi}}{2N} \sum_{i=0}^{2N-1} \sum_{j=0}^{2N-1} v(\theta_i, \phi_j) Y_{lm}^*(\theta_i, \phi_j) \omega_N(i) \tag{3.32}$$

where $\omega_N(i)$ is the weight function for the ith node of the polar angle calculated by:

$$\omega_N(i) = \frac{\sqrt{2}}{N} \sin(\frac{\pi i}{2N}) \sum_{k=0}^{N-1} \frac{1}{2k+1} \sin\big[\frac{(2k+1)\pi i}{2N}\big] \tag{3.33}$$

It should also be noted that the number N in equations 3.32 and 3.33 is restricted to be a power of 2.

the number of discrete data needed is rather large. Taking our problem for example, the desired degree of precision for V_{lm} is 4, which means the degrees of both $v(\theta, \phi)$ and $Y_{lm}^*(\theta, \phi)$ need to be at least 4, so $2N-1$ must be no less than $2 \times 4 = 8$; and because N has to be a power of 2, the smallest N satisfying these requirements is 8, which means we need 16×16 discrete data to ensure the accuracy.

The Gaussian-Lengendre quadrature, on the other hand, is well known for its ability to get up to $(2N-1)$th degree of accuracy with $2N \times N$ discrete data [97, 98]. The numerical integration is written:

$$V_{lm} = \frac{\pi}{N} \sum_{j=0}^{2N-1} \sum_{i=0}^{N-1} v(\theta_i, \phi_j) Y_{lm}^*(\theta_i, \phi_j) \omega_N(i) \tag{3.34}$$

where $\omega_N(i)$ is the well-known weight function for the ith Gaussian node.

For our problem, since the 4th degree of accuracy is desired, theoretically only 10×5 discrete data are needed, which is much reduced compared to the equiangular

quadrature method. Hence, in the following studies, Gaussian-Legendre quadrature is used with $N = 6$ to achieve both accuracy and efficiency.

3.4.2 Obtaining polycrystal velocities using the RVE model

With the numerical integration method chosen, the next task is to obtain the ultrasonic wave velocities $v(\theta, \phi)$ varying with angles θ and ϕ, which would, in practice, be generated by exciting and detecting ultrasonic waves in different directions through a polycrystal sample of interest which satisfies the underlying assumption of homogeneity; but in this study, these velocities are generated using the computational RVE FE model introduced in Chapter 2 and used in the previous section. The polycrystal representation is shown in Figure 2.2a, and wave velocity measurements need to be obtained over a range of incident wave angles.

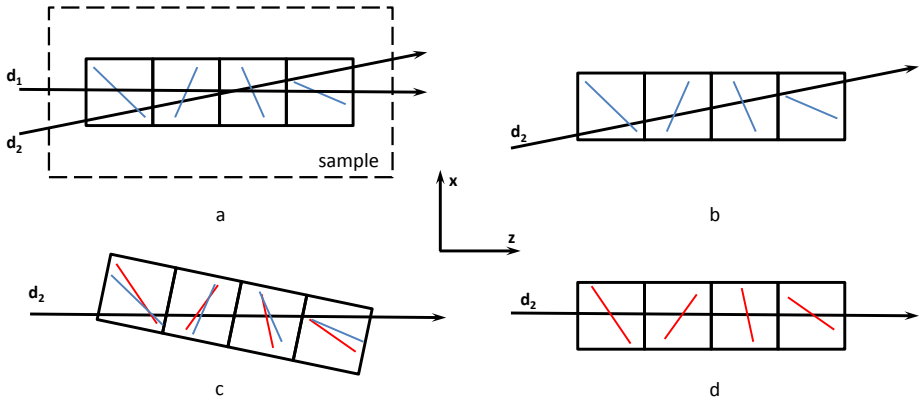

Figure 3.9: a. The actual testing scheme where the sample remains still and the evaluation direction varies; b. The relative orientations of the crystals to d_2 and the global system; c. The change of crystal orientations with respect to the global system after rotating the whole model to the configuration such that d_2 is along the z-axis; d. The retention of the crystallographic orientations and discarding of the morphology.

The principle of achieving the varying evaluation directions in the RVE model is illustrated in Figure 3.9. The actual testing scheme is sketched in Figure 3.9a, where d_1 is along the global z-axis and d_2 along an arbitrary direction, and the blue lines in

the boxes represent the c-axis orientations of the crystals. As the wave in the RVE is always applied and propagates along the z-axis, the evaluation in d_2 may be simulated by rotating the whole model in Figure 3.9b to the required configuration such that d_2 is parallel with z. As a result, the orientations of the crystals are also rotated accordingly with respect to the global coordinate system, as shown by the red lines in Figure 3.9c opposed to the blue ones, but their relative orientations to d_2 remain unchanged. Next, as shown by Figure 3.9d, the rotated orientations are retained and input into the RVE model, which ensures that the waves in d_2 go through the same collective crystallographic texture with d_1; and the rotated crystal morphologies is again discarded, as we did in the un-rotated model in the first instance. Figure 3.9 illustrates the idea in two dimensions, but it applies to three dimensional case too, where the orientation of every crystal in the model is subject to the same additional rotation to the configuration corresponding to the desired evaluation direction denoted by θ and ϕ. That is to say that if the sample is associated with a sample system o-xyz and the wave excitation direction with a rotated system o-$x'y'z'$, then evaluating the wave velocity with respect to o-xyz is equivalent to always evaluating the velocity in o-$x'y'z'$ coordinate system with all crystals rotated to its configuration given by $-\theta$ and $-\phi$. This may be achieved using the following rotation matrix applied to each crystal in the aggregate:

$$R = \begin{pmatrix} \cos\theta\cos\phi & -\cos\theta\sin\phi & \sin\theta \\ \sin\phi & \cos\phi & 0 \\ -\sin\theta\cos\phi & \sin\theta\sin\phi & \cos\theta \end{pmatrix} \tag{3.35}$$

3.4.3 Results from the convolution model

- **Texture SH coefficients & pole figure**

The nine progressively changing model experimental textures shown in Figure 3.7 are the subjects of our inverse studies. The first step is to obtain the velocity variations with polar and azimuthal angles $v(\theta_i, \phi_j)$ which correspond to each of these textures. Hence, for each texture, 12×6 velocities at the corresponding Gaussian-Legendre grids are simulated using the FE RVE model with configurations specified by equation 3.35. The SH coefficients of the polycrystal velocities are calculated from the velocity variations based on the numerical integration given by equation 3.34; then the texture SH coefficients are obtained by de-convolving the single crystal properties from those of the polycrystal through a pointwise division based on the spherical harmonic theorem in equation 3.24. Finally, the orientation distribution of the polycrystal is reconstructed using the SH texture coefficients from which pole figures in any required orientation may be obtained. The resulting predicted ODF coefficients for the texture a in Figure 3.7 are detailed in Table 3.7 alongside the original ones, and the predicted pole figures for all the nine textures given in Figure 3.7 obtained using the computational velocity data and the de-convolution technique are shown in Figure 3.10.

Note however, that the normalization convention of the SH coefficients used in reconstructions of the pole figures is different to that defined by equations 3.1 and 3.11 and is actually given by:

$$Q_{lm}(plot) = 2\sqrt{\pi} \cdot Q_{lm}. \tag{3.36}$$

This is carried out to ensure that the pole figure density is equal to 1 when the orientation distribution is random [99].

Table 3.7: SH coefficients and pole figures for texture **a** in Figure 3.7: original ones and ones determined using the de-convolution technique

Original textures (truncated to 4th degree)	Predicted by de-convolution
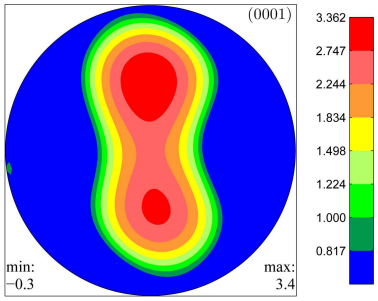	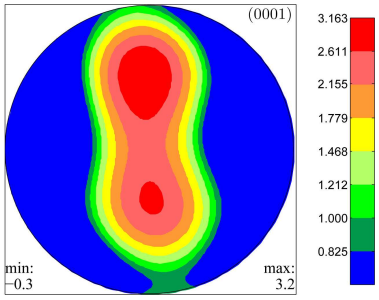
$Q_{00} = 0.2821$	$Q_{00} = 0.2815$
$Q_{20} = 0.18025$	$Q_{20} = 0.17309$
$Q_{21} = 0.02376 - 0.00320i$	$Q_{21} = 0.02057 - 0.00294i$
$Q_{22} = 0.08062 + 0.01204i$	$Q_{22} = 0.08593 + 0.01165i$
$Q_{40} = -0.00261$	$Q_{40} = 0.00171$
$Q_{41} = -0.00642 + 0.00100i$	$Q_{41} = -0.01163 + 0.00991i$
$Q_{42} = 0.10450 + 0.00821i$	$Q_{42} = 0.08279 + 0.00856i$
$Q_{43} = 0.01641 - 0.01143i$	$Q_{43} = 0.02870 + 0.00507i$
$Q_{44} = 0.03506 + 0.02266i$	$Q_{44} = 0.04192 + 0.02338i$

- **Retrieving Kearns' factors**

It was mentioned in the introduction that Kearns' factors, a sub-fraction of information contained in pole figures, are also widely employed in descriptions of textures in HCP polycyrstals, especially in zirconium alloys. They are written with respect to

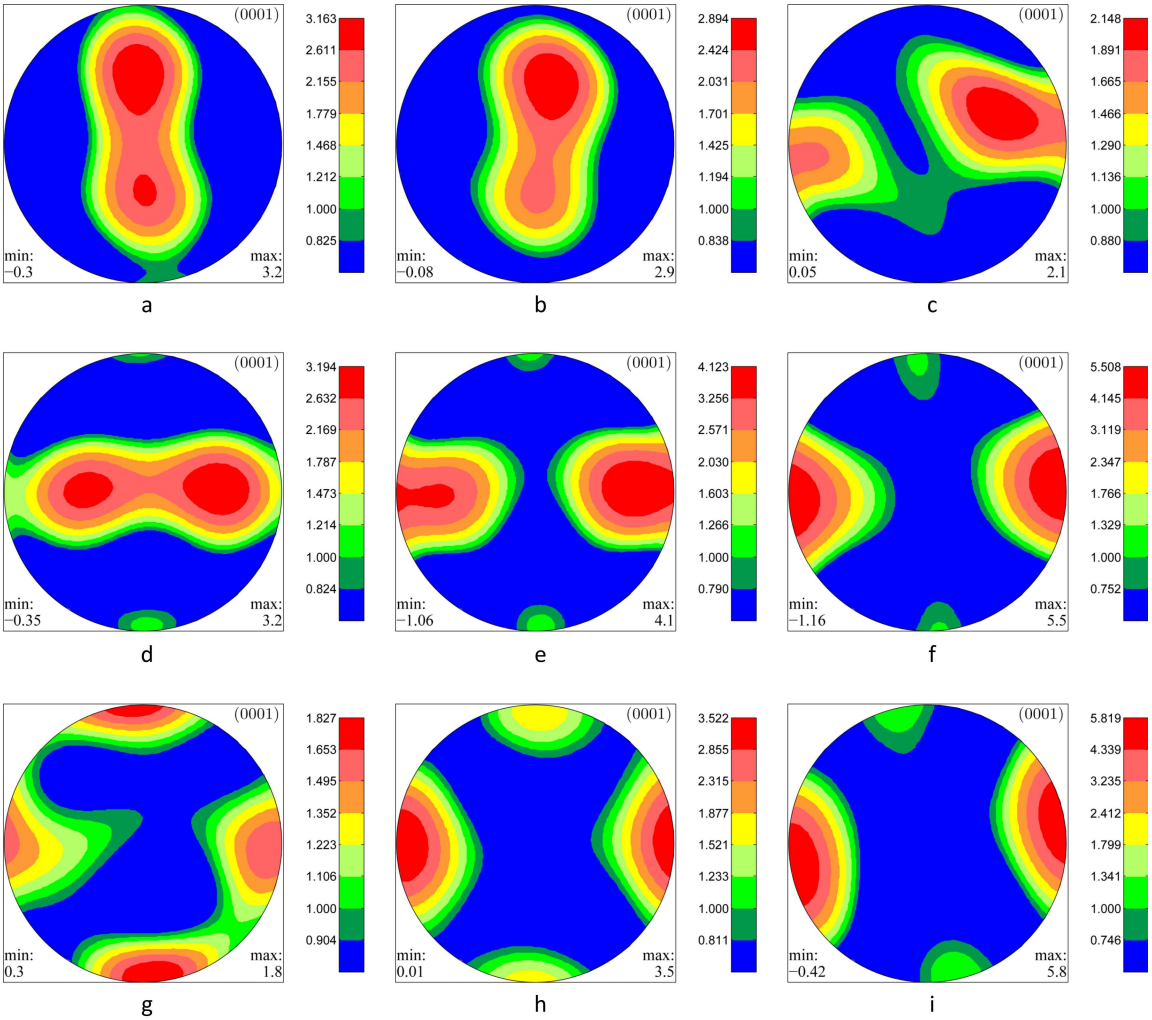

Figure 3.10: The pole figures predicted from the de-convolution technique for the different representative experimental textures.

the c-axis distribution function $q(\theta, \phi)$ here:

$$
\begin{aligned}
f_{\mathrm{RD}} &= \frac{1}{N} \int_0^{2\pi} \int_0^{\pi/2} q(\theta, \phi) \sin^3(\theta) \cos^2 \phi \; d\phi d\theta \\
f_{\mathrm{TD}} &= \frac{1}{N} \int_0^{2\pi} \int_0^{\pi/2} q(\theta, \phi) \sin^3(\theta) \sin^2 \phi \; d\phi d\theta \\
f_{\mathrm{ND}} &= \frac{1}{N} \int_0^{2\pi} \int_0^{\pi/2} q(\theta, \phi) \sin(\theta) \cos^2 \theta \; d\phi d\theta
\end{aligned}
\tag{3.37}
$$

where N is a normalisation constant defined as

$$N = \int_0^{2\pi} \int_0^{\pi/2} q(\theta, \phi) \sin(\theta)\ d\phi d\theta. \tag{3.38}$$

Equation 3.11, which expands the function $q(\theta, \phi)$ into spherical harmonic series, can be substituted back into equations 3.37 and 3.38 for the numerical calculations of the factors. For example, f_{RD} is now transformed into

$$\begin{aligned} f_{\mathrm{RD}} &= \frac{1}{N} \int_0^{2\pi} \int_0^{\pi/2} \sum_{l=0}^{+\infty} \sum_{m=-l}^{l} Q_{lm} Y_{lm}(\theta, \phi) \sin^3(\theta) \cos^2\phi\ d\phi d\theta \\ &= \frac{1}{N} \sum_{l=0}^{+\infty} \sum_{m=-l}^{l} Q_{lm} \int_0^{2\pi} \int_0^{\pi/2} Y_{lm}(\theta, \phi) \sin^3(\theta) \cos^2\phi\ d\phi d\theta \\ &= \frac{1}{N} \sum_{l=0}^{+\infty} \sum_{m=-l}^{l} Q_{lm} C_{lm} \end{aligned} \tag{3.39}$$

where C_{lm} are constants of degree l and order m calculated via

$$C_{lm} = \int_0^{2\pi} \int_0^{\pi/2} Y_{lm}(\theta, \phi) \sin^3(\theta) \cos^2\phi\ d\phi d\theta. \tag{3.40}$$

The other factors f_{TD}, f_{ND} and N can all be calculated similarly. The expansion in equation 3.39 may also be truncated up to a certain degree l_0 as well; in our case, for instance, it is again truncated to the 4th degree. With the texture coefficients for Texture a recovered in Table 3.7, the Kearns' factors are retrieved as an example of how the technique works, and the results are shown in comparison with the original factors in Table 3.8.

3.4.4 Discussions

Nine representative HCP textures quantified by orientation distribution functions, for which (0001) pole figures are shown in Figure 3.7, have been implemented into

Table 3.8: Kearns' factors calculated from original textures (truncated to 16th degree) and from the retrieved SH coefficients for Texture **a** in Figure 3.7

	f_{RD}	f_{TD}	f_{ND}
Original	0.342	0.134	0.524
Retrieved	0.353	0.130	0.516

an RVE finite element model subjected to simulated ultrasonic wave excitation and the resulting wave velocity dependence on incident wave direction determined. These data are representative of experimental ultrasonic measurements of wave velocity, and have been taken as the starting point for proof of principle of determination of texture (pole figures) from knowledge of ultrasonic velocity profiles.

The velocity data have been expressed as a spherical harmonic expansion together with that for the single crystal velocity response (the kernel function). The deconvolution technique presented above has then been utilized to extract out the spherical harmonic expansion, and corresponding function coefficients, up to order four, for the orientation distribution function, as listed in Table 3.7, along with those for the original distribution input to the RVE model. It is evident that the SH coefficients are retrieved with reasonably good numerical accuracy; some ones, for example Q_{40}, are not well recovered only because the original coefficients are too small, hence have minimal impact on the polycrystal wave speed (and on the reconstructed pole figure too). It also needs to be noticed that as a result of the recovered coefficients being truncated up to 4th degree only, the intensities in the reconstructed pole figures are not directly comparable to those in EBSD figures, which are normally truncated to 16th or even 32th degrees. However, if the original EBSD texture is also truncated to 4th degree, as shown in Table 3.7, it can be seen that the pole figure is in fact very well recovered from the wave velocities.

The recovered c-axis distribution function has then enabled the (0001) pole figures to

be shown graphically in Figure 3.10, such that comparisons between the original pole figures in Figure 3.7 and those predicted from the de-convolution of velocity profiles may be drawn. From the two figures, it can be seen that the predicted pole figures lack some of the detail, and sharpness, of the originals, but nonetheless provide very substantively the texture information sought, and this has been established over a broad range of differing HCP textures. It is again apparent that for strongly preferred distributions, the magnitude of the intensity drops considerably; in addition, for some of the predicted pole figures, it may be seen that the smallest intensity is less than zero, and the stronger the texture, the bigger the magnitude. Both phenomena are likely caused predominantly by the truncation of the SH coefficients, coupled with the crystal to crystal interactions which are ignored in the de-convolution technique. In its own right, however, the combination of both magnitudes in each figure is useful in the sense of being indicative of the original intensities, given that those magnitudes for the extreme cases (random texture and single crystals) are easily calculatable and those for a range of differing textures have already been established, which suggests that it is possible to mathematically re-scale the intensities to match the original, un-truncated ones. In additional to the pole figures, the Kearns' factors are also recovered with satisfactory accuracies.

The de-convolution technique presented therefore provides a solution to the well-known inverse problem in texture, and proof of principle has been established that full three-dimensional, bulk texture measurements may be made in HCP polycrystals from ultrasonic wave velocity measurements. The current work has utilized simulation-generated wave velocity profiles to demonstrate proof of principle. However, the direct experimental measurement of ultrasonic wave velocity is now well established and current techniques include the phased-array [100] approach in which an array of transducers is employed both to emit and receive ultrasonic signals over an area, for example, facilitating the provision of ultrasonic wave speeds in many

directions within the material, precisely as required by our de-convolution technique. Naturally, the same requirements for statistically homogeneous texture within the bulk of the polycrstal material still hold, but it is to be hoped that, through definition of an appropriately sized volume, the spatial variations of texture may now be explored using ultrasonic techniques combined with de-convolution. The prospect for three-dimensional bulk component measurement of texture is therefore much closer.

SECTION. 3.5

Conclusions

A new convolution approach which couples single HCP crystal wave velocity (the kernel function) response to incident wave angle with the orientation distribution function in order to provide the polycrystal velocity response has been established. The kernel function, orientation distribution function and polycrystal wave velocity response are represented using spherical harmonic expansions therefore providing full three-dimensional spherical characterisation of all three functions, and importantly, the potential for de-convolution when knowledge of two out of the three functions is known.

In the forward problem, the convolution tecnnique has been shown to allow polycrystal wave speed to be determined from knowledge of the polycrystal orientation distribution and the single crystal wave speed response (and other kernels) to orientation. The polycrystal wave speeds were predicted for a broad range of nine representative experimental single-phase HCP textures showing perfect sensitivity of wave speed to texture and quantitatively good agreement with wave velocity.

It has been demonstrated that the technique allows for de-convolution to be carried out so that with knowledge of the single crystal wave speed response to orientation, and the polycrystal wave speed response, it is now possible to de-convolve the underlying crystallographic orientation distribution up to degree four in the c-axis pole distribution function spherical harmonic expansion. The de-convolution process has been demonstrated for the nine representative HCP polycrystal textures for which knowledge of their wave velocity responses, together with the underlying single-crystal wave response, has been employed to extract out the polycrystal orientation distribution function. The pole figures predicted in this way have been compared with the original polycrystal pole figures from which the wave velocity profiles were obtained,

showing very good quantitative agreement.

It has been demonstrated that the order of the spherical harmonic expansion of the kernel function – here the single crystal wave velocity response to wave incident angle – explains why it has been widely reported in the literature that only texture coefficients up to 4th degree may be obtained from ultrasonic measurements.

Convolution kernels of velocity and slowness give polycrystal wave speeds which lie between the Voigt and Reuss methods which verifies Hill's conclusion that the latter methods set up the upper and lower bounds for the polycrystal elastic stiffnesses.

Finally, proof of principle has been established that texture measurement may be made for HCP polycrystals from knowledge of their ultrasonic wave speed response to orientation.

4

The Inverse Studies II: The Generalized Theorem and Solutions to Cubic Textures

It has been demonstrated in the previous chapter that with a single Hexagonal Close-Packed (HCP) crystal simplified to be elastically isotropic about its c-axis and the ODF of the polycrytal simplified to be the pole distributions of the c-axes, the convolution of the pole distribution and the single crystal velocity function by means of spherical harmonics gave the polycrystal velocity response; this spherical convolution theorem enabled the solution for one variable with knowledge of any two of the three variables (c-axes pole distribution, single crystal velocity function, and polycrystal velocity function), hence providing a solution to both the forward and inverse studies for (simplified) HCP polycrystals.

However, the simplification of the ODF to the c-axes pole distributions during the deduction of the theorem for HCP crystals in the previous chapter means that it is not applicable to cubic materials, or indeed any more generalised crystal classes, whose orientation presentations need all three Euler angles. This problem is solved in this chapter. By taking full account of the three Euler angles, the spherical convolution theorem is expanded into a generalised form which applies to all crystal classes when performing forward and inverse studies.

This chapter is structured in the following order: first, in the Background section the

mathematical description of the ODF is given and the single crystal velocity function of a cubic crystal is analyzed; then the analytical model of the relationship between the ODF, single crystal and polycrystal velocity functions is established, followed by the decompositions of the relationship by means of spherical harmonics and Wigner-D functions, which lead to the generalised spherical convolution theorem. The theorem is then applied in forward studies for both theoretical distributions of cubic crystals and three experimental polycrystal textures. Finally, proof of principle is established for the experimental textures for the solution of the inverse problem, that is, texture, or determination of the orientation distribution function from ultrasonic analyses.

SECTION. 4.1

Background: the ODF and single crystal wave speed for crystals with general symmetries

4.1.1 Orientation distribution function (ODF)

As already introduced previously, the specific orientation of a crystal within a polycrystalline sample is fully captured by means of the three Euler angles, as shown in Figure 4.1, where there are two sets of coordinate systems defined: one is the sample system o-xyz, whose x, y and z axes are often taken to be along the rolling (RD), transverse (TD) and normal (ND) directions of the sample, respectively; and the other is the crystal system o-XYZ associated with the specific crystal with an arbitrarily rotated orientation from the sample system. The Euler angles β, α and γ are then employed to apply the rotation from o-xyz to o-XYZ following the sequence of Z-Y'-Z''. Note that the sequence used in this thesis follows those employed by Roe [39] and Matthies [13] given its consistency with the subsequent analyses, and it is different from that used by Bunge [10, 12] whose rotation sequence is Z-X'-Z''.

Therefore, the statistical description of the distributions of the crystallographic orientations within the sample can be described by a probability function of the Euler angles. Often referred to as the orientation distribution function (ODF), the function can be written as $w(\alpha, \beta, \gamma)$ satisfying the following requirement:

$$\int_0^{2\pi} \int_0^{2\pi} \int_0^{\pi} w(\alpha, \beta, \gamma) \sin\alpha d\alpha d\beta d\gamma = 1. \tag{4.1}$$

4.1.2 Velocities of a single crystal

Similarly with the analyses on the HCP crystal in the previous chapter, the elastic stiffnesses of the general single crystal are needed in order to investigate the

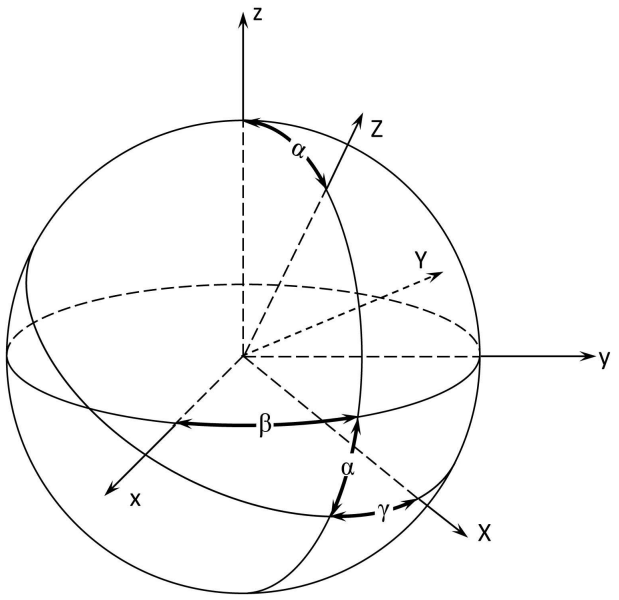

Figure 4.1: The three Euler angles to rotate the sample system *o-xyz* to the crystal system *O-XYZ*.

ultrasonic wave velocity propagating through it along an arbitrary direction in three-dimensional space. A single crystal α-phased Fe, for example, has the following stiffness matrix(with units of GPa) at room temperature [32]:

$$\mathbf{C} = \begin{pmatrix} 228.09 & 133.48 & 133.48 & & & & \\ 133.48 & 228.09 & 133.48 & & & & \\ 133.48 & 133.48 & 228.09 & & & & \\ & & & 110.87 & & & \\ & & & & 110.87 & & \\ & & & & & 110.87 & \end{pmatrix} \tag{4.2}$$

And the ultrasonic wave velocity in any given direction $\mathbf{n} = \begin{pmatrix} n_1 & n_2 & n_3 \end{pmatrix}^{\mathrm{T}}$ for the single Fe crystal can be estimated through the well-known Christoffel equation by substituting 4.2 and $\mathbf{n}$ into the equations given in Section 2.1, which ultimately leads

to a classic eigenvalue-eigenvector problem, with the eigenvalues of the Christoffel matrix directly linked to three phase velocities (one longitudinal and the other two shear) and the three eigenvectors being the respective particle displacement directions corresponding to the phase velocities.

Note that our principal interests in this study still lie with the fastest bulk wave; that is, the longitudinal wave. However, in an arbitrary direction $\mathbf{n}$ within generally anisotropic materials, even though the three particle displacement vectors are mutually orthogonal, none of them actually lies parallel with $\mathbf{n}$, meaning that the fastest phase velocity obtained through the Christoffel equation is in fact *quasi*-longitudinal. It is shown in Appendix B that while the angular difference between $\mathbf{n}$ and its closest eigenvector is generally small and negligible for HCP materials simplified to be transversely isotropic, it can be rather significant for cubic materials whose anisotropies are more pronounced. It is important to be aware of this difference in the studies of this chapter, and this will be discussed further in the later sections.

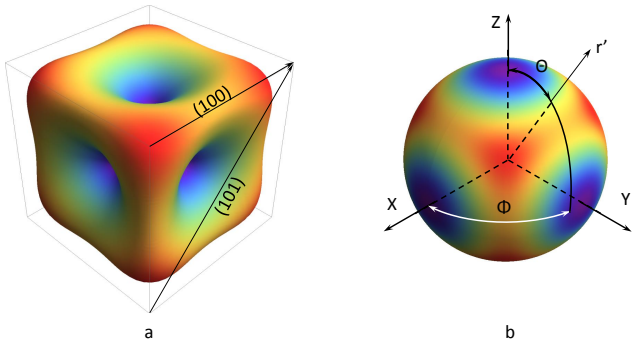

Figure 4.2: The single crystal velocity surface of Fe, with: a. the velocity variation as the explicit surface shape; b. as the colour change. The single crystal velocity in an arbitrary direction $\mathbf{r}'$ is determined by its polar angle Θ and azimuthal angle Φ with respect to the crystal system $o\text{-}XYZ$.

The ultrasonic wave velocities of a single crystal in all directions of the space form its

velocity surface, which is also a rough evaluation of the elastic stiffnesses-to-density ratio of the crystal given the dependence of the wave velocity on the ratio. The single crystal velocity surface of α-phased Fe is plotted in Figure 4.2, with the velocity variations shown as explicit shape change of the surface in Figure 4.2a and colour variations on the surface of the unit sphere in Figure 4.2b. It can be seen that all the symmetries of a cubic crystal, including four-fold symmetries about the Z-axis and all the mirror planes, are well preserved on the velocity surface, which agrees with Neumann's Principle. Moreover, the wave velocity in an arbitrary direction $\boldsymbol{r'}$ is determined by the combination of its polar angle Θ and azimuthal angle Φ with respect to the crystal system o-XYZ. So if the single crystal velocity surface is written as a function k, the velocity in direction $\boldsymbol{r'}$ is

$$k(\boldsymbol{r'}) = k(\Theta, \Phi). \tag{4.3}$$

SECTION. 4.2

Theoretical Framework for Studies on General Crystals

In this section, the analytical model and the relationship between the single crystal wave velocity function, ODF and polycrystal velocity function are constructed. Similar ideas to those presented in the previous chapter for HCP materials are employed, but now with full consideration of all three Euler angles.

4.2.1 Refinement of the grain average model

When an ultrasonic wave is excited into a sample from a point source, its three-dimensional wavefront expands out approximately as a sphere, with some distortions introduced by the anisotropy within the polycrystal; and if only the wave propagation in a certain direction is of interest, the problem can be simplified to be a wave going through an array of crystals in a straight line.

Consider the case shown in Figure 4.3 where the wave goes through a cubic polycrystalline aggregate in the direction of $\boldsymbol{r}$, with the mini-cubes on each crystal in the figure representing its crystallographic orientation. The wave velocities in different crystals are different, and the overall velocity through the aggregate can be calculated via the grain average method. Each crystal introduces a local coordinate system o-$X_iY_iZ_i$, about which the wave propagation direction $\boldsymbol{r}$ is evaluated to give the velocity through this particular crystal; then the contributions to the overall velocity in the direction from all grains are summed up one by one with regards to the volume fractions of their specific crystallographic orientations.

The wave velocity in the ith crystal is determined in such a way that if the direction $\boldsymbol{r}$ with respect to the local crystal system is denoted as $\boldsymbol{r_i'}$, and the latter is described by its polar angle Θ_i and azimuthal angle Φ_i, then the wave velocity is $k(\Theta_i, \Phi_i)$

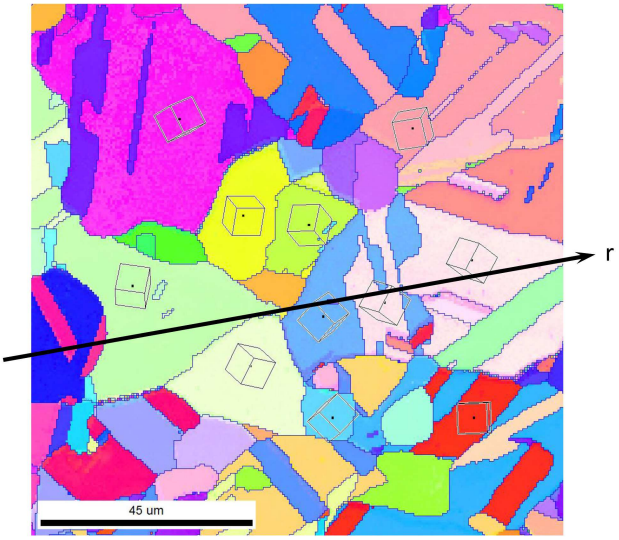

Figure 4.3: A wave going through a polycrystalline aggregate in direction $\boldsymbol{r}$. The boxes on the crystals represents the respective crystallographic orientations (EBSD grain map courtesy of Dr Jun Jiang, Dr Ben Britton and Professor Angus Wilkinson [101]).

according to equation 4.3. Meanwhile, if the volume fraction of crystals with the orientation (α, β, γ) is described by a function $g(\alpha, \beta, \gamma)$, the overall wave velocity through the aggregate in $\boldsymbol{r}$ can be calculated by:

$$v(\boldsymbol{r}) = \sum k(\boldsymbol{r_i'}) \cdot g(\alpha_i, \beta_i, \gamma_i). \tag{4.4}$$

In reality, however, the crystallographic orientation does not necessarily remain uniform even within the same grain, so the same treatment as the previous chapter is adopted here, which allows the orientations to vary continuously rather than keeping the averaging unit as a whole grain. As a result, the summation in equation 4.4 becomes an integration:

$$v(\alpha, \beta, \gamma) = \int_0^{2\pi} \int_0^{2\pi} \int_0^{\pi} k(\boldsymbol{r'}) \cdot g(\alpha, \beta, \gamma) \sin\alpha d\alpha d\beta d\gamma \tag{4.5}$$

Now consider the wave propagations through a full three-dimensional polycrystalline aggregate which is statistically homogeneous in such a way that when evaluating from any direction in the space, the waves all go through the same texture. The analytical equation 4.5 also applies for this case if $\boldsymbol{r}$ is allowed to cover all the directions in the space.

The $\boldsymbol{r}$ on the left-hand side of equation 4.5 is the wave incident direction described by its polar angle θ and azimuthal angle ϕ with respect to the sample system *o-xyz*; the $\boldsymbol{r'}$ on the right-hand side of the equation is essentially the same direction vector as $\boldsymbol{r}$, but given with respect to the crystal system *o-XYZ* and is described by Θ and Φ. In addition, *o-XYZ* is linked with *o-xyz* via the rotation of the coordinate system using the Euler angles (α, β, γ), which, according to the conventions in quantum mechanics [40], is a *passive* rotation, and its corresponding *active* operator $R^{(\alpha,\beta,\gamma)}$ to rotate the wave incident direction *vector* $\boldsymbol{r}$ to $\boldsymbol{r'}$ can be constructed accordingly using the same set of Euler angles:

$$(\Theta, \Phi) = R^{(a)}(\alpha, \beta, \gamma) \cdot (\theta, \phi) = R_z^{(a)}(\beta) \cdot R_y^{(a)}(\alpha) \cdot R_z^{(a)}(\gamma) \cdot (\theta, \phi) \tag{4.6}$$

where $R_z^{-\beta}$, for example, means to rotate the vector about the z-axis with an offset of $-\beta$.

Now that the orientation (α, β, γ) varies continuously in the three-dimensional space, the volume fraction function $g(\alpha, \beta, \gamma)$ follows the same concept with the ODF w defined in equation 4.1. Replacing g with w in equation 4.5 and substituting equation 4.6 back into 4.5 lead to:

$$\begin{aligned} v(\theta, \phi) &= \int_0^{2\pi} \int_0^{2\pi} \int_0^{\pi} k(\Theta, \Phi) w(\alpha, \beta, \gamma) \sin\alpha d\alpha d\beta d\gamma \\ &= \int_0^{2\pi} \int_0^{2\pi} \int_0^{\pi} k(R^{(a)}(\alpha, \beta, \gamma) \cdot (\theta, \phi)) w(\alpha, \beta, \gamma) \sin\alpha d\alpha d\beta d\gamma. \end{aligned} \tag{4.7}$$

This is the final grain average analytical model to describe the relationship between polycrystal velocity function v, the single crystal velocity function k and the ODF w in the three-dimensional space. The function k serves as a bridge to connect v and w and is therefore called the kernel of the relationship.

4.2.2 Generalised spherical convolution theorem

It has been shown in Chapter 3 that the relationship shown by the analytical equation 4.7 can be further exploited by means of the spherical harmonic (SH) expansion, and here the same technique is employed again.

The definition and description of the spherical harmonic bases were introduced in Section 3.2.2, and I now begin the analysis on equation 4.7 by expanding its kernel function $k(\Theta, \Phi)$ in terms of the spherical harmonics associated with the local crystal system $o\text{-}XYZ$:

$$k(\Theta, \Phi) = \sum_{l=0}^{\infty} \sum_{n=-l}^{l} K_{ln} Y_{ln}(\Theta, \Phi) \tag{4.8}$$

where the SH coefficients K_{ln} are calculated by projecting the original function onto the complex conjugates of the SH bases:

$$K_{ln} = \int_0^{2\pi} \int_0^{\pi} k(\Theta, \Phi) Y_{ln}^*(\Theta, \Phi) \sin\Theta d\Theta d\Phi \tag{4.9}$$

where $Y_{ln}^*(\Theta, \Phi)$ stands for the complex conjugate of $Y_{ln}(\Theta, \Phi)$.

The next step is to establish connections between the expansion of the kernel in equation 4.8, which is with respect to the crystal system $o\text{-}XYZ$, and the sample system $o\text{-}xyz$. As introduced in Chapter 3, it can be done with help of the Wigner-D matrix $D^l(\alpha, \beta, \gamma)$, which is a $(2l+1) \times (2l+1)$ dimensioned matrix containing the information to express a set of l-degree spherical harmonics as the linear combinations of another set of rotated l-degree harmonics. The elements of the Wigner-D matrix

are defined as:

$$D^l_{mn}(\alpha,\beta,\gamma) = e^{im\beta} d^l_{mn}(\alpha) e^{in\gamma} \tag{4.10}$$

where $-l \leq m, n \leq l$, and the $d^l_{mn}(\alpha)$ are the elements of the Wigner-d matrix directly related to the Jacobi polynomials. $d^l_{mn}(\alpha)$ follow a similar concept with $Z_{lmn}(\cos\alpha)$ defined by Roe in [39], but are not normalized. Now $Y_{ln}(\Theta,\Phi)$ can be related to the harmonics with respect to the sample system through the Wigner-D matrices, as shown in [94]:

$$Y_{ln}(\Theta,\Phi) = \sum_{m=-l}^{l} D^{l*}_{mn}(\alpha,\beta,\gamma) Y_{lm}(\theta,\phi). \tag{4.11}$$

Substituting equation 4.11 back to 4.8 makes the kernel function $k(\theta,\phi)$ further expanded into

$$k(\Theta,\Phi) = \sum_{l=0}^{\infty} \sum_{n=-l}^{l} K_{ln} \sum_{m=-l}^{l} D^{l*}_{mn}(\alpha,\beta,\gamma) Y_{lm}(\theta,\phi) \tag{4.12}$$

Now the focus turns to the ODF $w(\alpha,\beta,\gamma)$. As shown by Kostelec et al [102], the Wigner-D matrices also form a complete set of orthogonal bases, and the ODF, or indeed any function of the rotation group SO(3) defined by the three Euler angles, have the following decomposition:

$$w(\alpha,\beta,\gamma) = \sum_{l=0}^{\infty} \sum_{m=-l}^{l} \sum_{n=-l}^{l} \frac{2l+1}{8\pi^2} \cdot W_{lmn} D^l_{mn}(\alpha,\beta,\gamma) \tag{4.13}$$

where the coefficients $\frac{2l+1}{8\pi^2}$ result from the fact that the Wigner-D matrices are not normalized, and the expansion coefficients W_{lmn} are obtained via:

$$W_{lmn} = \int_0^{2\pi} \int_0^{2\pi} \int_0^{\pi} w(\alpha,\beta,\gamma) D^{l*}_{mn}(\alpha,\beta,\gamma) \sin\alpha d\alpha d\beta d\gamma. \tag{4.14}$$

Here $D^{l*}_{mn}(\alpha,\beta,\gamma)$ stands for the complex conjugate of $D^l_{mn}(\alpha,\beta,\gamma)$.

Substituting equations 4.12 and 4.13 back into 4.7 transforms the latter into:

$$\begin{aligned} v(\theta,\phi) &= \int_0^{2\pi}\int_0^{2\pi}\int_0^{\pi} k(R^{(\alpha,\beta,\gamma)}(\theta,\phi))w(\alpha,\beta,\gamma)\sin\alpha d\alpha d\beta d\gamma \\ &= \sum_{l_1=0}^{\infty}\sum_{m=-l_1}^{l_1}\sum_{n_1=-l_1}^{l_1} K_{l_1 n_1} Y_{l_1 m_1}(\theta,\phi)\cdot\sum_{l_2=0}^{\infty}\sum_{m_2=-l_2}^{l_2}\sum_{n_2=-l_2}^{l_2}\frac{2l+1}{8\pi^2}W_{l_2 m_2 n_2}\cdot T_{l_1,n_1,n_1,l_2,m_2,n_2} \end{aligned} \tag{4.15}$$

and the term $T_{l_1,n_1,n_1,l_2,m_2,n_2}$ can be simplified according to the orthogonality (but not normalization) of the Wigner-D matrix into:

$$\begin{aligned} T_{l_1,n_1,n_1,l_2,m_2,n_2} &= \int_0^{2\pi}\int_0^{2\pi}\int_0^{\pi} D^{l_1 *}_{m_1 n_1}(\alpha,\beta,\gamma)\cdot D^{l_2}_{m_2 n_2}(\alpha,\beta,\gamma)\sin\alpha d\alpha d\beta d\gamma \\ &= \frac{8\pi^2}{2l+1}\delta_{l_1,l_2}\delta_{m_1,m_2}\delta_{n_1,n_2} \end{aligned} \tag{4.16}$$

where $\delta_{a,b}$ is the Kronecker delta function equal to 1 if and only if $a = b$. So equation 4.16 enforces $l_1 = l_2$, $m_1 = m_2$ and $n_1 = n_2$, which turns equation 4.15 into:

$$v(\theta,\phi) = \sum_{l=0}^{\infty}\sum_{m=-l}^{l}\sum_{n=-l}^{l} W_{lmn}K_{ln}\cdot Y_{lm}(\theta,\phi) \tag{4.17}$$

And this means that if the polycrsytal velocity function v is decomposed in terms of spherical harmonics, its coefficients are:

$$V_{lm} = \sum_{n=-l}^{l} W_{lmn}K_{ln} \tag{4.18}$$

Equations 4.17 and 4.18 form the generalised convolution theorem for the analysis of the relationship between the polycrystal velocities, single crystal velocities and the crystallographic orientation distribution function.

4.2.3 Discussions of the approach

- **Normalization conventions of W_{lmn}**

There are different normalization conventions for the decomposition bases and W_{lmn} in the literature. Roe [39], for example, used normalized Wigner-D matrices as the decomposition bases, therefore the coefficients obtained in [39] have the following relationship with the W_{lmn} used in this thesis:

$$W_{lmn} = \frac{2}{2l+1} \cdot W_{lmn}(\text{Roe's}) \tag{4.19}$$

The most widely used normalization convention of W_{lmn} in the metal industries, however, is half of Roe's such that the ODF $w(\alpha, \beta, \gamma)$ always exhibit unity when the texture is random [99]. The relationship between this convention and our W_{lmn} is therefore:

$$W_{lmn} = \frac{1}{2l+1} \cdot W_{lmn}(\text{Industrial}) \tag{4.20}$$

- **Using the theorem for forward studies**

The deductions of equations 4.17 and 4.18 have taken full account of all three Euler angles, which, no matter what type of structure a crystal belongs to, provides enough information to describe its exact orientation. Hence the theorem applies to all types of crystal structures.

When the texture information is known, applying equation 4.18 from the right side to the left is the forward study process: the ODF expansion coefficients W_{lmn} can be calculated from the texture information using equation 4.14 (for which the MTEX toolbox for Matlab [86] is a very useful tool); then the SH coefficients V_{lm} of the polycrystal velocity function are obtained by inputting the coefficients of the ODF and the kernel (single crystal velocity function) to equation 4.18; finally, the polycrystal

velocity function is reconstructed based on the obtained V_{lm}, the velocity surface is established and the wave speeds in all directions of the space are predicted. Again, this process can be done for all types of crystal structures.

However, for the inverse study process where the polycrystal velocity function is known and the ODF is needed, it is not possible for all types of crystal structures to retrieve the ODF coefficients by using the theorem from the left side to the right. The reason is that for an arbitrary crystal structure, there are $2l + 1$ unknown variables $W_{lmn}(-l \leq n \leq l)$ for a given set of l and m to be solved from equation 4.18 only, which is not theoretically possible. However, there are two exceptions, being HCP and cubic crystal structures, whose ODF coefficients W_{lmn} both have only one independent unknown variable (at least up to a certain l) for a given set of l and m, but in two different ways. Therefore equation 4.18 can be solved and the ODF information can be recovered from the polycrystal velocity functions for these two types of crystals.

- **Using the theorem for inverse studies on HCP materials**

The inverse study on HCP materials was fully analysed in the previous chapter, and it can be proved that the spherical convolution theorem obtained specifically for HCP materials is actually a special case of the generalised convolution theorem described by equations 4.17 and 4.18.

As an HCP crystal is often simplified as transversely isotropic about its c-axis, only one angle in the crystal system is needed to determine the wave velocity in a given direction; that is, the polar angle Θ (which is also the angle between the wave direction and the c-axis of the crystal), and the kernel has no dependence on the azimuthal angle Φ. This means the coefficients of the kernel K_{ln} have non-zero values only when $n = 0$, which simplifies equation 4.18 to be:

$$V_{lm} = W_{lm0} K_{l0} \tag{4.21}$$

In addition, if the distribution intensity of the (0001) pole within an HCP aggregate is denoted as a function q, then its SH coefficients Q_{lm} are related with the ODF coefficients W_{lm0} by:

$$Q_{lm} = \sqrt{\frac{2l+1}{4\pi}} \cdot W_{lm0} \tag{4.22}$$

Substituting equation 4.22 back into 4.21 makes the latter into the spherical convolution theorem for HCP materials in equations 3.23 and 3.24, which proves the compatibility of the generalised theorem with HCP materials and that the HCP theorem is indeed a special case of the generalised one.

- **Using the theorem for inverse studies on cubic materials**

With all the symmetries of a cubic crystal considered, there are in total 24 equivalences for an arbitrary crystallographic orientation, and they must be taken correct account of in order to obtain accurate results of the ODF coefficients for a polycrystal. This topic has been thoroughly studied in Roe's papers [39, 41], and some of the most important symmetries as well as their effects on the ODF coefficients are listed in Table 4.1.

Table 4.1: Effects of cubic crystal symmetries on the ODF coefficients, part I [39, 41]

Crystallographic symmetry elements	The effects on W_{lmn}
Antipodal symmetry (also referred to as the centrosymmetry), i.e. $(\Theta, \Phi) = (\Theta + \pi, \Phi + \pi)$	$W_{lmn} = \begin{cases} W_{lmn}, & l \text{ even} \\ 0, & l \text{ odd} \end{cases}$
Mirror planes $\perp$ X, Y, Z, and four-fold rotation symmetry about Z	$W_{lmn} = \begin{cases} W_{lm\bar{n}}, & n = 4k \\ 0, & n \neq 4k \end{cases}$ where k is integer

It is shown in Table 4.1 that the number of unknown non-zero coefficients W_{lmn} has been reduced due to symmetries, with W_{lmn} being so only when l is even and

$n = 4k$; in addition, the rotation invariance of the crystallographic orientations of a cubic crystal when the Euler angles are $\alpha = 0, \beta = \frac{\pi}{2}, \gamma = 0$ further enforces linear relationships on the remaining non-zero W_{lmn}, as proved by Roe [41] and listed in Table 4.2. Note that only the relationships for W_{lmn} with l up to 10 are shown here, and the ones for larger ls can be found in Roe's paper [41].

Table 4.2: Effects of cubic crystal symmetries on the ODF coefficients, part II [41]

degree l	Linearly independent coefficients	The other coefficients
0	W_{000}	
2	None	$W_{2mn} = 0$
4	W_{4m0}	$W_{4m4} = 0.59761430 \cdot W_{4m0}$
6	W_{6m0}	$W_{6m4} = -1.8708287 \cdot W_{6m0}$
8	W_{8m0}	$W_{8m4} = 0.37605072 \cdot W_{8m0}$ $W_{8m8} = 0.57295971 \cdot W_{8m0}$
10	W_{10m0}	$W_{10m4} = -1.0076629 \cdot W_{10m0}$ $W_{10m8} = -1.1993588 \cdot W_{10m0}$

Tables 4.1 and 4.2 demonstrate that for a certain set of l ($l \leq 10$) and m ($-l \leq m \leq l$), there is only one linearly independent ODF coefficient W_{lm0}, and all the other W_{lmn} are either equal to 0 or linearly dependent on W_{lm0}. In fact, there are more linear dependences for W_{lmn}. The relationship $W_{lm\bar{n}} = W_{lmn}$ in Table 4.2 can be proved to lead to a further implication such that:

$$W_{l\bar{m}n} = W^*_{lmn} \tag{4.23}$$

where $\bar{m}$ in $W_{l\bar{m}n}$ means $-m$, and W^*_{lmn} refers to the complex conjugate of W_{lmn}. So with considerations on all the symmetries, it may be concluded that W_{lm0} with $l \leq 10$ and $0 \leq m \leq l$ contain all the linear independent terms needed to reconstruct

the original ODF matrices. Therefore, theoretically, for these sets of l and m, equation 4.18 can be solved to obtain all the ODF coefficients, and based on the results the ODF band-limited to $l \leq 10$ can be reconstructed.

A further important point is that the kernel (single crystal velocity) function of a cubic crystal share all the symmetries listed in Tables 4.1 and 4.2, as shown by Figure 4.2, so all the effects of the symmetries in these tables are equally applicable to the kernel SH coefficients. For example, K_{ln} have non-zero value only when $l \neq 0$ and $n = 4k$, and $K_{44} = 0.59761430 \cdot K_{40}$, etc.

As an example to demonstrate more explicitly how the generalised spherical convolution theorem works on cubic materials, it is sensible to write equation 4.18 with $l = 4$ and $-4 \leq m \leq 4$ in the matrix form as:

$$\begin{pmatrix} W_{4\bar{4}\bar{4}} & 0 & 0 & 0 & W_{4\bar{4}0} & 0 & 0 & 0 & W_{4\bar{4}4} \\ W_{4\bar{3}\bar{4}} & 0 & 0 & 0 & W_{4\bar{3}0} & 0 & 0 & 0 & W_{4\bar{3}4} \\ W_{4\bar{2}\bar{4}} & 0 & 0 & 0 & W_{4\bar{2}0} & 0 & 0 & 0 & W_{4\bar{2}4} \\ W_{4\bar{1}\bar{4}} & 0 & 0 & 0 & W_{4\bar{1}0} & 0 & 0 & 0 & W_{4\bar{1}4} \\ W_{40\bar{4}} & 0 & 0 & 0 & W_{400} & 0 & 0 & 0 & W_{404} \\ W_{41\bar{4}} & 0 & 0 & 0 & W_{410} & 0 & 0 & 0 & W_{414} \\ W_{42\bar{4}} & 0 & 0 & 0 & W_{420} & 0 & 0 & 0 & W_{424} \\ W_{43\bar{4}} & 0 & 0 & 0 & W_{430} & 0 & 0 & 0 & W_{434} \\ W_{44\bar{4}} & 0 & 0 & 0 & W_{440} & 0 & 0 & 0 & W_{444} \end{pmatrix} \begin{pmatrix} K_{4\bar{4}} \\ 0 \\ 0 \\ 0 \\ K_{40} \\ 0 \\ 0 \\ 0 \\ K_{44} \end{pmatrix} = \begin{pmatrix} V_{4\bar{4}} \\ V_{4\bar{3}} \\ V_{4\bar{2}} \\ V_{4\bar{1}} \\ V_{40} \\ V_{41} \\ V_{42} \\ V_{43} \\ V_{44} \end{pmatrix} \tag{4.24}$$

In the W_{4mn} matrix of equation 4.24, m changes with rows and n with columns; while in the kernel vector K_{ln} n changes with rows. It can be seen that both W_{4mn} and K_{ln} have non-zeros only when $n = -4$, 0 or 4, while SH coefficients V_{lm} of the polycrystal velocity function can be non-zero for any m. Moreover, for the ODF coefficients W_{4mn}, only the ones in the dashed box of equation 4.24 are linearly independent,

so when V_{lm} are known, these equations can be solved one by one to obtain the full $W_{4\bar{m}n}$ matrix. This is an example with $l = 4$, but it works in the same way for all $l \leq 10$.

It is also worth pointing out that only cubic crystal symmetries have been used to aid solving the inverse problem so far, and no statistical sample symmetries have been taken into account. This means the theorem applies to all types of sample symmetries; and if there is any sample symmetries affecting the ODF coefficients, it will manifest itself in the results obtained.

- **The flexibility to change the kernel in the theorem**

In the previous chapter it was argued that the spherical convolution theorem for HCP materials had the flexibility to change the convolution kernel from ultrasonic phase velocities to slowness, group velocity, or Young's modulus, etc, and it is the same for the generalised spherical convolution theorem in this chapter. So despite that phase velocities have been used as the kernel during the deduction of the theorem equation 4.18, slowness, which is a commonly used concept to evaluate ultrasonic wave velocities in the non-destructive testing world, can also be used as the kernel to calculate the phase velocity variations in polycrystals; and single crystal group velocity and Young's modulus can be used as the kernel to calculate the resulting properties in polycrystals.

In the previous chapter it was also demonstrated that the results obtained by adopting phase velocity and slowness kernels did not in fact display significant differences as far as the longitudinal wave velocities were concerned, and that using wave velocity and slowness as kernels yielded very close representation to the actual case compared to the Voigt method. So in the following sections of this chapter, wave velocity is again adopted as the kernel in the theorem and no further comparisons between different methods are performed.

SECTION. 4.3

Forward studies: from textures to wave velocities

As mentioned before, if the ODF of a texture is known, using the generalised theorem in equation 4.18 from the right side to the left is the forward problem, where the texture information is utilized to predict the polycrystal velocities. In doing so, the kernel, which is the single crystal velocity function, is essential.

As pointed out in Section 4.2, the velocities of compression waves are proportional to the square root of the elastic stiffnesses-to-density ratio along the wave directions, and therefore the elastic moduli of a single crystal in different directions, which can also form a surface, are able to give us some hints about the actual velocity surface. A comprehensive study on the Young's modulus surfaces of a series of cubic materials, including both body-centred cubic (BCC) and face-centred cubic (FCC) crystals, was conducted by Zhang et al [32] and the plots of such surfaces are shown in Figure 4.4 for FCC and 4.5 for BCC, respetively.

It is demonstrated in 4.4 and 4.5 that even though the crystal structures of BCC and FCC are different (hence so are the plastic behaviours), the elastic properties of a BCC material can be similar to an FCC one and vice versa. For example, α-phased Fe, which is BCC-structured, has a similar single crystal Young's modulus surface (hence also the compression wave speed surface) with a group of FCC materials including Cu, Ni, Au, Ag, etc. On the other hand, the FCC-structured Al has a similar Young's modulus surface compared with Nb, Mo, V, which are all BCC; there is also a special material, W, with its single crystal almost being elastically isotropic and its Young's modulus surface approximately spherical.

For the material W, it is easy to conclude that its polycrystal longitudinal wave velocities have no dependence on texture since its single crystal response is almost isotropic. So in this section, our interests are in the other two groups of materials.

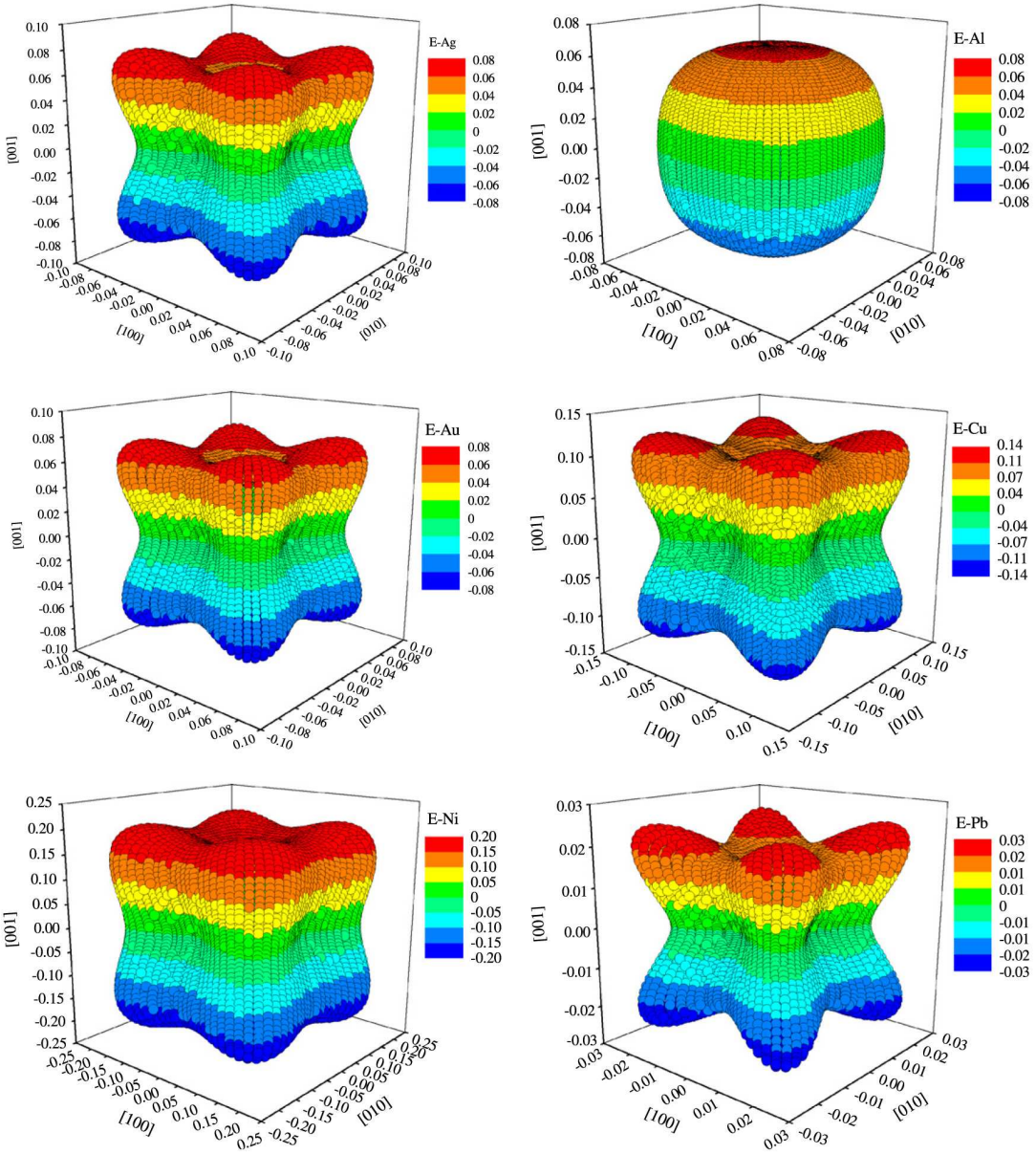

Figure 4.4: Representation surfaces of Young's modulus for FCC metals Ag, Al, Au, Cu, Ni and Pb. The length of the radius vector in the in the $[h\ k\ l]$ direction equals to E$(h\ k\ l)$ (in units of $10^{12}\ N/m^2$) [32].

I start by revealing more information on the single crystal SH coefficients of these materials, and then pick out Fe as the exemplary material to perform the forward studies, in the hope of primarily showing how the forward studies are carried out through the generalised convolution theorem, and also revealing some more subtle relationships lying between texture and polycrystal wave speeds.

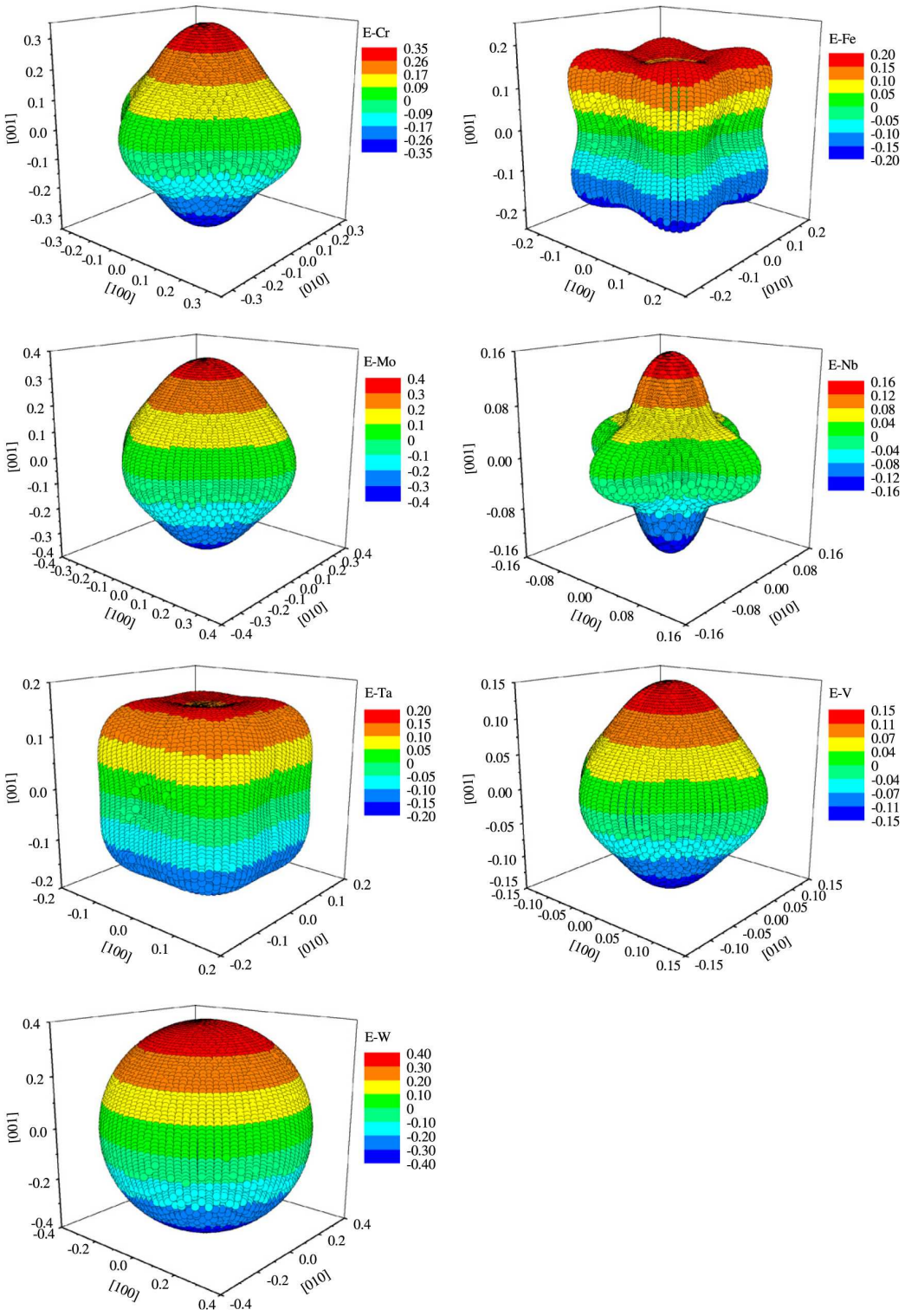

Figure 4.5: Representation surfaces of Young's modulus for BCC transition metals Cr, Fe, Mo, Nb, Ta, V and W. The length of the radius vector in the $[h\ k\ l]$ direction equals to E$(h\ k\ l)$ (in units of $10^{12}\ N/m^2$) [32].

4.3.1 Single crystal velocity surfaces and coefficients

With knowledge of the elastic moduli or the compliance of a single crystal, the velocity surface of the crystal can be determined through the Christoffel equation, and the SH coefficients of the obtained velocity surface are then calculated by expanding the surface in terms of the spherical harmonics using the equation 4.9.

Table 4.3: SH coefficients for single crystal Fe, Cu and Ni

	K_{00}	K_{20}	K_{40}	K_{60}	K_{80}	$K_{10,0}$
Fe	21303.6	0.0	-611.8	-4.2	-52.2	-2.2
Cu	17324.1	0.0	-535.5	-3.9	-46.5	-2.0
Ni	20877.2	0.0	-642.0	-4.6	-59.1	-2.7

Note that only K_{l0} are listed here, and that other non-zero, degree l coefficients are linearly dependent on K_{l0}

The SH coefficients for the single crystals of the first group of materials, including Fe, Cu and Ni, are obtained with this method using the compliance data in [32], and their K_{l0} for $l \leq 10$ are listed in Table 4.3. All the other non-zero coefficients of these degrees can also be retrieved though the relationships in Table 4.1 and 4.2.

It is evident in Table 4.3 that for this group of materials, the 2nd degree SH coefficients are enforced to be 0 by the crystal symmetries, and the amplitudes of the higher degree ones K_{ln} do not decrease monotonically with the degree l, but as two separate sets, ie the $4k$-th and the $(4k+2)$-th degrees. The 8th degree terms, for example, have an amplitude much larger than both the 6th and 10th degree terms.

Similarly, the SH coefficients for the single crystals of the other group of materials, including Al, Nb and V, can also be obtained using this method, and their K_{l0} are listed in Table 4.4. It can be seen that compared to the first group of materials, the 6th, 8th and 10th SH coefficients for this group are all very small. These differences

Table 4.4: SH coefficients for single crystal Al, V and Nb

	K_{00}	K_{20}	K_{40}	K_{60}	K_{80}	$K_{10,0}$
Al	23237.70	0.00	-122.24	-0.18	-0.63	-0.01
V	21382.30	0.00	156.73	-0.33	-2.92	0.02
Nb	18171.10	0.00	296.11	-1.42	-11.65	0.26

Note that only K_{l0} are listed here, and that there are other non-zero coefficients linearly dependent on K_{l0}

in the configurations of the SH coefficient amplitudes contribute to the completely different single crystal Young's modulus surfaces for these two group of materials, as is evident in [32].

- **The computational model and the pseudo-kernel**

In practice, ultrasonic waves are typically excited into a crystalline bulk from a transducer and received from different locations to investigate the wave velocities in various directions. In this chapter, however, I wish to establish a proof of principle for the generalised theorem as for the theorem for HCP polycrystals in Chapter 3, so that simulated velocities for a few representative experimentally obtained cubic textures will be utilized, instead of experimentally measured wave velocities, to evaluate the accuracies of forward wave speed predictions as well as to inversely extract the ODF information.

The RVE FE model established in Chapter 2 is again utilized in order to generate the simulated velocities for the analysis. As shown in Figure 2.2a, the Abaqus/Explicit model was finely-meshed to simulate the ultrasonic wave propagation in polycrystalline aggregates. There were in total 2160 grains in the model, and the elastic properties of the grains were specified to take full account of the crystallographic orientation of every grain resulting from the elastic anisotropy. By doing so a range of differing crystallographic textures could be studied, and the overall ultrasonic wave

speeds for the differing textures could be determined.

The ultrasonic waves propagating through the model were applied as pressure waves on the near-end of the model, with their amplitudes changing as sinusoidal pulses in a Hanning window, as shown by Figure 2.2b. The centre frequency of the pulses is 2MHz, which makes the wavelength about twice the size of a crystal. The centre frequency of the pulses is 2MHz, making the wavelength about twice the size of a crystal. The four lateral faces of the bar are all fixed in normal directions, enabling the waves applied on the near-end and propagating along the bar to be considered as plane waves. As the waves propagate along the model polycrystal, they pass a number of planes shown in Figure 2.2c, on which stresses and strains were tracked such that the arrival times were detected and the average wave velocities were calculated.

It needs to be stressed that as discussed in Section 4.2.2 and shown in Appendix B, the particle displacement direction can deviate significantly from the phase velocity direction along the bar. While this angular difference may be pre-calculated and compensated for single crystal simulations by carefully setting the boundary conditions, it is normally not possible for polycrystals where the particle displacement direction varies at each point along the propagation route and cannot be pre-determined. Therefore the plane wave condition does not hold any more and dispersion and dissipation come into play, resulting in smaller simulated phase velocities obtained compared to the theoretical ones.

A practical way is adopted in the following parts of the chapter to avoid this computational error affecting our studies. Whilst being aware that the actual phase velocities should be the solutions to the Christoffel equation and that the SH kernels shown in Tables 4.3 and 4.4 should be used in experimental tests, I instead use the single crystal SH coefficients obtained via the simulation model with normal boundary conditions consistent with all subsequent simulations on polycrystals as the pseudo-kernel in the generalised convolution theorem to perform both forward and inverse studies. By

virtue of the consistency of the boundary conditions, this serves as a verification of the theorem. Fe is used as the exemplary material for these demonstrations, and its pseudo-kernel coefficients to be used in all later studies are shown in contrast with the original ones in Table 4.5.

Table 4.5: Original and pseudo-kernel SH coefficients for single crystal Fe

	K_{00}	K_{20}	K_{40}	K_{60}	K_{80}	$K_{10,0}$
Original	21303.6	0.0	-611.8	-4.2	-52.2	-2.2
Pseudo	20982.2	0.0	-686.5	-6.8	73.9	-2.2

4.3.2 Theoretical orientation distributions

A single crystal satisfies our assumption of homogeneity in deduction of the generalised theorem such that when evaluating from any angles in the space, the waves always go through the same crystal, so the theorem stands in this case. Here, some simple orientations on a single crystal Fe are considered as demonstrations.

It has already been demonstrated in Section 4.2.3 that W_{lm0} with $m \geq 0$ contain all the linearly independent terms needed to reconstruct the original ODF matrices. Therefore in the following parts of the chapter, only these coefficients will be shown when referring to an ODF.

- **Single crystal with reference configuration**

The reference configuration is the simplest case for a single crystal, with the crystal system oriented exactly the same as the sample system. The ODF for this case is therefore a Dirac impulse at $\alpha = \beta = \gamma = 0$, or in fact a series of impulses at all equivalent orientations with the symmetries considered. So the ODF coefficients W_{lmn} can be then calculated accordingly by inputting all the orientations into equation 4.14.

Then to verify the generalised theorem, these W_{lmn} are input into equation 4.18 to obtain the resulting polycrystal velocity SH coefficients V_{lm}. All the calculated non-zero W_{lm0} as well as the resulting V_{lm}, both of $l \leq 10$ and $m \geq 0$, are listed in Table 4.6, and the other non-zero coefficients can be determined using the relationships listed in Table 4.2.

Table 4.6: Single Fe crystal with reference configuration

$W_{000} = 1$			
$W_{400} = 0.5833$	$W_{440} = 0.3486$		
$W_{600} = 0.125$	$W_{640} = -0.2339$		
$W_{800} = 0.5785$	$W_{840} = 0.2175$	$W_{880} = 0.3315$	
$W_{10,0,0} = 0.1693$	$W_{10,4,0} = -0.1706$	$W_{10,8,0} = -0.2030$	Kernel surface plot
$V_{00} = 20982.2$			
$V_{40} = -686.5.8$	$V_{44} = -410.2$		
$V_{60} = -6.8$	$V_{64} = 12.7$		
$V_{80} = 73.9$	$V_{84} = 27.7$	$V_{88} = 42.3$	
$V_{10,0} = -2.2$	$V_{10,4} = 2.2$	$V_{10,8} = 2.6$	Rotated surface plot

Note that only W_{lm0} are listed here, and that the other non-zero coefficients linearly dependent on W_{lm0}

For the reference configuration, the resulting velocity surface is expected to be exactly the same as the kernel, which is demonstrated in Table 4.6, with the resulting SH coefficients of the polycrystal velocity function after convolving the ODF coefficients with the kernel being exactly the same as the kernel coefficients. It is also noticeable that for this special orientation, W_{lm0} has non-zero values only when $m = 4k$.

- **Single crystal oriented with $\alpha = \pi/4$**

Now consider a single cubic crystal with an orientation rotated from the reference configuration, for example, with $\alpha = \frac{\pi}{4}$ and $\beta = \gamma = 0$. Similarly with the reference

configuration, the ODF is a series of Dirac impulses at all the equivalent orientations to $(\pi/4, 0, 0)$ given by the crystal symmetries, and the coefficients can then be calculated accordingly. The non-zero values of the W_{lmn} and the V_{lm} obtained after convolution, both of $l \leq 10$ and $m \geq 0$, are listed in Table 4.7.

Table 4.7: Single Fe crystal with $\alpha = \pi/4$

$W_{000} = 1$			
$W_{400} = 0.5833$	$W_{440} = -0.3486$		
$W_{600} = 0.125$	$W_{640} = 0.2339$		
$W_{800} = 0.5785$	$W_{840} = -0.2175$	$W_{880} = 0.3315$	
$W_{10,0,0} = 0.1693$	$W_{10,4,0} = 0.1706$	$W_{10,8,0} = -0.2030$	Kernel surface plot
$V_{00} = 20982.2$			
$V_{40} = -686.5.8$	$V_{44} = 410.2$		
$V_{60} = -6.7$	$V_{64} = -12.7$		
$V_{80} = 73.9$	$V_{84} = -27.7$	$V_{88} = 42.3$	
$V_{10,0} = -2.2$	$V_{10,4} = -2.2$	$V_{10,8} = 2.6$	Rotated surface plot

Note that only W_{lm0} are listed here, and that the other non-zero coefficients linearly dependent on W_{lm0}

With α being $\pi/4$ and β, γ both 0, the only expected difference made to the kernel is to rotate it about the Z-axis by the angle of $\pi/4$, and the figures in Table 4.7 shows exactly the same result as expected. As for the ODF coefficients, this rotated orientation only changes the signs of the W_{l40}, which results as the change of signs of the convolved velocity coefficients V_{l4}, which then eventually cause the velocity surface to be rotated about the Z-axis in the reconstruction of the surface.

- **Single crystal oriented with** $\alpha = \beta = \gamma = \pi/4$

Next, consider a slightly more complicated single cubic crystal orientation, with $\alpha = \beta = \gamma = \pi/4$. The calculation of the coefficients is still the same as the

Table 4.8: Single Fe crystal with $\alpha = \beta = \gamma = \pi/4$

$W_{000} = 1$		
$W_{400} = -0.328$	$W_{410} = 0.115 + 0.115i$	
$W_{420} = 0.115i$	$W_{430} = -0.305 + 0.305i$	
$W_{440} = 0.109$		
$W_{600} = 0.166$	$W_{610} = -0.063 - 0.063i$	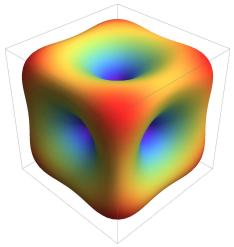
$W_{620} = 0.090i$	$W_{630} = -0.070 + 0.070i$	
$W_{640} = 0.048$	$W_{650} = -0.036 - 0.036i$	
$W_{660} = -0.134i$		
$W_{800} = 0.050$	$W_{810} = -0.103 - 0.103i$	Kernel surface plot
$W_{820} = -0.135i$	$W_{830} = 0.129 - 0.129i$	
$W_{840} = -0.225$	$W_{850} = -0.089 - 0.089i$	
$W_{860} = -0.301i$	$W_{870} = -0.114 + 0.114i$	
$W_{880} = 0.029$		
$V_{00} = 20982.2$		
$V_{40} = 386.2$	$V_{41} = -135.7 - 135.7i$	
$V_{42} = -135.7i$	$V_{43} = 359.0 - 359.0i$	
$V_{44} = -128.2$		
$V_{60} = -9.0$	$V_{61} = 3.4 + 3.4i$	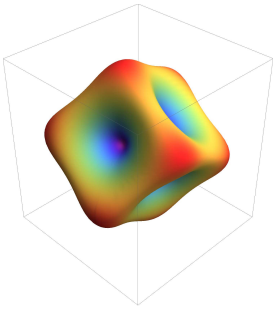
$V_{62} = -4.9i$	$V_{63} = 3.8 - 3.8i$	
$V_{64} = -2.6$	$V_{65} = 2.0 + 2.0i$	
$V_{66} = 7.2i$		
$V_{80} = -7.2$	$V_{81} = -14.8 - 14.8i$	
$V_{82} = -19.3i$	$V_{83} = 18.4 - 18.4i$	Rotated surface plot
$V_{84} = -32.2$	$V_{85} = -12.7 - 12.7i$	
$V_{86} = -43.1i$	$V_{87} = -16.3 + 16.3i$	
$V_{88} = 4.1$		

Note that only W_{lm0} are listed here, and that the other non-zero coefficients linearly dependent on W_{lm0}

previous orientations, with the ODF being impulses at all equivalent orientations to $(\pi/4, \pi/4, \pi/4)$. Some of the the non-zero coefficients W_{lmn} and V_{lm} are also listed in Table 4.8. However, only those with $l \leq 8$ are listed here for consideration of space.

For this case, the single crystal is rotated firstly about the Z-axis for $\pi/4$, then about the rotated Y'-axis for $\pi/4$, and finally about the rotated Z'' for another $\pi/4$. As a result, the (111) vector of the crystal system should be along the (001) direction in the sample system (gray box in the figures) and (001) in the crystal system along the $(1, 1, \sqrt{2})$ direction. The figures in Table 4.8 show that this rotation is done correctly with this group of W_{lmn}.

One difference of this orientation compared to the previous two, however, is that many more ODF coefficients are finite, with all W_{lm0} of $-l \leq m \leq l$ now having non-zero values, which then results in all the convolved velocity V_{lm} being non-zero.

For these respective single crystal orientations, the theorem is demonstrated to have applied correct rotations on the velocity surfaces, and the underlying SH coefficients for these cases are also calculated. It is notable that even for these single crystal orientations, which are the strongest textures possible, the 10th degree SH coefficients of V_{lm} are smaller than 2.6, which means the contributions of the ODF to V_{lm} and V_{10m} to the velocity surface are both small and negligible. Therefore in the following, focus is given only to coefficients with $l \leq 8$.

4.3.3 Studies on experimental polycrystal textures

- **Textures to be investigated**

It has been demonstrated in the previous section how to apply the rotations on single cubic crystals through equation 4.18 and therefore validated the convolution theorem; but in reality, the textures in polycrystalline aggregates are much more complex. However, provided the ODF of the texture is known, forward studies can be carried out

in a similar fashion to predict the polycrystal wave velocities using equation 4.18.

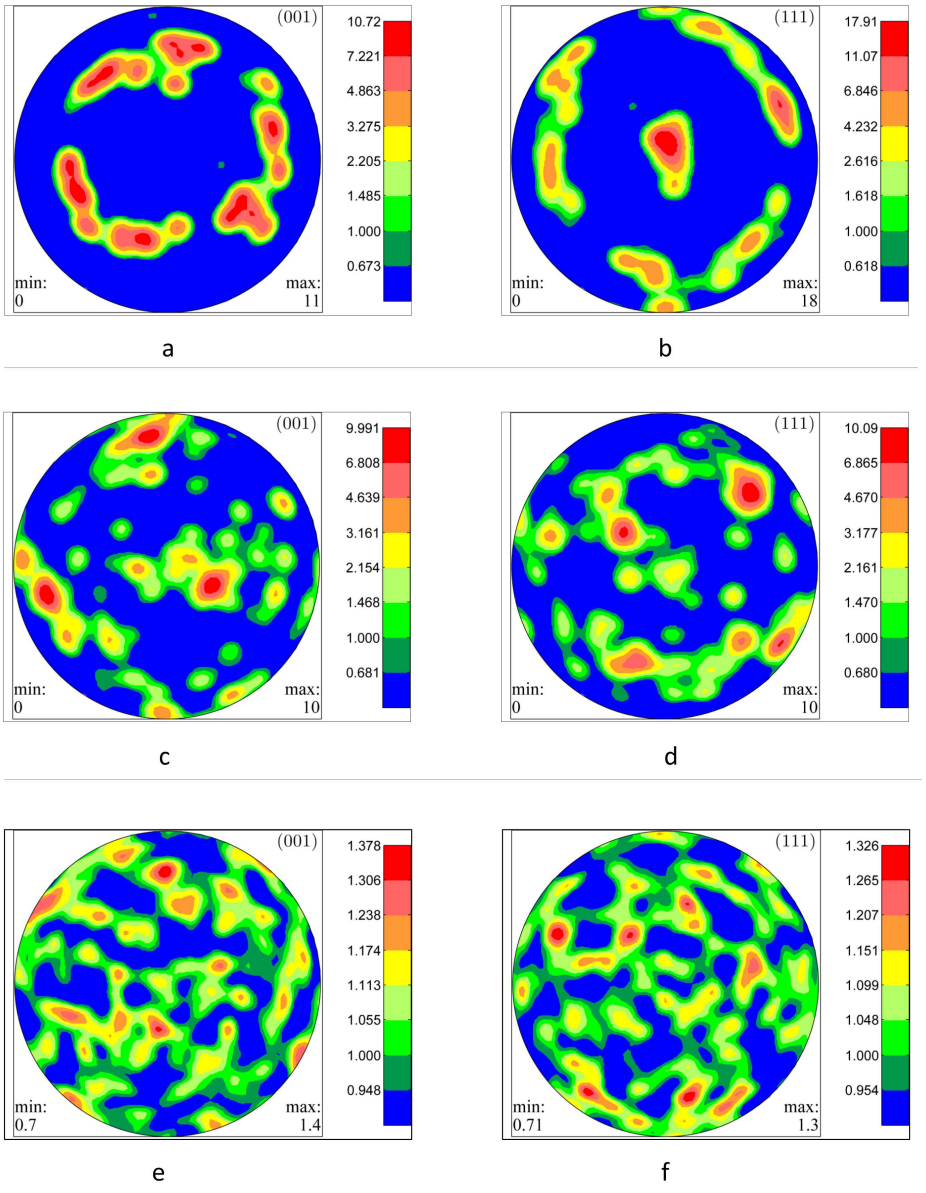

Figure 4.6: The pole figure plots of the three representative experimental cubic textures to be investigated, where a and b: the (001) and (111) pole figures of Texture-1, respectively; c and d: the plots of Texture-2; and e and f: the plots of Texture-3.

Here, the subjects of our forward studies are the three experimental representative cubic textures illustrated in Figure 4.6, with the two figures in each row showing respectively the (001) and (111) pole figure plots of the same texture. Details of the forward studies are fully demonstrated as follows: firstly, from the texture infor-

mation, the corresponding sets of ODF coefficients are determined, which are then convolved with the kernel to calculate the SH coefficients of the polycrystal velocity function; finally, these coefficients are employed by means of SH expansions to reconstruct the velocity surfaces, which are then plotted, and the polycrystal velocities in the three-dimensional space are predicted. Through the study and the results obtained, the relationship between the ODF and the polycrystalline velocities are further explored.

- **The forward study routine and results of Texture-1**

It can be seen from Figure 4.6 that the texture shown by the first row, labelled Texture-1, has the cubic crystals predominantly aligned with their (111) reciprocal vectors along the direction of the north pole, which is also the normal direction of the sample. The orientation distributions about the north pole, however, are not significantly preferred, as shown by the circle about the centre in the (001) pole figure. There are some clusters on the circle, but these are not strong.

The ODF coefficients of the texture can be readily calculated with the aid of the MTEX toolbox for Matlab [86], and the non-zero independent ones are listed in the first half of Table 4.9.

The SH coefficients of the polycrystal velocity function are then obtained through the matrix-vector multiplication described by equation 4.18 using the calculated ODF coefficients, and the results are shown in the second half of Table 4.9.

The polycrystal velocity surface band-limited up to the 8th degree can be recovered using the obtained SH coefficients:

$$v(\theta,\phi) = \sum_{l=0}^{8} \sum_{n=-l}^{l} V_{lm} Y_{lm}(\theta,\phi) \tag{4.25}$$

Table 4.9: The coefficients for the ODF and the resulting polycrystal velocity surface of Texture-1

$W_{000} = 1.0$		
$W_{400} = -0.291$		$W_{410} = -0.0771 + 0.0099i$
$W_{420} = 0.0141 + 0.0090i$		$W_{430} = 0.1034 + 0.0569i$
$W_{440} = 0.00523 + 0.00300i$		
$W_{600} = 0.127$		$W_{610} = 0.0488 - 0.0311i$
$W_{620} = 0.0351 + 0.0032i$		$W_{630} = 0.0283 + 0.0132i$
$W_{640} = 0.00784 - 0.00267i$		$W_{650} = -0.0008 + 0.0184i$
$W_{660} = 0.0228 - 0.0401i$		
$W_{800} = 0.0431$		$W_{810} = 0.0339 + 0.0195i$
$W_{820} = -0.00948 - 0.00299i$		$W_{830} = -0.0454 - 0.0312i$
$W_{840} = 0.0069 - 0.0243i$		$W_{850} = -0.0181 + 0.0462i$
$W_{860} = 0.0249 - 0.0814i$		$W_{870} = 0.0025 - 0.0441i$
$W_{880} = 0.01022 - 0.00408i$		
$V_{00} = 20982.2$		
$V_{40} = 342.3$	$V_{41} = 90.7 - 11.7i$	$V_{42} = -16.6 - 10.6i$
$V_{43} = -121.7 - 67.i$	$V_{44} = -6.2 - 3.5i$	
$V_{60} = -6.9$	$V_{61} = -2.6 + 1.7i$	$V_{62} = -1.9 - 0.2i$
$V_{63} = -1.5 - 0.7i$	$V_{64} = -0.4 + 0.1i$	$V_{65} = 0. - 1.i$
$V_{66} = -1.2 + 2.2i$		
$V_{80} = 6.2$	$V_{81} = 4.9 + 2.8i$	$V_{82} = -1.4 - 0.4i$
$V_{83} = -6.5 - 4.5i$	$V_{84} = 1. - 3.5i$	$V_{85} = -2.6 + 6.6i$
$V_{86} = 3.6 - 11.7i$	$V_{87} = 0.4 - 6.3i$	$V_{88} = 1.5 - 0.6i$

Note that only W_{lm0} are listed here, and that the other non-zero coefficients linearly dependent on W_{lm0}

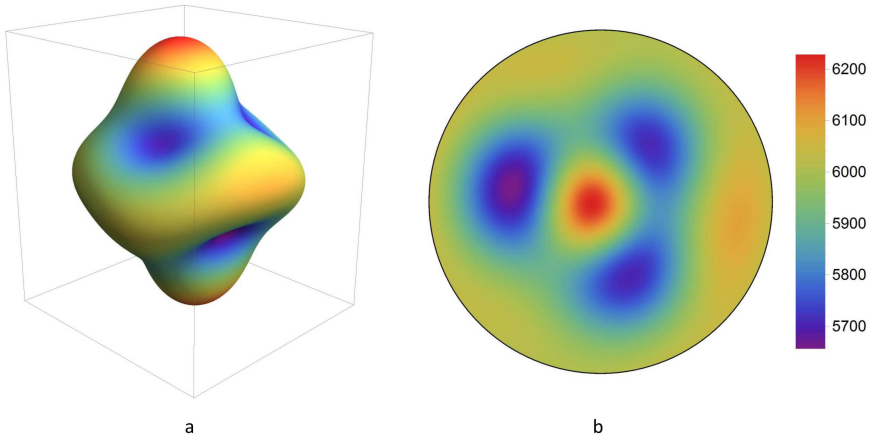

Figure 4.7: The polycrystal velocity surface of Texture-1, shown as: a. three-dimensional shape; b. the stereographic projection of the upper part onto the equator.

The reconstructed velocity surface for Texture-1 is plotted in Figure 4.7, with Figure 4.7a illustrating the velocity variations as three-dimensional shape changes and Figure 4.7b showing the stereographic projection of its upper half onto the equator in a similar way as for pole figures. It can be seen that because of the preferred (111) pole distributions along the north pole and the fact that the (111) direction has the largest wave speed within a single crystal, the polycrystal velocities are also the largest near the north pole; and because the (111) poles on the peripheries of the figure are evenly distributed, the velocities near the equator also display very close amplitudes. The blue regions in the middle of Figure 4.7b are resulting from the (001) pole distributions because the single crystal velocities along this pole are the smallest.

- **Results of the other two textures**

The other two textures are studied using the same method. As for the previous texture, Texture-2 is also strongly textured according to the intensities of its pole figures in the second row of Figure 4.6. The red spots in its (001) pole figure, as well the

four preferred orientations in the (111) pole figure, suggest that the texture is in loose approximation with a rotated single crystal.

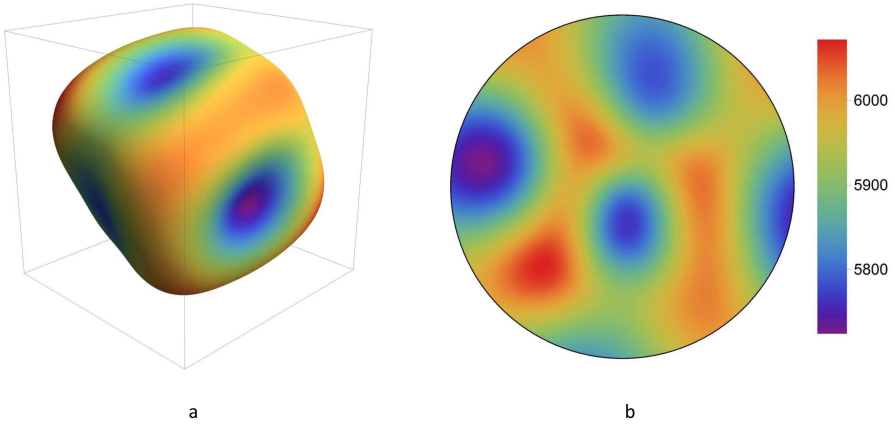

Figure 4.8: The polycrystal velocity surface of Texture-2, shown as: a. three-dimensional shape; b. the stereographic projection of the upper part onto the equator.

Similarly, the ODF coefficients are output and polycrystal velocity coefficients are calculated. But here, only the latter are shown for space reasons. The values for Texture-2 are listed in Table 4.10, and the reconstructed velocity surface is also plotted in two ways in Figure 4.8.

Figure 4.8a shows that the polycrystal velocity surface of Texture-2 is indeed approximately in the shape of a distorted and rotated cube, which agrees with the information from the pole figures.

The last texture, labelled Texture-3 and shown by the last row of pole figures in Figure 4.6, has near theoretically random orientation distributions and therefore almost uniform intensities in all the pole figures, suggesting that the texture may be from a powder-metallurgy sample. The resulting SH coefficients of the polycrystal velocity surface are similarly calculated and listed in Table 4.11, and the surface itself is plotted in Figure 4.9.

Theoretically, a polycrystal aggregate with random texture should be elastically

Table 4.10: The polycrystal velocity SH coefficients calculated from the ODF of Texture-2

$V_{00} = 20982.2$			
$V_{40} = -72.1$	$V_{41} = 35.1 + 98.7i$	$V_{42} = 67.8 + 7.5i$	$V_{43} = -80.4 - 26.9i$
$V_{44} = -90.6 - 65.9i$			
$V_{60} = -2.6$	$V_{61} = -0.1 + 0.2i$	$V_{62} = 1.4 - 1.7i$	$V_{63} = 0.6 - 1.3i$
$V_{64} = 1.1 - 0.1i$	$V_{65} = 0.1 - 1.4i$	$V_{66} = -0.7 - 0.5i$	
$V_{80} = -4.6$	$V_{81} = -1.6$	$V_{82} = -5.1 + 0.5i$	$V_{83} = 3.6 - 1.i$
$V_{84} = -0.3 - 5.1i$	$V_{85} = 0.4 - 2.1i$	$V_{86} = -0.2$	$V_{87} = 4.3 + 2.7i$
$V_{88} = 1.1 + 1.1i$			

isotropic, so the wave velocities should be approximately the same regardless of the incident direction. It is shown in Figure 4.9a that the velocity surface is indeed close to a sphere, and the largest difference in velocity amplitudes is no more than 20 m/s, as shown by Figure 4.9b.

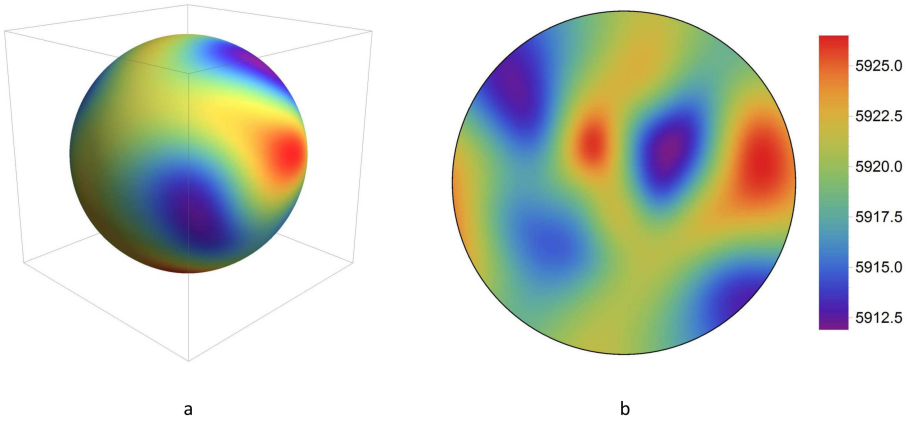

Figure 4.9: The polycrystal velocity surface of Texture-3, shown as: a. three-dimensional shape; b. the stereographic projection of the upper part onto the equator.

So far forward studies have been successfully performed on the three experimental

Table 4.11: The polycrystal velocity SH coefficients calculated from the ODF of Texture-3

$V_{00} = 20982.2$			
$V_{40} = 0.9$	$V_{41} = 4.6 - 0.3i$	$V_{42} = -2.1 + 4.6i$	$V_{43} = -1.2 - 0.9i$
$V_{44} = 3.9 - 0.4i$			
$V_{60} = 0.$	$V_{61} = 0.1$	$V_{62} = 0.$	$V_{63} = -0.1$
$V_{64} = 0.$	$V_{65} = -0.1 + 0.1i$	$V_{66} = 0. - 0.1i$	
$V_{80} = 0.1$	$V_{81} = 0. - 0.2i$	$V_{82} = -0.3 - 0.1i$	$V_{83} = -0.4 + 0.7i$
$V_{84} = -0.2 - 0.1i$	$V_{85} = 0.1 - 0.4i$	$V_{86} = 0.1 - 0.1i$	$V_{87} = 0.3 + 0.3i$
$V_{88} = -0.2 + 0.4i$			

textures and reconstructed the polycrystal velocity surface, which all qualitatively agree with the pole figures. These results will be compared to independent simulation results in following sections to show quantitatively the correctness and accuracy of the generalised convolution theorem.

4.3.4 Discussions of the forward studies

The forward studies on theoretical distributions and experimental textures have revealed the following properties about the ODF and velocity surfaces themselves and the relationships between them.

First, for general cases (eg the single crystal orientation with $\alpha = \beta = \gamma = \pi/4$ or indeed all the experiential textures), many terms of the ODF and the velocity surface coefficients are complex numbers, and omitting the imaginary parts [74, 78] leads to errors in both the amplitudes and phases in the ODF and reconstructed velocity surfaces.

Secondly, for the material Fe, the polycrystal velocity SH coefficients V_{lm} of the degrees 6∼10 are all less than 10 for all the experimental textures, even though two

of them are strongly textured. This is because the ODF coefficients W_{lmn} of the corresponding degrees are very small (partly resulting from the $1/(2l+1)$ term in equation 4.20), so despite that the 8th degree coefficient of the kernel K_{80} has relatively large amplitude, the resulting V_{lm} after convolving the kernel with the ODF are still small. This means that when reconstructing the polycrystal velocity surfaces, the contributions from V_{lm} of 6∼10th degrees to the overall velocities are no more than 10 m/s respectively, which are in the same order with the experimental errors of ultrasonic tests and hence can be neglected. As the V_{lm} are obtained through the convolution process, these contributions are in fact from the ODF coefficients of these degrees.

This leads to two more important implications: first, it demonstrates that the ultrasonic wave velocities in these cubic materials only have strong dependence on the 4th degree ODF coefficients, and the contributions from the higher degree coefficients are relatively weak and of negligible amplitudes of less than 10. So when performing the forward studies to predict the polycrystal velocities, the theoretical accuracy of approximately ±20 m/s can be achieved by using the coefficients up to the 4th degree only. Second and more importantly, it is therefore not possible to retrieve the ODF coefficients of 6th degree or higher using ultrasonic wave tests, because accurate results of the velocity coefficients V_{lm} are required in order to retrieve these ODF coefficients, which is not possible to achieve as their amplitudes are in the same order with experimental errors.

It also should be noted that even though the above conclusions are based on the elastic properties of the metal Fe, it applies to the group of materials with similar single crystal velocity surfaces with Fe, including Cu, Ni, etc; it also applies for the other group of materials including Al, Nb, V, etc, whose 6th, 8th and higher degree single crystal SH coefficients are even smaller compared to Fe, which results in even less contributions to the polycrystal velocities from the ODF coefficients of these degrees.

SECTION. 4.4

Inverse studies: from wave velocities to the ODF

The generalised spherical convolution theorem has been employed in the previous section in forward studies to predict velocities from the texture information for both theoretical and experimental orientation distributions. In this section, it is to be used in the inverse sense to extract texture information from ultrasonic wave velocities, ie, to perform inverse studies.

4.4.1 The Gaussian-Legendre quadrature scheme to obtain V_{lm}

The direct objective of the inverse studies is the determination of the ODF coefficients, which would ultimately enable us to reconstruct the original ODF through the convolution expansion theory. As shown by the generalised theorem in equation 4.18, the ODF is convolved with the single crystal wave velocity to make the polycrystal velocity function and therefore may be obtained by de-convolving the kernel from the polycrystal velocities. In other words, in order to extract the texture information from ultrasonic tests, the first step is to establish the polycrystal velocity coefficients V_{lm} from the velocity results.

The calculation of the coefficients V_{lm} from a set of discrete values via numerical integration method was presented in Chapter 3 where comparisons of the two most widely used quadrature, namely equiangular and Gaussian-Legendre, were also presented. In this chapter the latter quadrature is again chosen for its ability to get to $(2N-1)$th degree of accuracy with only $2N \times N$ discrete data. The numerical integration is written:

$$V_{lm} = \frac{\pi}{N} \sum_{j=0}^{2N-1} \sum_{i=0}^{N-1} v(\theta_i, \phi_j) Y_{lm}^*(\theta_i, \phi_j) \omega_N(i) \tag{4.26}$$

where θ_i is the ith Gaussian node for the polar angle, ϕ_j is equal to $(j-1)\cdot\pi/N$ to ensure the azimuthal angle goes equally spaced from 0 to 2π, and $\omega_N(i)$ is the well-known weight function for the ith Gaussian node.

The same technique described in Chapter 3 is used here to generate the velocity at the particular nodes $v(\theta_i, \phi_j)$ using the RVE model. Instead of rotating the ultrasonic wave incident directions, it is the crystallographic orientations of all crystals in the model that are rotated systematically and correspondingly, with both the polycrystal model and the wave propagation direction fixed. Here evaluating the wave velocity in various different directions (θ_i, ϕ_j) with respect to the sample system o-xyz is equivalent to always evaluating the velocity in a fixed direction but with the sample system rotated by $(-\theta_i, -\phi_j)$.The rotation of the sample system then causes the configurations of all the crystals in the model to undergo the same additional rotation, which may be calculated by left-multiplying the following rotation matrix shown in equation 3.35.

The 4th degree of accuracy is desired in our studies, so theoretically at least 10×5 discrete data are needed for the Gaussian-Legendre quadrature. In the following parts N is chosen to be 10 to achieve both accuracy and efficiency.

4.4.2 Simulated wave velocity surfaces & retrieved ODF coefficients

The three experimental textures in Figure 4.6 are all input to the RVE model and rotated to the corresponding configurations, taking full account of their crystallographic orientations and the additional rotation introduced by the Gaussian-Legendre quadrature scheme, as shown by equation 4.6. The computational results are then used to calculate the SH coefficients V_{lm} of the polycrystal velocity function through equation 4.26, and the resulting V_{lm} may be used in two ways: on one hand, they can be utilized to reconstruct the velocity surfaces, which, when compared with the velocity surfaces predicted by the generalised convolution theorem in Section 4.3, enable us

to verify the accuracy of the theorem in the forward studies; on the other hand, the ODF information contained in the calculated V_{lm} may be obtained by de-convolving the SH coefficients of single crystal velocity function out from the V_{lm}.

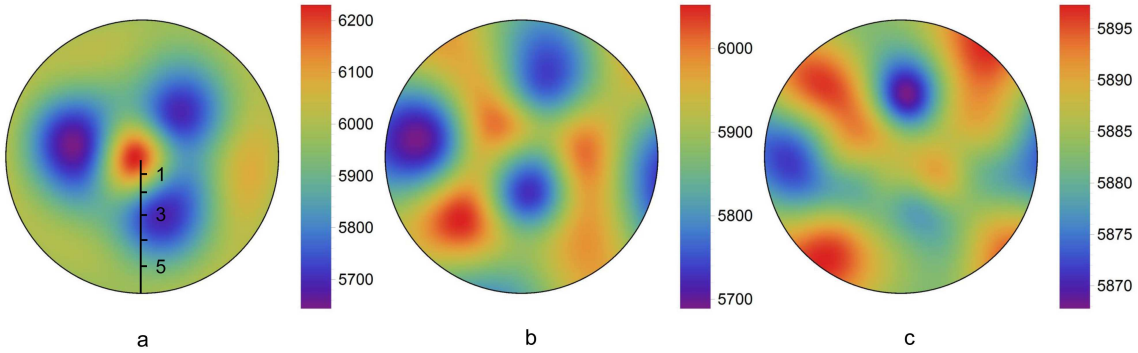

Figure 4.10: The stereographic projections of the polycrystal velocity surfaces obtained via the simulation method, with a, b, c corresponding respectively to Texture-1, 2, 3. Note that the different appearance of plot c with Figure 4.9b results from their fine colourscales and that the near-isotropy in wave speed for Texture-3 is well reflected in both plots.

The reconstructed polycrystal velocity surfaces from the V_{lm} are plotted in Figure 4.10, with a, b, c corresponding to the simulation results of Texture-1, 2, 3 in Figure 4.6, respectively. It can be seen that for Texture-1 and 2 whose textures are strongly preferred and elastic anisotropies are pronounced, the results agree very well with the predictions of the theorem in Figures 4.7 and 4.8. However, for Texture-3 whose orientation distribution is almost random, the contour results seem rather different to the predictions in Figure 4.9. This is because the random texture results in very small differences in the polycrystal spatial velocities (about 10m/s in this case), which are the same level as the errors of the simulation model(and of the ultrasonic wave experiment techniques too), so that the model velocity differences are difficult to extract. Nevertheless, the simulation results do capture the most important characteristic of the velocity surface for the random texture; that is, velocities are almost the same regardless of the incident direction, with largest difference less than 20m/s.

It is also noticeable that for the Texture-3, even though both the simulation results

Table 4.12: Comparison between the predicted and simulated velocities of Texture-1 at 5 Gaussian nodes

Gaussian nodes$(\theta_i, 0)$	i=1	i=2	i=3	i=4	i=5
Predicted (m/s)	6074.3	5868.5	5854.5	6013.2	6088.7
Simulation (m/s)	6044.3	5849.7	5845.3	5990.1	6065.0

and the predictions display no significant velocity changes with direction, the amplitudes of the former are smaller compared to the latter. Indeed, this is also the case for Texture-1 and 2 as well. Take the two sets of results at the five Gaussian nodes in Figure 4.10a for example, as listed in Table 4.12, the simulation results are also smaller than the predicted values. This phenomenon has been discussed in the previous chapter and can be explained in the same way: in the generalised theorem there are no inter-grain effects taken into consideration, and grains are treated as arrays of crystals. However, in the simulation model or experimental practice, neighbouring grains always have interactions on each other such that, when the waves propagates through neighbouring grains with different velocities, local stress fields are generated which eventually slow the waves down. Or in other words, the crystals in polycrystalline aggregates do not exhibit exactly the same properties as the theoretical kernel due to the confinement from neighbouring grains. In addition, because the elastic anisotropy of Fe is known to be more pronounced than Ti, the differences between the two sets of velocities for Fe are a little larger than those of Ti.

I now move on to the inverse problem to perform the deconvolution on V_{lm} and to extract the ODF coefficients. According to the relationships of W_{4mn} listed in Table 4.2 and similarly of K_{4n}, the coefficients W_{4m0} can be calculated via:

$$W_{4m0} = \frac{V_{lm}}{(1 + 2 \times 0.59761430^2)K_{40}}, \text{where} - l \leq m \leq l. \tag{4.27}$$

Table 4.13: The original and recovered (Recovrd) 4th degree ODF coefficients of the three textures(Tex-1,2,3) illustrated in Figure 4.6

Tex-1	Original	$W_{400} = -0.291$	$W_{410} = -0.0771 + 0.0099i$
		$W_{420} = 0.0141 + 0.0090i$	$W_{430} = 0.1034 + 0.0569i$
		$W_{440} = 0.00523 + 0.00300i$	
	Recovrd	$W_{400} = -0.278$	$W_{410} = -0.0696 + 0.0035i$
		$W_{420} = 0.0145 + 0.0079i$	$W_{430} = 0.1137 + 0.0587i$
		$W_{440} = -0.00053 + 0.00415i$	
Tex-2	Original	$W_{400} = 0.0613$	$W_{410} = -0.0298 - 0.0839i$
		$W_{420} = -0.0576 - 0.0064i$	$W_{430} = 0.0683 + 0.0228i$
		$W_{440} = 0.0770 + 0.0560i$	
	Recovrd	$W_{400} = 0.0476$	$W_{410} = -0.0356 - 0.0871i$
		$W_{420} = -0.0561 - 0.0014i$	$W_{430} = 0.0825 + 0.0201i$
		$W_{440} = 0.0744 + 0.0557i$	
Tex-3	Original	$W_{400} = -0.000769$	$W_{410} = -0.00395 + 0.00024i$
		$W_{420} = 0.00180 - 0.00387i$	$W_{430} = 0.001042 + 0.000731i$
		$W_{440} = -0.00333 + 0.00030i$	
	Recovrd	$W_{400} = -0.00424$	$W_{410} = -0.000195 + 0.000608i$
		$W_{420} = -0.00579 - 0.00294i$	$W_{430} = 0.00350 - 0.00515i$
		$W_{440} = 0.00749 - 0.00186i$	

It has been mentioned that $W_{4\bar{m}0}$ andW_{4m0} are complex conjugates to each other, hence only W_{4m0} with $m \geq 0$, which are the only linearly independent coefficients, are listed in Table 4.13. It can be seen that for these textures, all the coefficients of the 4th degree including W_{410} and W_{430} are recovered. For Texture-1 and 2, the coefficients obtained via simulated velocities are of good accuracy compared to the original ones, with both the real and imaginary parts well retrieved; but the results of Texture-3 is less good. This results from the previously discussed issue of V_{lm} being very small and beyond the accuracy of the simulation model. It is also directly

related with the ODF, as shown by Table 4.13, the original ODF coefficients of the random texture are one or two orders smaller than the other two textures. This simply reflects that Texture-3 is, to all interests and purposes, random, and the small deviations from randomness cannot be nor need to be actually quantified.

4.4.3 Recovering the ODF & discussions

The recovered 4th degree coefficients can be utilized to represent texture. The band-limited ODFs to the 4th degree are reconstructed via equation 4.13 using the coefficients listed in Table 4.13. The pole figures for the reconstructed ODFs are shown in Figure 4.11, and in order to provide direct comparison with the originals from which the velocity profiles were determined, we again plot the them in Figure 4.12, and the following conclusions are drawn from this comparison:

First, it is evident that for the first two textures, the contours in both the (001) and (111) pole figures of the recovered plots capture the hot spots of the original distributions well. The preferred orientations of (111) in the centre for Texture-1 and the three hot spots of the (001) distribution for Texture-2 are both clearly recognizable. For Texture-3, even though the contours of the recovered pole figures appear to be different from the original distributions, in fact the random texture is captured and the pole distribution densities should be near uniform for all poles which is well reflected in terms of the distribution of intensities. Therefore, the (001) and (111) pole figures recovered from wave velocities are demonstrated to provide good quality information about the original ODF.

It is observed that the smallest values in some of the reconstructed plots are negative. This results for two reasons: firstly, the simulated velocities used to determine the ODF coefficients inversely are different from theoretical values, as compared in Section 5.3, hence errors are introduced (because of grain interaction etc); and secondly, the truncation degree of 4 means the expansion is not a perfect approximation to the

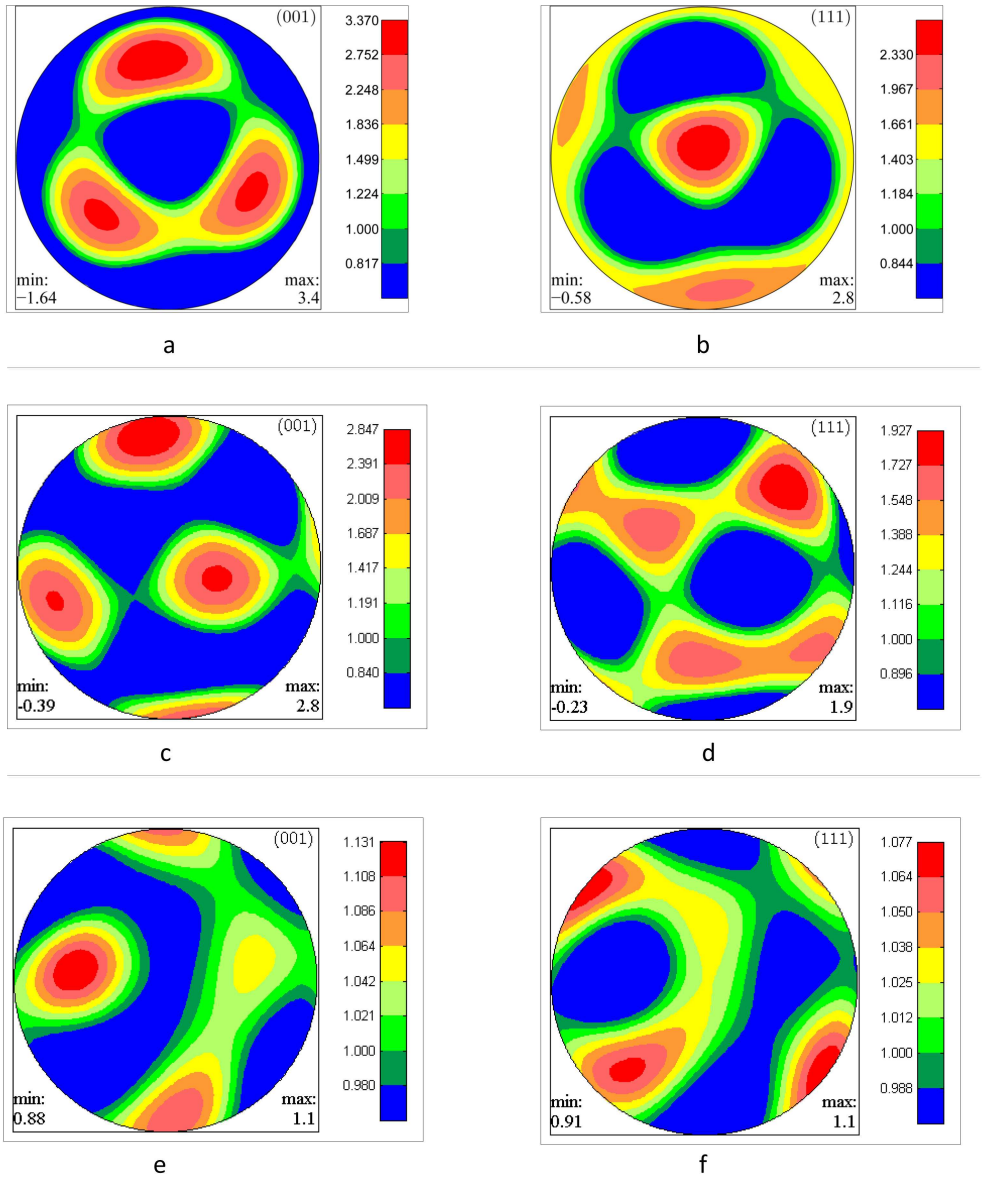

Figure 4.11: The pole figures of the three ODFs retrieved from wave velocities, where a and b: the (001) and (111) pole figures of Texture-1, respectively; c and d: plots of Texture-2; and e and f: plots of Texture-3.

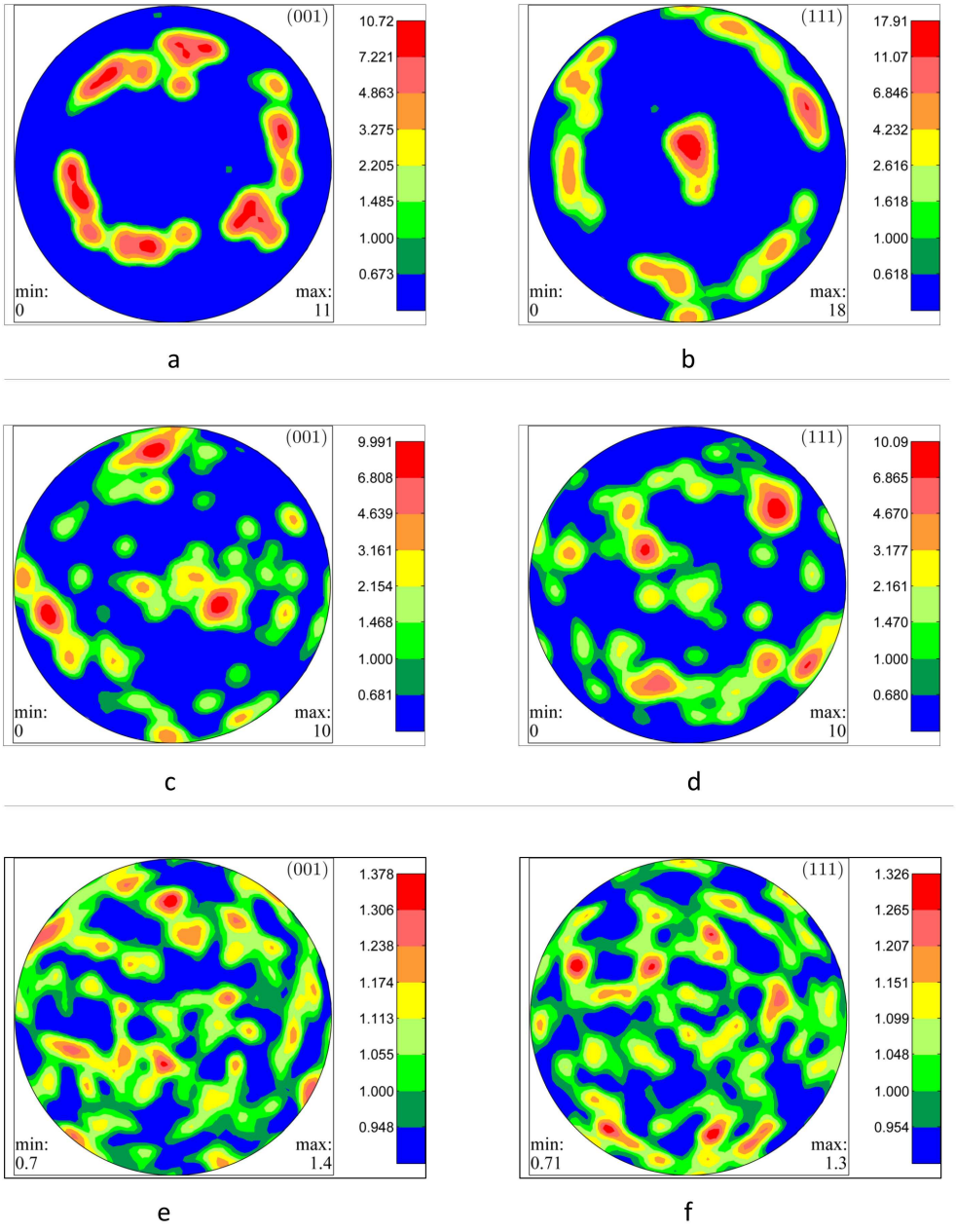

Figure 4.12: The original pole figure plots of the three representative experimental cubic textures to be investigated, where a and b: the (001) and (111) pole figures of Texture-1, respectively; c and d: the plots of Texture-2; and e and f: the plots of Texture-3.

original function, so localized deviations may occur. Moreover, the truncation errors are also responsible for the greatly reduced intensities at the preferred orientations in the reconstructed pole figures for the first two original textures with strongly preferred orientations. According to Roe [39], the error can be quantitatively calculated via:

$$\delta_w = \sum_{l=6}^{\infty} \sum_{m=-l}^{l} \sum_{n=-l}^{l} W_{lmn} W_{lmn}^* \tag{4.28}$$

and the error is likely to be quite large. However, even for the truncated ODF, random texture and single crystal orientations are still the two extreme cases which would set up the lower and upper bounds for the amplitudes, and it is possible that the values obtained with these extremes also truncated at 4th degree would enable us to re-scale the intensities of the recovered ODFs to comparable values to the originals.

SECTION. 4.5

Conclusions

In this chapter, the spherical harmonic convolution theorem obtained specifically for HCP materials in Chapter 3 has been expanded into a generalised form which applies for all types of crystal structures. It has been shown again that the ODF of a polycrystalline aggregate convolves with the single crystal wave velocity function to give the polycrystal velocity function.

When applying the generalised theorem for forward studies, the polycrystal velocity function for any crystal type can be predicted with knowledge of the ODF and the kernel. Representative studies have been performed on the cubic metal Fe, with both theoretical orientations and experimental textures, and satisfactory predictions of the polycrystal velocities are obtained.

When applying the generalised theorem for inverse studies, however, it is shown that only for HCP and cubic structure can the ODF be obtained from polycrystal velocities. In the studies on the Fe kernel convolving with experimental textures, the reason for the fact that it is often not possible to recover ODF coefficients with 6th degrees or higher through ultrasonic tests has also been demonstrated. Further, proof of principle of the inverse technique has been established using simulated velocities from representative experimental textures, and the 4th degree ODF coefficients have been well recovered.

5

Conclusions and Future Plans

SECTION. 5.1

Conclusions of The Thesis

Systematic studies have been carried out on ultrasonic wave propagations in polycrystalline HCP and cubic materials with presences of crystallographic textures, and both forward studies (where texture is known for the predictions of ultrasonic wave speed) and inverse studies (where the wave speed is known for the inverse determination of texture) are demonstrated for the ultimate purpose of developing a non-destructive, bulk 3D texture determination technique for HCP and cubic materials using ultrasounds.

Chapter 2 reviewed the feasibility of the development by performing forward studies, both computationally and experimentally, on HCP polycrystalline aggregates and evaluating the speed differences introduced by texture. In the computational part of the study, a finite element Representative Volume Element (RVE) methodology, which is able to accommodate up to 2160 crystals with arbitrary orientations, was employed to investigate the ultrasonic response of a range of differing textures, and it was demonstrated that the changes in texture (including the incorporation of a macro-zone) easily generated measurable differences in wave speed. In the experimental part, two Ti-6Al-4V samples with differing rolling histories were characterized

by EBSD and examined using ultrasonic scanning to determine wave speed for each sample. The texture information from EBSD was incorporated into the RVE model to predict the speeds, and the computed and experimental ultrasound speeds were in good agreement, with both indicating the existence of clear velocity profiles for the two samples, which enabled the textures to be differentiated using ultrasound, and proved the feasibility for the development of the ultrasound technique for texture measurements.

A solution to the inverse problem for HCP materials was provided in Chapter 3 as a new convolution approach which coupled single crystal wave velocity (the kernel function) with the orientation distribution function to give the polycrystal velocity response. The convolution relationship became simple point-wise multiplications when the three functions were expressed by means of spherical harmonics and could be solved to achieve any one of the three functions when the other two were known. In the forward problem, the polycrystal wave speed for a range of nine representative HCP textures predicted by the convolution technique was shown to have perfect sensitivity to texture and quantitatively good agreement with the computed one. As for the inverse problem, the technique allowed for de-convolution to be carried out so that texture information could be extracted with knowledge of the single crystal and the polycrystal wave speed response. Proof of principle was established for this inverse process of texture determination for HCP materials by obtaining excellent texture results from a series of computational wave velocities generated via the RVE model.

In Chapter 4 the convolution theorem obtained specifically for HCP materials in Chapter 3 was expanded into a generalised form with considerations of all three Euler angles in the description of crystallographic orientations. It has been shown again that the ODF of a polycrystalline aggregate convolves with the single crystal wave velocity function to give the polycrystal velocity function. Similarly with Chapter 3,

the generalised theorem was first applied for forward studies, where the polycrystal velocity function for any crystal type can be predicted with knowledge of the ODF and the kernel. The cubic metal Fe was used as the exemplary material and satisfactory predictions of the polycrystal velocities are obtained. For inverse studies, however, it was demonstrated that only for HCP and cubic structure could the ODF be obtained from polycrystal velocities, and that even though the solution to inverse problem for cubic materials was given by the generalised theorem, it was often not possible to recover ODF coefficients with 6th degrees or higher through ultrasonic tests. Further, proof of principle of the inverse process was also established in the same manner as Chapter 3.

The major finding of the thesis, therefore, is twofold. Firstly, it has been proved and demonstrated that the differing textures in polycrystalline aggregates would cause significant differences in ultrasonic wave velocities, which can well be detected by state-of-the-art experimental instruments, so it is entirely possible for ultrasound to be used for texture detections; more importantly, a theorem has been constructed for both HCP and cubic materials which can be used to determine all low-degree ODF coefficients (up to the 4th degree), with both the real and imaginary parts recovered, solely from ultrasonic wave speed. Proof of principle has been established of these materials as well, with the obtained ODF coefficients and pole figures in excellent agreement with original ones.

SECTION. 5.2

Future plans

- **Experimental validation of the theories**

Proof of principle has been established for the applications of the spherical convolution theorem on both HCP and cubic materials in Chapter 3 and 4, where the texture information was extracted solely from their angular variations of ultrasonic wave speed for a range of differing textures. In those demonstrations, however, computational wave speeds generated by the RVE model with texture inputs were used instead of experimentally obtained wave speeds. In order for the technique to hopefully get a wide application, experimental verifications are an essential step to start with, and this is the first thing to do in my future plans.

It was revealed in Sections 3.4 and 4.4 that the core problem in the inverse study processes for both HCP and cubics is to obtain the SH coefficients V_{lm} of the polycrystal wave velocity function $v(\theta, \phi)$, and it can be calculated by means of numerical integration with the Gaussian-Legendre quadrature via:

$$V_{lm} = \frac{1}{2N} \sum_{j=0}^{2N-1} \sum_{i=0}^{N-1} v(\theta_i, \phi_j) Y_{lm}^*(\theta_i, \phi_j) \omega_N(i), \tag{5.1}$$

where $\omega_N(i)$ is the well-known weight function for the ith Gaussian node. So the problem has in fact become how the wave velocities can be obtained at the given Gaussian nodes $v(\theta_i, \phi_j)$. There are at least two ways to do it.

The first way is to use the clever apparatus which was devised by Rokhlin and Wang [103] for phase velocity measurements on composite plates, but nevertheless has wider applications on indeed plates made of any generally anisotropic materials. The set-up of the apparatus is sketched in Figure 5.1, and it is based on the fact that when an ultrasonic wave travels from the coupling medium (eg water) through the

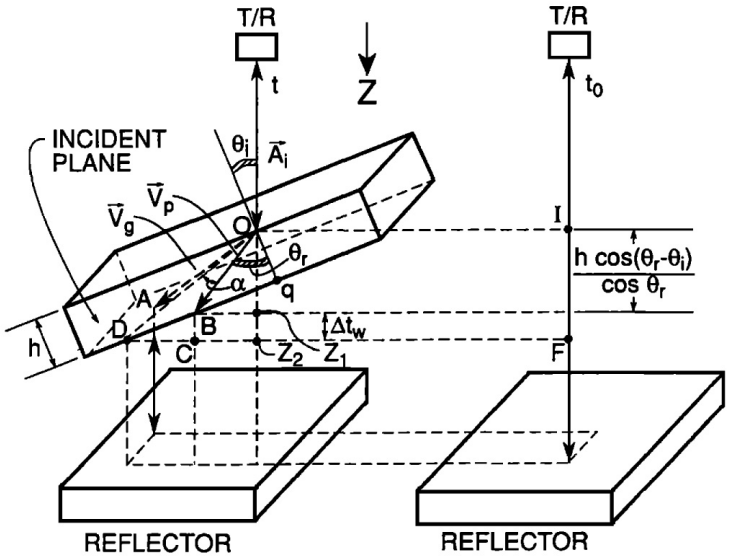

Figure 5.1: Schematic of the double through-transmission apparatus devised by Rokhlin and Wang [103].

sample, refraction happens at the upper and lower interfaces and quasi-longitudinal group velocity v_g and phase velocity v_p deviate from each other from the upper interface onwards; however, it could be mathematically proved that the time t_g it takes the wave energy propagating at the speed of v_g to reach the reflector is the same as t_p it takes the wave energy propagating at v_p, and when reflected by the reflector, the two groups of energy return along the same routes with their respective incident routes. If the difference between t_p and the time it takes the wave to travel the same vertical distance through the coupling medium only (the configuration shown by the right figure in Figure 5.1) is denoted as Δt, the thickness of the sample as h and the wave velocity in the coupling medium as v_0, then the phase velocity in the direction with refraction angle θ_r is calculated by:

$$v_p(\theta_i) = (\frac{1}{v_0^2} - \frac{\Delta t \cos\theta_i}{h v_0} + \frac{\Delta t^2}{4h^2})^{-1/2} \tag{5.2}$$

The second method is to make use of the ultrasonic phased array technology. Unlike the conventional transducers which have only a single piezoelectric element for generating and receiving wave signals, a phased array is made of a number of such elements arranged in linear (1D arrays), planar (2D arrays) or circular patterns [100]. One advantage of the phased array technology is that the movement of a single element transducer (eg a linear scan) can be simulated by simply scanning a fixed width aperture over the length of the array, enabling rapid scanning process and full B-scan map capture; the other advantage is that all the existing conventional inspection modalities requiring multiple single element probes can be done simultaneously by an array, and by using advanced signal capture techniques such as Full Matrix Capture (FMC), arrays can achieve new inspections that would have been impossible for conventional transducers [104].

A linear array normally has two working modes for the measurements of ultrasonic *group* velocity of the quasi-longitudinal wave (as it has higher velocity over shear waves thus can be captured by first arrival method), the Backwall Reflection Method (BRM) and Through-Transmission Method (TTM), as shown respectively by Figure 5.2a and b [104]. The sample for both modes needs to be flat, with front and back surfaces parallel with each other for accurate calculation of wave velocities. For the BRM mode in Figure 5.2a, the wave generated by the ith element and propagating at the *group* velocity v_g is reflected by the backwall ultimately received by the jth element, hence $v_g = 2d/(\cos\theta_i \cdot \Delta t)$ and $\theta_i = \theta_j = \arctan(|x_j - x_i|/2d)$; similarly for the TTM mode, the group velocity v_g and the angle θ_i are $v_g = d/(\cos\theta_i \cdot \Delta t)$ and $\theta_i = \theta_j = \arctan(|x_j - x_i|/d)$. It should be noted that the measurement results from these tests are the *group* velocities, whereas in our convolution theorem, the phase velocities are needed for the inverse studies. It has been shown though, that these two velocities overlap on the symmetry planes for transversely isotropic material [105] (which HCP belongs to) and can be extended to generally anisotropic materials [106].

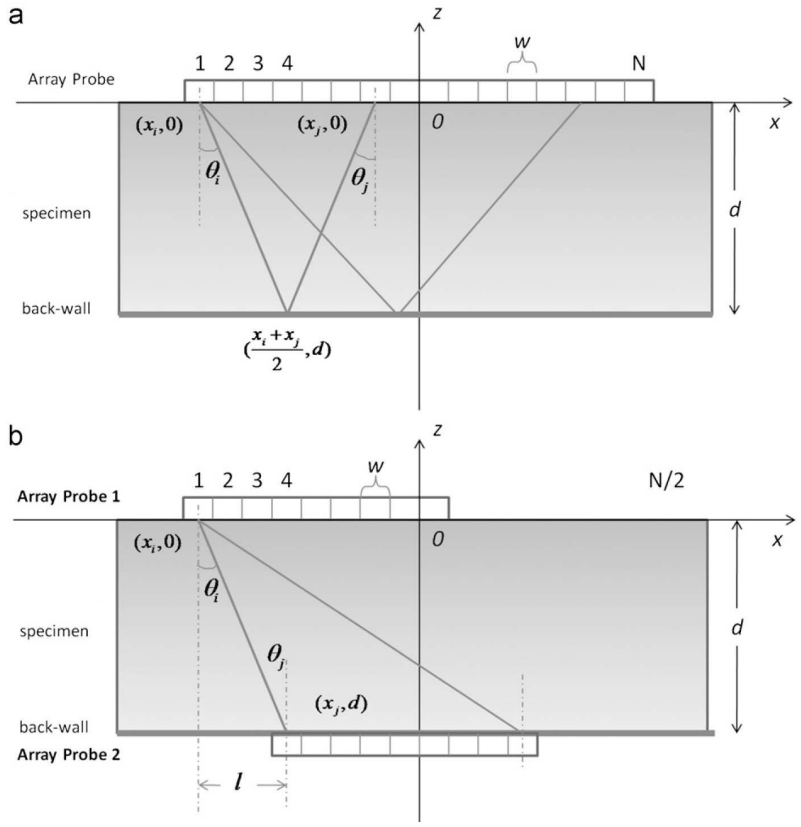

Figure 5.2: Schematic of the Backwall Reflection Method (BRM) and Through-Transmission Method (TTM) modes for the measurement of ultrasonic *group* velocities [104].

This issue needs to be handled with extra care in experiments.

Section 3.4 and 4.4 have demonstrated that our aims for both HCP and cubic materials in ultrasonic experiments are to obtain up to 6th degree SH coefficients V_{lm} of the polycrystal wave speed, so the value of N in equation 5.1 is equal to 6, which means $v(\theta_i, \phi_j)$ at 6 Gaussian nodes of the polar angles θ_i for each of 12 azimuthal angles ϕ_j are needed. As illustrated in Figure 5.3a, one placement of the phased array can be used for the detection of various polar angles at the same azimuthal angle ϕ (here two cases of ϕ_0 and ϕ_N are shown). The 6 polar angles at the Gaussian nodes of each azimuthal angle are $\theta_i = (\ 21.2 \quad 48.6 \quad 76.2 \quad 103.8 \quad 131.4 \quad 158.8\ )^\circ$, however, the 3rd (whose position is approximately shown by $v(\theta_3, \phi_0)$ in Figure 5.3a) and 4th angles exceeds the angular region the normal test modes shown in Figure 5.2 are able

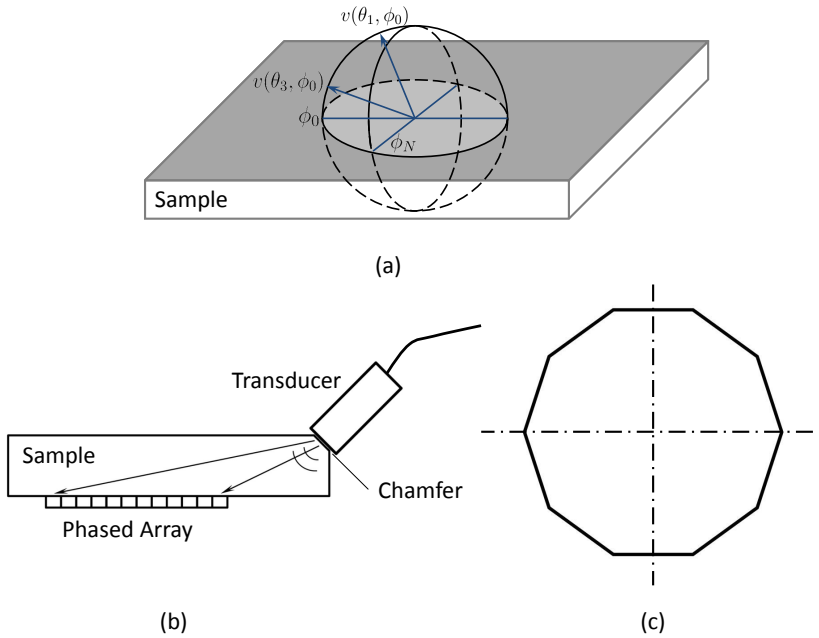

Figure 5.3: Schematics of: a. the way to use phased arrays for the wave speed measurements at Gaussian-Legendre grids; b. the experimental design using chamfered sample and the combination of a single element transducer and a phased array for the wave speed measurements at large polar angle θ_i; c. top view of the sample, which needs to be machined into the shape of a decagon for such experiments to measure the wave speed at 12 azimuthal angles ϕ_j.

to cover, given that the wave energy generated by a single element is normally confined within a cone-like region within approximately $\theta = \pm 45°$ and hardly any signal can be detected out of this region. In order to overcome this issue, the test scheme shown in Figure 5.3b is devised, where a single element transducer is applied on the edge of a chamfered sample with an approximately 45° angle from the surface plane, enabling the wave energy to reach the angles that are out of the reach of the normal test modes. Because each of such test only give the results for a single azimuthal angle ϕ_i only, it needs to be repeated at in total 12 rotated potions to obtain the data for all the required angles, therefore the sample needs to be cut into a shape with 12 edges, that is, a decagon, as shown in Figure 5.3c.

- **Things beyond the experimental validations**

The experiments will be performed soon as verifications of the spherical convolution approaches presented by the thesis; and if they turn out to be successful, a device is hoped to be developed based on the theories and the phased array technique.

Compared to other methods such as EBSD and X-ray, the technique to be developed have the advantages of being fast (almost in real time), cheap and convenient to conduct, and naturally offering non-destructive, bulk texture detections for HCP and cubic materials. In addition, it not only works at room temperatures but also at higher or lower ones, as long as the materials are still in crystalline state and the ultrasonic instruments are still able to obtain wave speeds (the kernel function in the convolution relationship needs to be changed according to the temperature to obtain relatively good results, since crystal elastic moduli change with temperature). There are also possibilities for the convolution technique to be coupled with other ultrasonic wave applications, for example grain size detection, microstructural features (eg. macrozones in titanium alloys, dislocation density and grain lattice effects) capturing, such that a complete and versatile package may be developed.

On the other hand, however, the drawback of the technique is also obvious: it is only able to detect lower degree ODF coefficients up to 4th degree. This truncation of coefficients, whose effects on the obtained texture information and the texture's usability still need follow-up studies to find out, poses limitation on the technique's application future. Therefore with these upsides and downsides combined, I think the application prospect of the technique lies in the scenarios where rough bulk texture is more desirable than accuracy of the texture itself, for example to be used as an additional means of quality control of metal sheet manufacturing process at different temperature environments, etc. It is expected to be a complementary method to EBSD and X-ray to supply information which is not accessible to the latter ones,

rather than a replacement.

Appendices

A

Brief Introduction to Spherical Harmonics

Similar with the Fourier series which provides a powerful tool for evaluation of functions in one- or two dimensions, spherical harmonics provides the platform for the analysis on the surface of a sphere. This appendix provides a short introduction to spherical harmonics excerpted from the manual by Schonefeld [93], and the reader is referred to the original text or related literature for better and more complete understandings.

- **Orthonormal basis functions**

A class of functions $\{p_n(x)\}$ is a series of *orthonormal basis functions* if its components obey the orthogonality relation over their domain $[a, b]$:

$$\int_a^b w(x)p_n(x)p_m^*(x)dx = \delta_{nm} \tag{A.1}$$

for complex-valued functions, where $w(x)$ is an arbitrary weighting function independent of m and n, the symbol $*$ denotes complex conjugate, and δ_{nm} is the Kronecker's delta between m and n. The most important property of orthonormal basis functions is that they allow the expressions of any piecewise continuous function over $[a, b]$ as a linear combination of an infinite series of linearly independent basis functions.

- **Projection and reconstruction**

For an arbitrary given function $f(x)$, everything needed to approximate it is to compute the coefficients k_n describing how much each basis function p_n is like f, and this

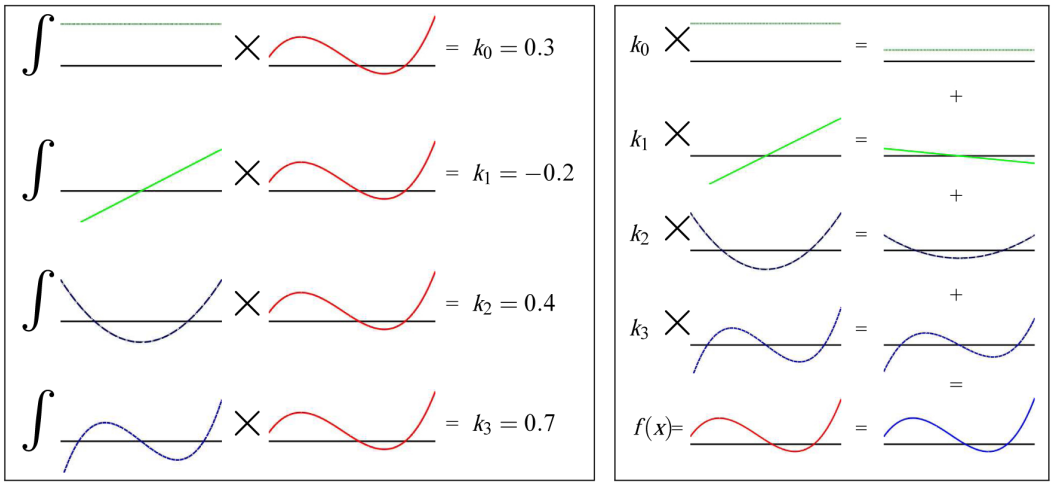

(a) **Projection** of the red polynomial into the first few Legendre coefficients k_n.

(b) **Reconstruction** of the original function by summing the scaled basis functions.

Figure A.1: An example of an expansion and reconstruction of $f(x) = 1.75x^3 + 0.6x^2 + 0.21x - 0.06$ using the first four Legendre polynomials.

is done by projecting f on to conjugate of the basis:

$$k_n = \int_a^b f(x)p_n(x)dx \tag{A.2}$$

And this process is called projection or expansion, of which one example is shown in Figure A.1a. Its inverse process is defined as linear combination of all basis functions scaled by their associated coefficients in the purpose of approximate the original function:

$$f = \sum_{n=0}^{\infty} k_n p_n(x) \tag{A.3}$$

This is called reconstruction and it is demonstrated in Figure A.1b.

- **Spherical harmonics as basis functions**

Perhaps the most prominent example of making use of orthonormal basis function is the Fourier series. Spherical harmonics are the orthonormal functions defined on the surface of a sphere equivalent to the Fourier series in one- or two-dimensions, and with respect to them any function defined on the surface of the sphere can be

expanded into linear combinations of the harmonics. They are defined as

$$Y_{lm}(\theta, \phi) = P_{lm}(\cos\theta)e^{im\phi} \tag{A.4}$$

where $P_{lm}(\cos\theta)$ is the *normalized* associate Legendre polynomial which accounts for the effects of the polar angle θ; while $e^{im\phi}$ means that the dependence of azimuthal angle ϕ in spherical harmonics is described in terms of the Fourier bases. The value of the basis functions with different degree l and order m changing on the surface of the sphere is plotted in Figure A.2. Notice that the basis functions only changes with the polar angle θ when $m = 0$, and these functions are called *zonal harmonics*. These are the only functions needed to expand the single crystal velocity function k in Chapter 3.

Now with the spherical harmonics defined as the basis functions, the similar idea of projection applies, which is about projecting a function $f(\theta, \phi)$ onto the conjugates of the bases:

$$F_{lm} = \int_{\Omega} f(\theta, \phi) Y^*_{lm}(\theta, \phi) d\Omega, \tag{A.5}$$

and the reconstruction can be done similarly via:

$$f(\theta, \phi) = \sum_{l=0}^{+\infty} \sum_{m=-l}^{l} F_{lm} Y_{lm}(\theta, \phi). \tag{A.6}$$

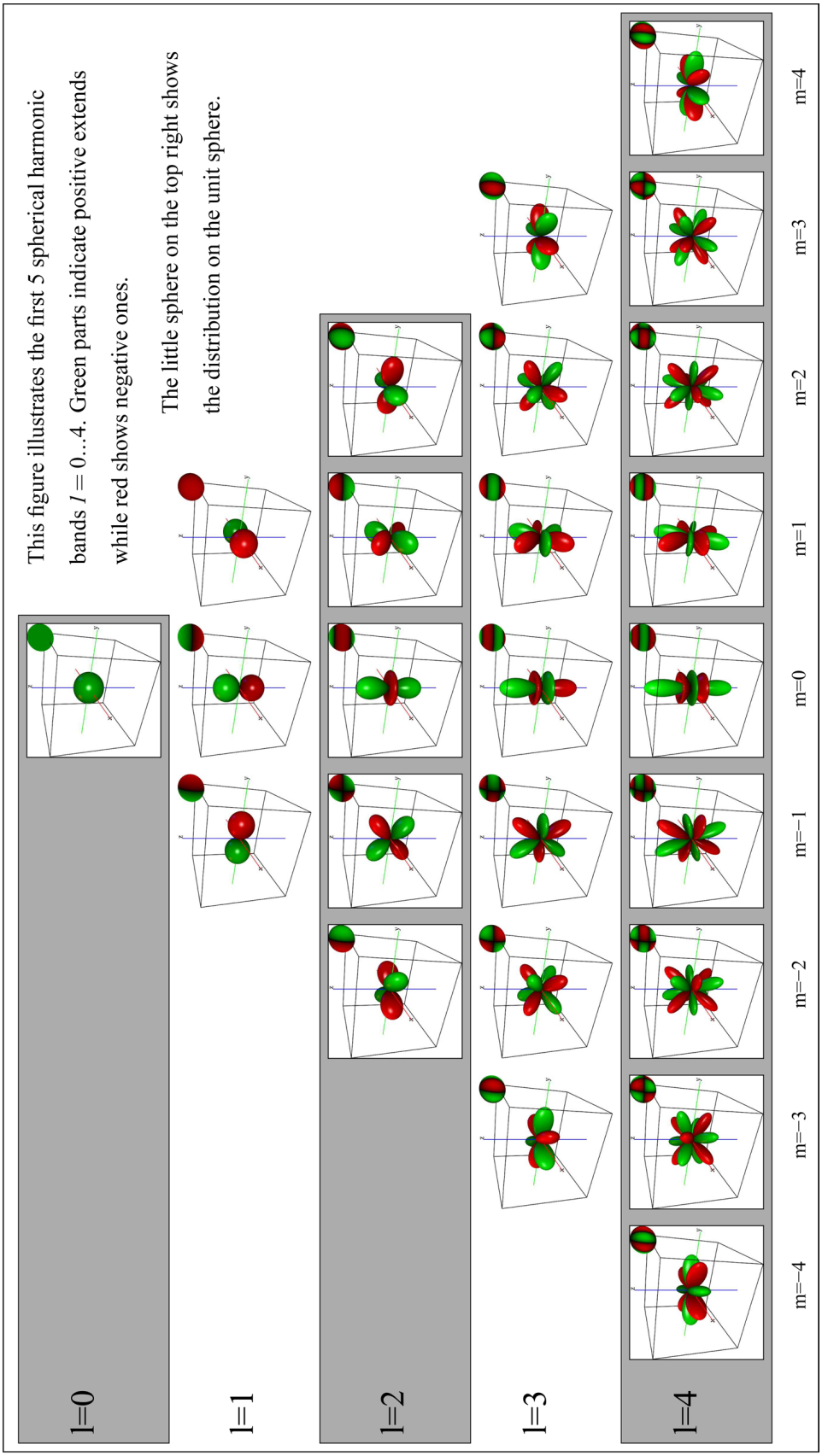

Figure A.2: Spherical harmonic basis functions.

B

Angular Differences between Phase Velocity and Particle Displacement Directions for HCP and Cubic Single Crystals

For the known elastic matrix **C** of a material and an arbitrarily given wavefront normal **n**, deductions of the Christoffel equation finally conclude as

$$[c_{ijkl}n_j n_k - \rho v^2 \delta_{il}][A_l] = 0, \tag{B.1}$$

where the subscripts stand for the tensor component indices, ρ is the material's density, δ is the Kronecker product and the vector **A** is the particle displacement vector (or referred to as the polarization vector). It now transpires that equation B.1 is a

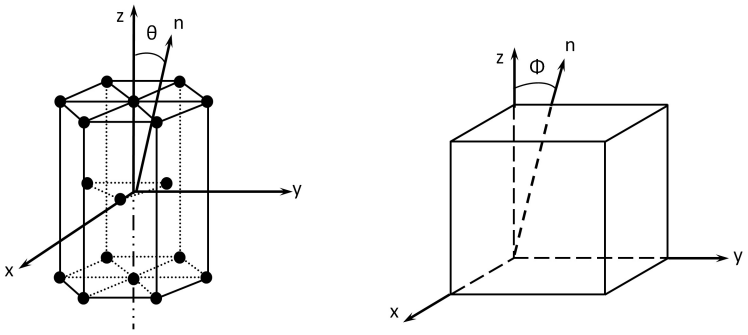

Figure B.1: The orientations of an HCP and a cubic crystal to be studied. The vector **n** varies on the y-z plane, with the angles $\theta \in [0, \pi/2]$ and $\Phi \in [0, \pi/4]$.

classical eigenvalue-eigenvector problem; its three eigenvalues are directly linked to the phase velocities, of which the largest one is the longitudinal or *quasi*-longitudinal wave velocity, depending on whether its corresponding eigenvector is exactly parallel with **n** or not. As both **n** and **A** are unit vectors, the angle between them is hence

equal to $\arccos(\mathbf{n} \cdot \mathbf{A})$.

Table B.1: Single crystal elastic moduli α phase Ti-6Al-4V and Fe, for the former $C_{66} = (C_{11} - C_{12})/2$ (Units:GPa).

	C_{11}	C_{12}	C_{13}	C_{33}	C_{44}
Ti-6Al-4V(α phase)	170.0	92.0	70.0	192.0	52.0
Fe	228.09	133.48	-	-	110.87

Our intention here is to evaluate the angular differences between the vectors **n** and **A** for HCP and cubic crystals; and as an example, only **n** varying on the x-z planes for the crystals with orientations shown in Figure B.1 are studied. It can be proved [107] that

Table B.2: Angular differences between **n** and **A** for the HCP and cubic crystals at certain directions

HCP(Ti-6Al-4V)		Cubic(Fe)	
θ	angle between **n** and **A** (deg)	Φ	angle between **n** and **A** (deg)
0	0.00	0	0.00
$\pi/16$	1.39	$\pi/32$	5.64
$\pi/8$	2.42	$\pi/16$	9.15
$3\pi/16$	2.84	$3\pi/32$	10.29
$\pi/4$	2.58	$\pi/8$	9.69
$5\pi/16$	1.85	$5\pi/32$	7.99
$3\pi/8$	1.04	$3\pi/16$	5.63
$7\pi/16$	0.42	$7\pi/32$	2.90
$\pi/2$	0.00	$\pi/4$	0.00

for the HCP crystal in Figure B.1a, $\theta \in [0, \pi/2]$ is the smallest symmetric component region to evaluate the angular difference; while for the cubic crystal in Figure B.1b, $\Phi \in [0, \pi/4]$ is the smallest region. α-phased Ti-6Al-4V and Fe, whose elastic stiffness

components are shown in Table B.1, are studied as the exemplary materials, and the angular differences for selections of θ and Φ are listed in Table B.2. It is thus clear that the largest difference between $\mathbf{n}$ and $\mathbf{A}$ for an HCP crystal is less than 3 degrees but escalate to more than 10 degrees for the cubic, so the former difference is often neglected while the latter needs to be taken account of for accurate calculations.

Bibliography

[1] Michael M Woolfson. *An Introduction to X-ray Crystallography*. Cambridge University Press, 1997.

[2] H.P. Klug and L.E. Alexander. *X-Ray Diffraction Procedures: For Polycrystalline and Amorphous Materials*. Wiley Interscience Publication. Wiley, 1974.

[3] C. Giacovazzo, G. Artioli, H.L. Monaco, D. Viterbo, and M. Milanesio. *Fundamentals of Crystallography*. IUCr texts on crystallography. OUP Oxford, 2011.

[4] Cubic crystal system, June 2014.

[5] Greenwood. *Chemistry of the Elements*. Elsevier Science & Technology Books, 1996.

[6] P. Radaelli. *Symmetry in Crystallography: Understanding the International Tables*. IUCr texts on crystallography. OUP Oxford, 2011.

[7] John Bamberg, Grant Cairns, Devin Kilminster, et al. The crystallographic restriction, permutations, and goldbach's conjecture. *The American mathematical monthly*, 110(3):202–209, 2003.

[8] Marjorie Senechal. What is a quasicrystal. *Notice of the AMS*, 53:886–887, 2006.

[9] U. Fred Kocks, Carlos Norberto Tome, and H. R. Wenk. *Texture and anisotropy: preferred orientations in polycrystals and their effect on materials properties*. Cambridge university press, 2000.

[10] HJ Bunge. Three-dimensional texture analysis. *International Materials Reviews*, 32(1):265–291, 1987.

[11] V. Randle and O. Engler. *Introduction to Texture Analysis: Macrotexture, Microtexture and Orientation Mapping*. Taylor & Francis, 2000.

[12] H.J. Bunge. *Texture analysis in materials science: mathematical methods*. Butterworths, 1982.

[13] S. Matthies, G.W. Vinel, and K. Helming. *Standard distributions in texture analysis: maps for the case of cubic-orthorhomic symmetry*. Standard Distributions in Texture Analysis: Maps for the Case of Cubic-orthorhomic Symmetry. Akademie-Verlag, 1987.

[14] HR Wenk and Paul Van Houtte. Texture and anisotropy. *Reports on Progress in Physics*, 67(8):1367, 2004.

[15] F. Ullmann, W. Gerhartz, Y.S. Yamamoto, F.T. Campbell, R. Pfefferkorn, and J.F. Rounsaville. *Ullmann's Encyclopedia of industrial chemistry*. Number v. 2 in Ullmann's Encyclopedia of Industrial Chemistry. VCH, 1995.

[16] Y. N. Wang and J. C. Huang. Texture analysis in hexagonal materials. *Materials Chemistry and Physics*, 81(1):11–26, 2003.

[17] HR Wenk, T Takeshita, R Jeanloz, and GC Johnson. Development of texture and elastic anisotropy during deformation of hcp metals. *Geophysical Research Letters*, 15(1):76–79, 1988.

[18] B. Lan, M. Lowe, and F. P. E. Dunne. Experimental and computational studies of ultrasound wave propagation in hexagonal close-packed polycrystals for texture detection. *Acta Materialia*, 63:107–122, 2014.

[19] Gerd Lutjering and James Case Williams. *Titanium*, volume 2. Springer, 2003.

[20] Robert Gehrmann, Matthias M Frommert, and Günter Gottstein. Texture effects on plastic deformation of magnesium. *Materials Science and Engineering: A*, 395(1):338–349, 2005.

[21] M.J. Philippe, M. Serghat, P. Van Houtte, and C. Esling. Modelling of texture evolution for materials of hexagonal symmetry-ii. application to zirconium and titanium α or near α alloys. *Acta Metallurgica et Materialia*, 43(4):1619 – 1630, 1995.

[22] HP Lee, C Esling, and HJ Bunge. Development of the rolling texture in titanium. *Texture, Stress, and Microstructure*, 7(4):317–337, 1988.

[23] S Banumathy, RK Mandal, and AK Singh. Texture and anisotropy of a hot rolled ti–16nb alloy. *Journal of Alloys and Compounds*, 500(2):L26–L30, 2010.

[24] C.N. Tome, R.A. Lebensohn, and U.F. Kocks. A model for texture development dominated by deformation twinning: Application to zirconium alloys. *Acta Metallurgica et Materialia*, 39(11):2667 – 2680, 1991.

[25] R.A. Lebensohn and C.N. Tome. A self-consistent anisotropic approach for the simulation of plastic deformation and texture development of polycrystals: Application to zirconium alloys. *Acta Metallurgica et Materialia*, 41(9):2611 – 2624, 1993.

[26] S.R. Agnew, M.H. Yoo, and C.N. Tome. Application of texture simulation to understanding mechanical behavior of mg and solid solution alloys containing li or y. *Acta Materialia*, 49(20):4277 – 4289, 2001.

[27] Sean R. Agnew and ´Ozg´ur Duygulu. Plastic anisotropy and the role of non-basal slip in magnesium alloy AZ31B. *International Journal of Plasticity*, 21(6):1161 – 1193, 2005. Plasticity of Multiphase Materials.

[28] K Le Biavant, S Pommier, and C Prioul. Local texture and fatigue crack initiation in a ti-6al-4v titanium alloy. *Fatigue & Fracture of Engineering Materials & Structures*, 25(6):527–545, 2002.

[29] L. Germain, N. Gey, M. Humbert, P. Bocher, and M. Jahazi. Analysis of sharp microtexture heterogeneities in a bimodal IMI 834 billet. *Acta Materialia*, 53(13):3535 – 3543, 2005.

[30] L. Germain, N. Gey, M. Humbert, P. Vo, M. Jahazi, and P. Bocher. Texture heterogeneities induced by subtransus processing of near alpha titanium alloys. *Acta Materialia*, 56(16):4298 – 4308, 2008.

[31] Ioannis Bantounas, David Dye, and Trevor C Lindley. The role of microtexture on the faceted fracture morphology in Ti-6Al-4V subjected to high-cycle fatigue. *Acta Materialia*, 58(11):3908 – 3918, 2010.

[32] Jian-Min Zhang, Yan Zhang, Ke-Wei Xu, and Vincent Ji. Young's modulus surface and poisson's ratio curve for cubic metals. *Journal of Physics and Chemistry of Solids*, 68(4):503 – 510, 2007.

[33] Fionn Dunne and Nik Petrinic. *Introduction to computational plasticity*. Oxford University Press New York, 2005.

[34] CA Bronkhorst, SR Kalidindi, and L Anand. Polycrystalline plasticity and the evolution of crystallographic texture in fcc metals. *Philosophical Transactions of the Royal Society of London. Series A: Physical and Engineering Sciences*, 341(1662):443–477, 1992.

[35] I.L Dillamore and W.T Roberts. Rolling textures in f.c.c. and b.c.c. metals. *Acta Metallurgica*, 12(3):281 – 293, 1964.

[36] H.J. Bunge and C. Esling. Texture development by plastic deformation. *Scripta Metallurgica*, 18(3):191 – 195, 1984.

[37] J. Hirsch and K. Lucke. Overview no. 76: Mechanism of deformation and development of rolling textures in polycrystalline f.c.c. metals-i. description of rolling texture development in homogeneous cuzn alloys. *Acta Metallurgica*, 36(11):2863 – 2882, 1988.

[38] Lawrence C Biedenharn and James D Louck. *Angular momentum in quantum physics*. Cambridge University Press, 1984.

[39] R. J. Roe. Description of crystallite orientation in polycrystalline materials .3. general solution to pole figure inversion. *Journal of Applied Physics*, 36(6):2024–2031, 1965.

[40] M. A. Morrison and G. A. Parker. A guide to rotations in quantum mechanics. *Australian Journal of Physics*, 40:465, 1987.

[41] J. Roe, R. Inversion of pole figures for materials having cubic crystal symmetry. *Journal of Applied Physics*, 37:2069–2072, 1966.

[42] J.J. Kearns. Thermal expansion and preferred orientation in zircaloy (lwdr development program). Report, Westinghouse, 1965.

[43] A. J. Anderson, R. B. Thompson, and C. S. Cook. Ultrasonic measurement of the kearns texture factors in zircaloy, zirconium, and titanium. *Metallurgical and Materials Transactions a-Physical Metallurgy and Materials Science*, 30(8):1981–1988, 1999.

[44] Bertram Eugene Warren. *X-ray Diffraction*. Courier Dover Publications, 1969.

[45] F. Heidelbach, C. Riekel, and H.-R. Wenk. Quantitative texture analysis of small domains with synchrotron radiation x-rays. *Journal of Applied Crystallography*, 32(5):841–849, Oct 1999.

[46] L. Wcislak, H. Klein, H. J. Bunge, U. Garbe, T. Tschentscher, and J. R. Schneider. Texture analysis with high-energy synchrotron radiation. *Journal of Applied Crystallography*, 35(1):82–95, Feb 2002.

[47] Paula MB Piccoli, Thomas F Koetzle, and Arthur J Schultz. Single crystal neutron diffraction for the inorganic chemist–a practical guide. *Comments on Inorganic Chemistry*, 28(1-2):3–38, 2007.

[48] Roger Pynn. Neutron Scattering: A Primer, 1990.

[49] Angus J. Wilkinson and T. Ben Britton. Strains, planes, and ebsd in materials science. *Materials Today*, 15(9):366–376, 2012.

[50] T Ben Britton. Introduction to ebsd. Online, 2013.

[51] Adam J Schwartz, Mukul Kumar, Brent L Adams, and David P Field. *Electron backscatter diffraction in materials science*. Springer, 2009.

[52] M. Clark, S. D. Sharples, and M. G. Somekh. Fast, all-optical rayleigh wave microscope: Imaging on isotropic and anisotropic materials. *Ieee Transactions on Ultrasonics Ferroelectrics and Frequency Control*, 47(1):65–74, 2000.

[53] Steve D. Sharples, Matthew Clark, and Mike G. Somekh. Spatially resolved acoustic spectroscopy for fast noncontact imaging of material microstructure. *Optics Express*, 14(22):10435–10440, 2006.

[54] Philip John Withers. Depth capabilities of neutron and synchrotron diffraction strain measurement instruments. i. the maximum feasible path length. *Journal of Applied Crystallography*, 37(4):596–606, Aug 2004.

[55] Philip Withers. Depth capabilities of neutron and synchrotron diffraction strain measurement instruments. ii. practical implications. *Journal of Applied Crystallography*, 37(4):607–612, 2004.

[56] Jan Achenbach. *Wave propagation in elastic solids*. Elsevier, 1984.

[57] F. E. Stanke and G. S. Kino. A unified theory for elastic wave-propagation in polycrystalline materials. *Journal of the Acoustical Society of America*, 75(3):665–681, 1984.

[58] MarkP. Blodgett and Daniel Eylon. The influence of texture and phase distortion on ultrasonic attenuation in ti-6al-4v. *Journal of Nondestructive Evaluation*, 20(1):1–16, 2001.

[59] M. Juva, A.and Haarvisto. On the effects of microstructure on the attenuation of ultrasonic waves in austenitic stainless steel. *British Journal of Non-Destructive Testing*, 1977.

[60] R. Klinman, G. R. Webster, F. J. Marsh, and E. T. Stephenson. Ultrasonic prediction of grain size, strength, and toughness in plain carbon steel. In *Ultrasonic Materials Characterization*, volume 596, page 83. US Department of Commerce, National Bureau of Standards, 1980.

[61] Jafar Saniie and Nihat M. Bilgutay. Quantitative grain size evaluation using ultrasonic backscattered echoes. *The Journal of the Acoustical Society of America*, 80(6):1816–1824, 1986.

[62] James H. Rose. Ultrasonic backscatter from microstructure. In *Review of Progress in Quantitative Nondestructive Evaluation. Vol. 11B*, volume 11, pages 1677–1684, 1992.

[63] P. Palanichamy, A. Joseph, T. Jayakumar, and Baldev Raj. Ultrasonic velocity measurements for estimation of grain size in austenitic stainless steel. *NDT & E International*, 28(3):179 – 185, 1995.

[64] Y. K. Han and R. B. Thompson. Ultrasonic backscattering in duplex microstructures: Theory and application to titanium alloys. *Metallurgical and Materials Transactions a-Physical Metallurgy and Materials Science*, 28(1):91–104, 1997.

[65] A. Bhattacharjee, A. L. Pilchak, O. I. Lobkis, J. W. Foltz, S. I. Rokhlin, and J. C. Williams. Correlating ultrasonic attenuation and microtexture in a near-alpha titanium alloy. *Metallurgical and Materials Transactions a-Physical Metallurgy and Materials Science*, 42A(8):2358–2372, 2011.

[66] L. Yang, J. Li, O. I. Lobkis, and S. I. Rokhlin. Ultrasonic propagation and scattering in duplex microstructures with application to titanium alloys. *Journal of Nondestructive Evaluation*, 31(3):270–283, 2012.

[67] L. Yang, J. Li, and S. I. Rokhlin. Ultrasonic scattering in polycrystals with orientation clusters of orthorhombic crystallites. *Wave Motion*, 50(8):1283–1302, December 2013.

[68] R. Hill. The elastic behaviour of a crystalline aggregate. *Proceedings of the Physical Society of London Section A*, 65(389):349–355, 1952.

[69] P. R. Morris. Averaging fourth-rank tensors with weight functions. *Journal of Applied Physics*, 40(2):447–448, 1969.

[70] C. M. Sayers. Ultrasonic velocities in anisotropic polycrystalline aggregates. *Journal of Physics D-Applied Physics*, 15(11):2157–2167, 1982.

[71] G. Backus. A geometrical picture of anisotropic elastic tensors. *Reviews of Geophysics and Space Physics*, 8(3):633–671, 1970.

[72] Martin L. Smith and F. A. Dahlen. The azimuthal dependence of love and rayleigh wave propagation in a slightly anisotropic medium. *J. Geophys. Res.*, 78(17):3321–3333, June 1973.

[73] Y. Li and R. B. Thompson. Relations between elastic-constants cij and texture parameters for hexagonal materials. *Journal of Applied Physics*, 67(5):2663–2665, 1990.

[74] R.B. Thompson, S.S. Lee, and J.F. Smith. Relative anisotropies of plane waves and guided modes in thin orthorhombic plates: Implication for texture characterization. *Ultrasonics*, 25(3):133 – 137, 1987.

[75] M. Hirao, K. Aoki, and H. Fukuoka. Texture of polycrystalline metals characterized by ultrasonic velocity-measurements. *Journal of the Acoustical Society of America*, 81(5):1434–1440, 1987.

[76] P. J. Kielczynski, A. Moreau, and J. F. Bussiere. Determination of texture coefficients in hexagonal polycrystalline aggregates with orthorhombic symmetry using ultrasounds. *Journal of the Acoustical Society of America*, 95(2):813–827, 1994.

[77] C. M. Sayers. Angular dependent ultrasonic wave velocities in aggregates of hexagonal crystals. *Ultrasonics*, 24(5):289–291, 1986.

[78] S. Dixon, C. Edwards, and S. B. Palmer. Texture measurements of metal sheets using wideband electromagnetic acoustic transducers. *Journal of Physics D-Applied Physics*, 35(8):816–824, 2002. PII S0022-3727(02)30108-6.

[79] E.B. Christoffel. *Ann.di Mat*, 8:193, 1877.

[80] Joseph L. Rose. *Ultrasonic waves in solid media*. Cambridge university press, 2004.

[81] M.J.P. Musgrave. *Crystal Acoustics: Introduction to the Study of Elastic Waves and Vibrations in Crystals*. Holden-Day series in mathematical physics. Holden-Day, 1970.

[82] FPE Dunne and D Rugg. On the mechanisms of fatigue facet nucleation in titanium alloys. *Fatigue & Fracture of Engineering Materials & Structures*, 31(11):949–958, 2008.

[83] D Raabe, Z Zhao, S.-J Park, and F Roters. Theory of orientation gradients in plastically strained crystals. *Acta Materialia*, 50(2):421 – 440, 2002.

[84] Anish Kumar, T. Jayakumar, Baldev Raj, and K.K. Ray. Characterization of solutionizing behavior in vt14 titanium alloy using ultrasonic velocity and attenuation measurements. *Materials Science and Engineering: A*, 360:58 – 64, 2003.

[85] R.E. Newnham. *Properties of Materials : Anisotropy, Symmetry, Structure: Anisotropy, Symmetry, Structure*. OUP Oxford, 2004.

[86] F Bachmann, Ralf Hielscher, and Helmut Schaeben. Texture analysis with mtex–free and open source software toolbox. *Solid State Phenomena*, 160:63–68, 2010.

[87] A. Moreau, L. Toubal, P. Bocher, M. Humbert, E. Uta, and N. Gey. Evaluation of macrozone dimensions by ultrasound and ebsd techniques. *Materials Characterization*, 75:115–128, 2013.

[88] David Rugg. Private communication, 2012.

[89] Robert Kiwanuka. *Mocro-deformation and Texture in Engineering Materials*. PhD thesis, University of Oxford, 2013.

[90] J.L.W. Warwick, J. Coakley, S.L. Raghunathan, R.J. Talling, and D. Dye. Effect of texture on load partitioning in ti-6al-4v. *Acta Materialia*, 60(10):4117 – 4127, 2012.

[91] R. Ramamoorthi and P. Hanrahan. On the relationship between radiance and irradiance: Determining the illumination from images of a convex lambertian object. *Journal of the Optical Society of America a-Optics Image Science and Vision*, 18(10):2448–2459, 2001.

[92] R. Ramamoorthi and P. Hanrahan. *An efficient representation for irradiance environment maps*, pages 497–500. Computer Graphics. 2001. SIGGRAPH 2001 AUG 12-17, 2001 LOS ANGELES, CA ACM SIGGRAPH.

[93] Volker Schonefeld. Spherical harmonics, 2005.

[94] Morris Edgar Rose. *Elementary theory of angular momentum*. Courier Dover Publications, 1995.

[95] David Mainprice, Ralf Hielscher, and Helmut Schaeben. Calculating anisotropic physical properties from texture data using the mtex open-source package. *Geological Society, London, Special Publications*, 360(1):175–192, 2011.

[96] J. R. Driscoll and D. M. Healy. Computing fourier transforms and convolutions on the 2-sphere. *Advances in Applied Mathematics*, 15(2):202–250, 1994.

[97] Martin J. Mohlenkamp. A user's guide to spherical harmonics, 2011.

[98] JAR Blais and Dean Allen Provins. Spherical harmonic analysis and synthesis for global multiresolution applications. *Journal of Geodesy*, 76(1):29–35, 2002.

[99] A.D. Rollett. Orientation distribution:definition, discrete forms, examples. University Lecture, 2014.

[100] Bruce W Drinkwater and Paul D Wilcox. Ultrasonic arrays for non-destructive evaluation: A review. *NDT & E International*, 39(7):525–541, 2006.

[101] Jun Jiang, T. Benjamin Britton, and Angus J. Wilkinson. Mapping type III intragranular residual stress distributions in deformed copper polycrystals. *Acta Materialia*, 61(15):5895 – 5904, 2013.

[102] Peter J Kostelec and Daniel N Rockmore. Soft: So (3) fourier transforms. *Department of Mathematics, Dartmouth College, Hanover, NH*, 3755, 2007.

[103] SI Rokhlin and W Wang. Double through-transmission bulk wave method for ultrasonic phase velocity measurement and determination of elastic constants of composite materials. *The Journal of the Acoustical Society of America*, 91(6):3303–3312, 1992.

[104] Chuan Li, Damien Pain, Paul D Wilcox, and Bruce W Drinkwater. Imaging composite material using ultrasonic arrays. *NDT & E International*, 53:8–17, 2013.

[105] LH Pearson and WJ Murri. Measurement of ultrasonic wavespeeds in off-axis directions of composite materials. In *Review of Progress in Quantitative Nondestructive Evaluation*, pages 1093–1101. Springer, 1987.

[106] SI Rokhlin and W Wang. Ultrasonic evaluation of in-plane and out-of-plane elastic properties of composite materials. In *Review of Progress in Quantitative Nondestructive Evaluation*, pages 1489–1496. Springer, 1989.

[107] B.A. Auld. *Acoustic fields and waves in solids*. Number v. 2 in Acoustic Fields and Waves in Solids. R.E. Krieger, 1990.